eman ta zabal zazu

Universidad   Euskal Herriko
del País Vasco Unibertsitatea

Modelling of Polymer–Carbon Nanotube Heterojunctions for Photovoltaic Applications

by

Livia Noëmi Glanzmann

Supervisors:

Professor Angel Rubio Secades

Associate Professor Duncan John Mowbray

A thesis

presented to the University of the Basque Country UPV/EHU

in fulfilment of the

thesis requirement for the degree of

Doctor of Philosophy

in

Physics of Nanostructures and Advanced Materials

Donostia-San Sebastián, Guipuzkoa, España, January 26, 2017

Abstract

Semiconducting single-walled carbon nanotubes (s-SWNTs) have outstanding physical properties such as high thermal stability, scattering-free (ballistic) charge carrier transport with charge carrier mobilities of up to >100,000 cm^2/Vs, and high current densities. In addition, s-SWNTs have large and tunable optical absorption over a wide spectral range due to the specific band gaps of different tube chiralities. All these remarkable properties make semiconducting carbon nanotubes promising materials for a new generation of highly efficient organic photovoltaics (OPVs). Unfortunately, the implementation of s-SWNTs has so far not lead to the expected increase in power conversion efficiencies of OPVs. It is exactly on this topic which we focus in the theoretical studies presented in this work.

To begin, we find efficient ways to model polymer-SWNT heterojunctions. Using linear dielectric response (LDR) time-dependent density functional theory (TDDFT) claculations within the random phase approximation (RPA), we find that the electronic properties of the copolymer of 9,9-dioctylfluorenyl-2,7-diyl and bipyridine (PFO-BPy) are sufficiently described by the subunit Py-PFO-Py. This result can be used to perform studies on polymer-SWNT interactions and supramolecular structure analysis of polymer-SWNT heterojunctions. Knowing the transition dipole moment of polymers allows us to extract the orientation of the polymer with respect to the SWNT axis from polarized angle-dependent absorption spectra. We show that linear response (LR) TDDFT is a good tool for identifying the direction of the polarized light absorbed by a certain transition in the PFO-BPy spectrum.

Further, we explore the mechanisms of exciton generation, diffusion, decay, and splitting into free charge carriers in polymer-SWNT blends. This is done by evaluating the transient spectrum, which provides direct information about photoexcitation processes. The existence of a photoinduced absorption (PA) peak in the transient spectrum of SWNTs and polymer-SWNT heterojunctions, and how it depends on such systems, is still an active subject of investigation. We model the transient spectrum of a polymer:fullerene:s-SWNT blend from its ground and excited state difference spectrum using LDR-TDDFT-RPA. Based on our results, we are able to explain the origin of the PA peak in transient spectra of s-SWNT systems and the electronic dynamics linked to it.

Finally, we evaluate the internal quantum efficiency (IQE) of different donor–acceptor blends by carrying out density functional theory (DFT) calculations of the excited state formation energy, charge transfer, and zero-bias conductance of prototypical donor–acceptor heterojunctions in the singlet ground state and triplet excited state. We calculate the Landauer-Bütticker conductance of electron and hole charge carriers from donor to acceptor across the heterojunction based on the DFT tight-binding Hamiltonians using a multiterminal implementation of the non-equilibrium Green's function (NEGF) method. We find a dependence of the conductivity on the level alignment, which demonstrates the importance of considering the hybridization of donor–acceptor levels in the excited state. By improving the level alignment of the polymer and s-SWNT through the use of larger band gap s-SWNTs, one may obtain a dramatic improvement in OPV efficiency.

In summary, our results provide a deeper insight into the photoexcitation and electronic processes in polymer–s-SWNT heterojunctions and thus support the development of more efficient polymer–s-SWNT OPVs.

Acknowledgements

I would like to express my special appreciation to my supervisors Angel Rubio and Duncan Mowbray, for the incredible opportunity they gave me, their guidance, support, and trust in me. I want to thank Angel for giving me the freedom to choose my projects and letting me develop my own ideas. Duncan I want to thank for his endless patience teaching me as much as possible. None of these projects, including writing the thesis, would have been that successful without his help, criticism, ideas, and know-how. Much more, I want to thank Duncan for his friendship and the good times outside of the office.

I thank all the people of the POCAONTAS network for the fantastic and stimulating times during the meetings. Many thanks go to the people who hosted me during the last years. I thank Tobias Hertel and Florian Späth for the fruitful discussions, the great time in Würzburg and at all the conferences, I want to thank Jorge Morgado and Rajesh Veeravarapu for the good times at the IST in Lisbon, and last but not least I thank Guglielmo Lanzani, Diana Gisell Figueroa del Valle, Isis Maqueira, and Francesco Scotognella for having me 3 months at the IIT in Milano and for the successful collaboration we had.

Special thank goes to Cecilia Benguria, Izaskun Ibarbia, and Kate Chabarek for the help with all the paper work during these years.

I want to thank all my colleagues and friends of the Nano-Bio Spectroscopy Group, for the great working atmosphere, the support when things were not running, and the wonderful times during lunch, coffee breaks, and outside of working hours. Without you this last years would not have been the same. Especially, I want to thank Ask for his friendship and for making magic with GPAW and python.

Thanks go to Bruce for all the fun times we had during his visits and the stimulating discussions.

Vielen Dank an meine Freunde, die mich all die Jahre unterstützt und besucht haben. Ihr seid die Besten!

Muchisimas gracias a mi suegra Silvia por la ayuda cuidando a Lia mientras escribia esta tesis.

Grossen Dank geht an meine Familie, an meine Schwester Andrea, meinen Vater Emil, und meine Mutter Elisabeth, ohne die das alles gar nicht möglich gewesen wäre. Ganz herzlich möchte ich meiner Mutter danken für die grenzenlose Unterstützung durch all die Jahre hindruch.

I want to thank my husband, Marcos, for his support during the stressful but wonderful time, for his love, his care, and the future he plans with me.

Contents

List of Figures

List of Tables

List of Papers

[1] Glanzmann, L. N.; Mowbray, D. J.; Rubio, A. PFO-BPy Solubilizers for SWNTs: Modelling Polymers from Oligomers. *Phys. Stat. Solidi B* **2014**, *251*, 2407–2412.

[2] Glanzmann, L. N.; Mowbray, D. J.; Figueroa del Valle, D. G.; Scotognella, F.; Lanzani, G.; Rubio, A. Photoinduced Absorption within Single-Walled Carbon Nanotube Systems. *J. Phys. Chem. C* **2015**, *120*, 1926–1935.

[3] Glanzmann, L. N.; Mowbray, D. J. Theoretical Insight into the Internal Quantum Efficiencies of Polymer/C_{60} and Polymer/SWNT Photovoltaic Devices. *J. Phys. Chem. C* **2016**, *120*, 6336–6343.

Chapter 1

Introduction

Since Bell Laboratories produced the first silicon-based solar cell in 1954[1], the public interest in this safe, clean, and renewable energy source has grown substantially, with the photovoltaic market reaching a global total of 227 GW in 2015[2]. However, although the sun provides several times more energy than the world population consumes[3], only around 1% of the total world electricity demand is met by photovoltaics.[2] This stems from the high production costs of silicon-based solar panels. Although their price has decreased significantly in the last few years, the cost of silicon-based solar panels still can not compete with the inexpensive supply of fossil fuels or nuclear power.[4]

Cheap organic compounds may help to overcome this obstacle. The last decades gave rise to numerous novel organic materials from conducting polymers[5–8] to carbon-only structures such as graphene[9,10], fullerenes[11] and carbon nanotubes[12–15]. All these materials have a conjugated π-system over which the electrons are delocalized. When the electrons in this one dimensional electronic band become mobile, the compound shows conductivity. This is the case when the band is partially emptied or filled, for example, when the material is "doped" via oxidation or reduction. For the discovery and the development of conductive polymers Alan J. Heeger, Alan MacDiarmid and Hideki Shirakawa were awarded the 2000 Nobel Prize in Chemistry.[16] Undoped conjugated polymers are typically semiconductors rather than metals or insulators. Their band gaps show absorption from the ultraviolet spectral region (UV) to the near infrared spectral region (NIR), which makes them suitable for photovoltaic applications. In addition, organic compounds are light and flexible compared to their inorganic counterparts, which broadens their scope of application. But are they competitive in photovoltaic devices regarding their efficiencies?

For inorganic p-n junction solar cells, power conversion efficiency (PCE) of 25%[17,18] have been reached, as described in Appendix A. Although this may sound low, Schockley and Queisser have shown that with an optimal bandgap of 1.1 electronvolt (eV), the maximum efficiency obtainable for an inorganic p-n junction under ideal conditions is 30%.[19] In principle, the maximum efficiency for organic photovoltaics (OPVs) should be higher due to their lower refractive index.[20] Nevertheless, so far the highest PCE reached for OPVs is ~ 10%.[21]

To improve the performance of OPVs, we must take a closer look at the physical properties of organic materials and the working principle of such devices. Figure 1.1 provides a schematic description of a type II heterojunction, where the valence band (VB) and conduction band (CB) of the acceptor lie energetically lower but close to the VB and CB of the donor.[20] Upon irradiation a singlet exciton, i.e., a Coulomb-bound electron-hole pair, is created via photo-excitation of an electron from the VB to the CB of the donor material.[22] The donor is typically a semiconducting polymer such as poly(3-hexylthiophene-2,5-diyl) (P3HT) , in which the exciton extends over 1 nm and exhibits
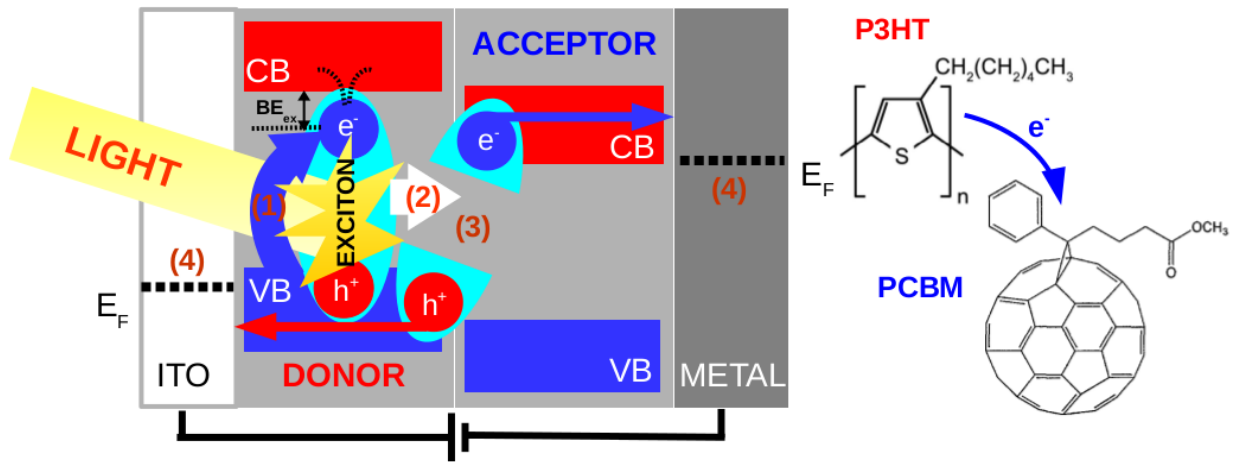
Figure 1.1: Schematic working principle of an OPV device; (1) exciton generation within the donor material (P3HT), (2) diffusion to the donor–acceptor (P3HT-PCBM) interface, (3) exciton splitting, and (4) electron (hole) transport as bound polaron pair through the acceptor's (donor's) conduction (valence) band to the metal electrode (ITO).

a binding energy BE_{ex} between 0.35 and 0.5 eV.[20] In comparison to the weakly bound delocalized Wannier-Mott exciton found in silicon-based devices, this more localized Frenkel exciton is so strongly bound that its binding energy exceeds the thermal energy.[23,24] In addition, its relatively short (< 1 ns) exciton lifetime requires fast charge separation in order to achieve charge generation.[25] For this reason, next to the donor material, OPVs need an acceptor material to facilitate exciton splitting.[26,27] At the donor–acceptor interface the process of charge separation then needs to occur within 100 fs.[28] The acceptor is preferably an organic semiconducting nanostructure that will enable charge carrier transport. Most often fullerenes, such as phenyl-C_{61}-butyric acid methyl ester (PCBM), are used as the organic acceptor material.[29] Ideally, the donor and the acceptor are not separate layers but intermixed to form a so-called bulk heterojunction (BHJ).[30] Such a donor–acceptor blend provides exciton diffusion lengths from creation in the donor material to the donor–acceptor interface of less than 10 nm.[31]

Next to their strong exciton binding, organic semiconductors have two other major drawbacks. First is their narrow absorption widths, which only covers part of the visible spectral region (VIS).[29] In comparison, inorganic devices absorb over the whole visible spectrum and beyond to more than 1000 nm. This means inorganic devices have much larger absorption cross sections, even though organic semiconductors show very high absorption coefficients. Another issue is their low charge carrier mobilities. These are expected to produce recombination losses in the Langevin regime.[32–34] Interestingly, a reduced Langevin recombination was recently found in OPVs.[35] The Onsanger description of bimolecular recombination is valid when the charge transfer (CT) state of a pair of Coulomb-bound charges is more likely to dissociate again than to recombine.[36] Veldman *et al.* suggested that next to the highest occupied molecular orbital (HOMO)–lowest unoccupied molecular orbital (LUMO) difference of the donor acceptor pair, the energy of this charge transfer state defines the open-circuit voltage, V_{OC}.[37] This is important as V_{OC} is significantly lower in inorganic devices. Burke *et al.* derived an equation, which successfully explains the observed dependence of V_{OC} on the interfacial energetic disorder, temperature, and dielectric constants.[38]

In summary, the efficiency of OPV materials is limited by (1) the optical losses arising from their narrow absorption widths, (2) any misalignment of the donor and acceptor material, (3) exciton losses due to either insufficient

diffusion of excitons to the next donor–acceptor interface or inefficient exciton dissociation, and (4) charge carrier losses due to non-radiative recombination or insufficient charge mobilities.[39]

One way to overcome these limitations is by optimizing the device fabrication. This could include the use of thin layers[40] to shorten charge carrier travelling paths, bulk-heterojunctions[30] to decrease diffusion lengths, and nanocrystallinity[41] with enhanced contact surfaces to improve charge mobilities. Also, more efficient charge collection can be achieved by additional electron collecting layer (ECL) or hole collecting layer (HCL).[42–44] Depending on whether the device architecture is standard (the metal electrode is the anode) or inverted (ITO is the anode), the transparent HCL or ECL, respectively, is next to the ITO. Thin films of doped conjugated polymers like poly(3,4-ethylenedioxythiophene)poly(styrenesulfonate) (PEDOT:PSS) or a thin oxide layer (e.g. MoO_3) are used to collect holes, while fulleropyrolidine or different oxides improve the extractions of electrons. In addition, the introduction of the inverted design helps to prevent fast electrode degradation.[45]

Another approach to increasing efficiency is through the use of novel organic materials that exhibit broader absorption widths to increase exciton yields, higher dielectric constants to reduce the exciton binding energy, and higher charge carrier mobilities to improve transport.[29] Note that an increased mobility only leads to higher efficiency when combined with an efficient charge extraction, since longer extraction times also lead to a higher probability of recombination.[34,46]

Due to their exceptional physical properties, semiconducting single-walled carbon nanotubes (s-SWNTs) have attracted an enormous amount of attention in the field of electronic applications.[47] Like polymers, carbon nanotubes are solution processable and have large and tunable optical absorption. However, in contrast to polymers, no chemical changes are needed to shift their absorption spectrum, as a wide spectral range may be covered by nanotubes with different band gaps, corresponding to different tube chiralities.[48,49] A detailed explanation of the structure classification and physical properties of single-walled carbon nanotubes (SWNTs) is given in section 2.6. In addition, some semiconducting nanotubes show strong absorption peaks in the infrared next to the visible regions, with band gaps between 1 and 1.3 eV. Other advantages of SWNTs over polymers are their high thermal stability[50,51], scattering-free (ballistic) charge carrier transport[52] with charge carrier mobilities of up to >100,000 cm^2/Vs[53–56], and high current densities[57]. All these remarkable properties make semiconducting nanotubes promising materials for photovoltaics.

Recent works show one can obtain charges directly upon photoexcitation of s-SWCNTs.[58–62] The absorption in the near infrared region results from energy gaps between 1 and 1.3 eV, which lie very close to the Shockley-Queisser optimum. The elementary photoexcitations in s-SWNTs are singlet excitons with a large binding energy of about 400 meV.[48,63–67] Since nanotubes have intermediate exciton binding energies when compared to other organic materials, their physical properties make them possible donor materials. Devices with carbon nanotubes as light harvesting material showed high internal and external quantum efficiencies, but only when referred to the infrared region.[68–74] This reflects the stronger binding energy within organic materials compared to inorganic semiconductors.

Since another limiting factor of OPVs are their low charge carrier mobilities, this might be overcome by replacing the acceptor material with s-SWNTs.[75–77] Figure 1.2 shows a polymer-SWNT blend, where the polymer absorbs light $\hbar\omega$ and transfers an electron e^- to the SWNT. The introduction of nanotubes was recently shown to enhance the photoconductance and carrier lifetime in P3HT:SWNT blends.[78] Yan *et al.* improved the performance of the device by 10% after introducing carbon nanotubes in the active layer.[79] Nevertheless, an efficient prototype type II heterojunction with carbon nanotubes as acceptors has not yet been produced.[80–83] The highest PCE obtained
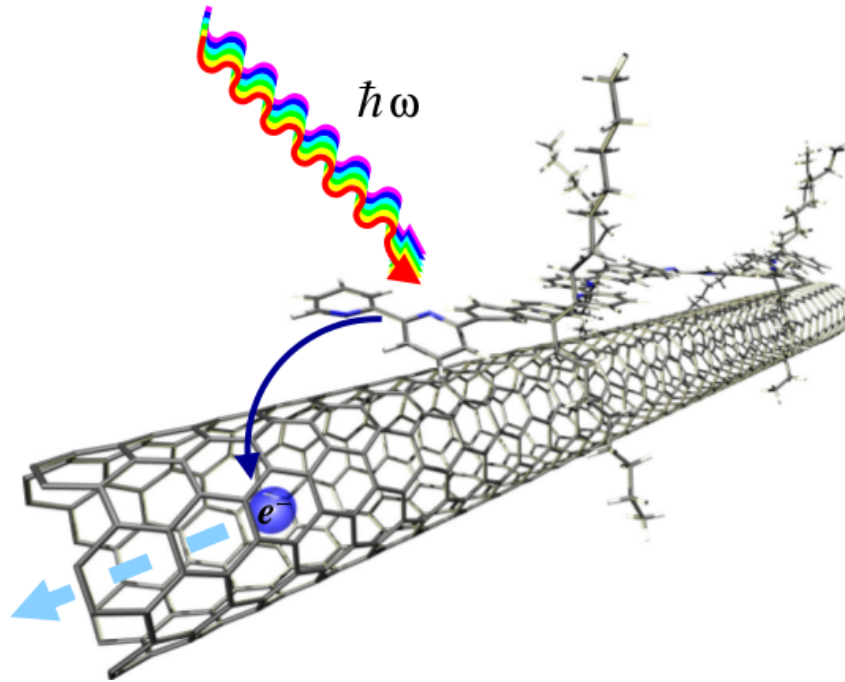
Figure 1.2: Cartoon of a polymer-SWNT hybrid system as photoactive layer in a BHJ.

from a polymer:SWNT blend is 3.02%, whereas polymer:fullerene cells have PCEs of $\sim$ 6.5%.[20,84] Another path towards improving efficiencies is by adding s-SWNTs as ECLs between the active layer and the metal electrode (ITO/P3HT:PCBM/s-SWNT/metal) to enhance electron extraction (chapter 3.3). An increase of almost 30% from 1.24% reference to 1.58% was achieved, mainly due to an increase of short-circuit current, I_{SC}.[85,86]

A summary of carbon nanotube containing photovoltaic devices is given in Refs. 87 and 88. Both reviews make clear that including carbon nanotubes in OPVs has so far not lead to a significant increase in efficiency. It is exactly here we focus in the theoretical studies presented in this work. Through modelling of polymer–SWNT blends and the undergoing photo-electric processes under illumination we reveal the interactions within the hybrid system, the mechanisms upon excitation, and the distribution and transport of charges. In this way our results support the development of more efficient polymer-SWNT OPVs. Specifically, we address different fields of investigation for SWNT containing OPVs: the modelling of the polymer–SWNT heterojunctions using monomers or oligomers, supramolecular structure evaluation of polymer–SWNT heterojunctions, transient absorption spectroscopy on polymer–s-SWNT systems, and device performance of s-SWNT OPVs, as introduced in the following sections.

1.1 Modelling Polymer–SWNT Heterojunctions by Modelling Polymers from Oligomers

One major hurdle to the use of nanotubes in electronics arises from having mixtures of nanotube chiralities that include metallic tubes. Such mixtures are the result of the synthesizing processes, which include arc discharge[89], laser ablation[90], chemical vapor deposition (CVD)[91], high-pressure carbon monoxide disproportionation (HiPco)[92], and the cobalt-molybdenum catalyst (CoMoCAT®) process[93]. While some attempts have been made to use mixtures of semiconducting chiralities as donor material to broaden the spectral range of the device[94], chirality enhanced or single chirality samples are preferred[74]. This is because several experiments have shown exciton transfer between tubes of different chiralities.[95,96] This results in electron–hole trapping on the nanotube with the smallest band gap.[74] For this reason, impurities of metallic tubes significantly reduce the efficiencies of the devices due to both a decrease in long-lived carrier population and an increase in the number of charge carrier recombination centers.[78,97] Another advantage to using chirality sorted SWNTs is the possibility of employing specific tubes with the optimal band gaps. This would allow the tuning of the donor–acceptor (polymer–SWNT) interface.[71,75,76,98]

For these reasons it is essential to find an efficient path to untie, sort and isolate tubes based on their diameters and chiralities.[99] A suitable medium to disperse the tubes is required to prevent bundling due to van der Waals interactions. Only noncovalent strategies come into consideration because covalent bond formation on the nanotube wall causes modification of their electronic properties.[100] The use of surfactants (sodium dodecyl sulphate (SDS)) delivers dispersions of high concentration (>1 mg/mL) in water[101]. Unfortunately, this method allows neither sorting of metallic and semiconducting tubes nor sorting by diameter. Density-gradient ultracentrifugation using a bile acid salt (e.g., sodium cholate)[102] or single-stranded deoxyribonucleic acid (ssDNA) wrapped SWNTs[103,104], dielectrophoresis[105], and gel chromatography[106] have all proved effective for sorting SWNTs.

An efficient and simple way to both disperse and sort SWNTs is through the use of different conjugated polymers and block copolymers.[107–111] The conjugated backbone of the polymer wraps around the nanotube wall through van der Waals interactions, while the side chains support dispersion of isolated hybrids in common organic solvents. In 2011 Ozawa *et al.* were able to produce a 97% enriched dispersion of (6,5) SWNTs using a copolymer of 9,9-dioctylfluorenyl-2,7-diyl and bipyridine (PFO-BPy) as a solubilizer.[112] A summary of the performance of sorting polymers is given in Refs. 88 and 99. Photoluminescence quantum yieldss (PLQYs) showed that selection by sorting polymers is increased by an order of magnitude compared to the use of surfactants.[113] Sorting small band gap nanotubes with photoactive polymers would be a straightforward approach to the production of polymer-SWNT thin films for OPVs.

The effectiveness of the physisorption, that is, the optimization of $\pi - \pi$ interactions with the nanotube and following its dispersion in a solvent, depends on a complex interplay between the conjugated polymer's main chain structure, its chain length, and the length and structure of its side chains.[88,99] So far, there is no recipe for producing polymers with specific sorting abilities, since the sorting process itself is still not completely understood. To gain a deeper insight it is important to know (1) the supramolecular structure of the polymer-nanotube hybrid and (2) which electronic interactions play a role. The supramolecular structure could reveal how efficient wrapping depends on the polymer main chain structure and the tube diameter, whereas the kind of electronic interactions could identify whether selective sorting relies on the nanotube's electronic band structure and electronic density.

Molecular dynamic simulations of polymer–SWNT conjugates showed that 9,9-dioctylfluorenyl-2,7-diyl (PFO) prefers to wrap.[114] In addition, the hybrids show more stable wrapping with high chiral angle tubes. In other

studies, the efficient wrapping is linked to the number of polymer repetition units[115], their arrangements and conformation[116], or stiffness[117]. Still, modelling of such large and computationally demanding systems, including all possible conformations and solvent effects, is rather difficult. Moreover, the energy surface of the van der Waals interaction within the polymer–SWNT interface is rather flat.[118] For this reason we take an alternative approach to studying polymer–SWNT junctions. By modelling a polymer using oligomers we can describe the heterojunction as a periodically repeated oligomer–SWNT unit. To ensure an accurate description of the polymer, it is important to have an oligomer unit that describes the physical properties of the polymer as closely as possible. In the case of photoactive polymers this implies a similar absorbance spectrum. Linear dielectric response (LDR) time-dependent density functional theory (TDDFT) calculations within the random phase approximation (RPA) is useful and efficient tool for simulating absorbance spectra of molecules by extracting excitation energies from transitions in the molecule's ground-state.[119,120] We show that the spectrum of copolymer PFO-BPy can be properly modelled by sandwiching the PFO unit between the pyridine (Py) units, and that already the monomer copolymer of pyridine, 9,9-dioctylfluorenyl-2,7-diyl and pyridine (Py-PFO-Py) describes the polymer qualitatively good description of the polymer.[121]

1.2 Supramolecular Structure Evaluation of Polymer–SWNT Heterojunctions

Scanning electron microscopy (SEM) and atomic force microscopy (AFM) have produced high resolution and high contrast images of nanoscale structures such as carbon nanotubes.[127,128] Nevertheless, resolving in detail polymer–SWNT conjugates has not yet been achieved. Shea *et al.* analyzed the orientation of the polymer backbone with respect to the SWNT axis using anisotropic fluorescence spectroscopy.[129] The angle-dependent emission yielded adsorption angles of 12 to 17 degrees between the SWNT axis and the PFO polymer backbone. This is quite close to a parallel alignment and implies only a loose wrapping of the SWNT by the polymer.

With less technical effort and no need for advanced technical equipment, the SWNT–polymer angle can also be measured using polarized angle-dependent absorption spectroscopy. This experiment is performed with a common UV/VIS/NIR absorption spectrometer incorporating a broadband polarizer (Glan-Thompson-prism). The orientation of the polymer and the SWNT can then be reconstructed knowing the transition dipole moment (TDM) of the measured absorbance peaks. For SWNTs the TDM of the most intense transitions, e.g from the ground-state to the first excited state in SWNTs (E_{11}), and second excited state, E_{22}, are polarized along the tube axis.[130,131] For conjugated systems it is expected that the TDM is along the conjugated backbone. However, for some polymers the assignment of the different absorbance peaks to the orientation of the backbone proves to be more complicated. With the help of linear response (LR) TDDFT we evaluate the TDM of the transitions of polymer units by plotting a spatially resolved spectrum and explicitly highlighting the involved Kohn-Sham (KS) orbitals within the unit. In so doing we can identify the orientation of PFO-BPy within polymer–SWNT supramolecular structures.

1.3   Modelling Transient Absorption Spectroscopy

Visualization of the ultrafast processes occurring during photoabsorption of the excited state in carbon nanotubes and polymer-nanotube blends displays the mechanisms of exciton generation, diffusion, decay, and splitting into free charge carriers. This data provides an informative basis for making improvements in the device's composition. Most of the energy dissipation and transfer processes occur on a time scale longer than 100 fs.[132] Pump-probe spectroscopy is a powerful tool for studying optical properties and exciton dynamics over the femtosecond to microsecond time domain.[133] With a pulsed laser a molecule's electrons are excited from the ground state to higher energy excited states, while a probing light source with a time delay τ is used to obtain the time-dependent absorption spectra of the excited state with $\lesssim 50$ fs resolution. The collection of a difference absorption spectrum as a function of the delay and pump wavelength, $\Delta A(\tau, \lambda)$, is known as transient spectroscopy. As an example, the size of the exciton and its diffusion in the incoherent regime have been experimentally estimated for (6,5) SWNTs[134] using the phase space filling model.[135] Also, the energy of relaxation from higher energy exciton states to the first exciton E_{11} transition has been measured, yielding a very short decay time of 50 fs. This is a peculiarity of one dimensional systems, such as SWNTs, and the strong coupling to highly energetic optical phonons.[136] The strong electron-phonon coupling is evident in the large Raman cross-section, extensively studied with standard continuous wave techniques. The most intense Raman active modes, radial breathing modes and G modes, have been detected in transient coherent Raman experiments.[137,138]

An added complication is the presence of other photoexcited species, resulting from highly nonlinear phenomena that might occur in SWNTs, besides singlet excitons. For this reason, the interpretation of transient spectra for SWNTs becomes complicated due to contributions of such species, e.g., triplets[77], biexcitons[139,140], trions[141,142], and charge-carrier photogeneration[62,143]. Previous transient absorption measurements[144,145] have found a photoinduced absorption (PA) peak at ~ 950 nm for predominantly (6,5) SWNT samples when pumped in the VIS region. The structure of this PA feature provides direct information about the photoexcitation processes within the SWNT. The structure and origin of this PA peak, and how it depends on the SWNT system, is still an active subject of investigation.

In silico simulations of photon-matter interactions allow the calculation of excitation energies, transition moments, and even the undergoing relaxation processes of the compound. This information can assist with the interpretation of spectroscopic data. TDDFT[146], described in section 2.3, has been routinely used to study the electron dynamics in condensed matter by computing the linear or non-linear response properties of systems in the ground state. For example, the absolute rate of charge separation and recombination at the P3HT:fullerene interface was calculated to be $10^{-11} - 10^{-9} \text{s}^{-1}$ based on the Marcus rate equation[147] and TDDFT calculations.[148,149] Extensive theoretical studies of polymer:fullerene heterojunctions all confirm the formation of an exciplex, an excited polymer:fullerene complex, and an energetic favourable CT state for the electron transfer to the fullerene.[150–155] Even non–equilibrium dynamical processes of a P3HT:fullerene blend were simulated within quantum electrodynamical (QED) TDDFT.[156] For simulating pump-probe experiments it is essential to extend the ground-state TDDFT formalism, since the system is driven out of equilibrium by the initial pulse. In this work, we present a simple method on the basis of ground-state TDDFT to model a transient absorption spectrum of a system pumped in the lowest excited state. From the expansion of the ∇ operator in a locally centered atomic orbital (LCAO) basis set, the dielectric matrix in reciprocal space at $\mathbf{q} \to 0^+$ can be derived.[157] The absorption spectrum is then obtained from the imaginary part of the macroscopic dielectric tensor.[158] This description makes TDDFT calculations of periodically repeated systems significantly faster, making tractable the study of optical and dielectric properties of infinite crystal

structures, isolated or bundled carbon nanotubes, as well as extensive polymer:SWNT bulk systems. As a result, for the first time a transient absorption spectrum of a polymer:fullerene:SWNT blend could be efficiently modelled, which is presented in chapter 3.3. Based on our results, we are able to explain the origin of the PA peak in transient spectra of SWNT samples.

1.4 Modelling Conductance Across Heterojunctions

The internal quantum efficiency (IQE) (see Appendix A) of a type II bulk heterojunction within an OPV device is simply the ratio of free charge carrier generation to photon absorption at a given photon energy.[159] As such, the IQE depends on both the ease of separating electron and holes and the resulting current through the OPV. The former depends on the electron-hole binding, charge transfer from donor to acceptor, and electron-hole recombination, while the later depends on the conductance from donor to acceptor across the bulk heterojunction.

To estimate the relative exciton binding between type II bulk heterojunctions, one may compare the first transition for the isolated acceptor, e.g., the E_{11} transition of a nanotube, with the formation energy $E_f(\uparrow\uparrow)$ of the triplet excited state from the singlet ground state, i.e., their difference in total energy. A much smaller triplet formation energy for the isolated acceptor, $E_f(\uparrow\uparrow) \ll E_{11}$, suggests electron-hole separation may prove difficult. This is the case for SWNTs, where the measured singlet exciton binding is ~ 0.4 eV[48,63–66]. On the other hand, if the triplet formation energy in the bulk heterojunction is smaller than that for the isolated acceptor, this is indicative of hole transfer to the donor for type II bulk heterojunctions. In this way, the triplet formation energy can be used to compare the relative ease or difficulty of electron hole separation and the probability of recombination in bulk heterojunctions.

The ease of electron-hole separation in the bulk heterojunction may also be directly probed by considering the difference in charge transfer from donor to acceptor between the triplet excited state and the singlet ground state.[160,161] However, although a greater charge transfer in the triplet excited state means the electron and hole are separated onto different molecules in the bulk heterojunction, it does not address whether the separated electron and hole are free charge carriers, or remain bound within the junction.

To determine whether separated electrons and holes truly behave as free charge carriers, the degree of scattering, and the resulting current through the OPV, one should compute the conductance across the bulk heterojunction from the donor to the acceptor in the excited state. In particular, one should consider the conductance at the Fermi level of the excited electron/hole to determine the number of free electron/hole carriers.

To study the IQE of different bulk heterojunctions, we carry out density functional theory (DFT) calculations of the excited state formation energy, charge transfer, and zero-bias conductance of prototypical donor–acceptor bulk heterojunctions in the singlet ground state and triplet excited state. Additionally, we calculate the Landauer-Bütticker conductance of electron and hole charge carriers from donor to acceptor across the bulk heterojunction based on the DFT tight-binding Hamiltonians using a multiterminal implementation[162] of the non-equilibrium Green's function (NEGF) method[163–166]. We find a dependence of the conductivity on the level alignment, which demonstrates the importance of considering the hybridization of donor–acceptor levels in the excited state. By improving the level alignment of the polymer and SWNT through the use of larger band gap SWNTs, one may obtain a dramatic improvement in OPV efficiency.

As we see, the optimization of SWNT OPVs requires a combined theoretical and experimental approach to reveal the supramolecular structure of polymer–SWNT heterojunctions, to differentiate between the different adsorption processes and interfacial interactions, and to understand the photoelectric and transport processes within polymer–

SWNT blends. Only in so doing can we take full advantage of the outstanding physical properties of SWNTs and develop highly efficient OPVs. The following section provides a short overview of the content of the thesis.

1.5   Overview

This thesis begins by providing the reader an introduction to the theoretical and computational background in **chapter 2**. In section 2.1 DFT is presented, which allows one to find the ground-state energy using the electron density distribution. We will see that DFT is a useful alternative to many-body wavefunction approaches based on the Schrödinger equation (section 2.1.1), which are intractable for the many-electron systems we are interested in. Another wavefunction approach is the Hartree-Fock approximation, which is discussed in section 2.1.2. It describes the electronic structure of atoms by a set of self-consistent single particle equations. In section 2.1.3 we will learn about the Hohenberg-Kohn Theorem, which states that the ground state density of a bound system of interacting electrons in some external potential is uniquely determined. On this basis we rely on the KS self-consistent equations, which allows one to find the exact ground state energy by varying trial densities (section 2.1.4). The only missing piece to the exact theory is the form of the exchange and correlation (xc) term, which needs to be approximated for many-electron systems. We will present the xc functionals used in this work in section 2.1.5.

In section 2.2, we will address the descriptions and parameters that are used for the calculation of extended systems. For example, we can describe particles in a periodically repeating environment using Bloch's Theorem (section 2.2.1). Motivated by Bloch's Theorem, we can calculate periodically repeated systems by expanding the KS equations in plane-waves, both within and without the unit cell, as we will show in section 2.2.2. In section 2.2.3 the reader becomes familiarized with the real-space description of the wavefunctions, which makes it possible to perform accurate calculations for large systems due to simple and very scalable parallelization through domain decomposition. Further, LCAOs are introduced as a basis set of atomic orbital-like functions that allow more efficient calculations compared to grid-based wavefunctions, although the accuracy depends on the quality of the chosen basis set (section 2.2.4). Finally, the projector augmented wave (PAW) method allows us to describe the all-electron (AE) wavefunction near the core of the atom while using smooth pseudo (PS) wavefunctions to describe their spatial extent (section 2.2.5).

The reader will be introduced to LR-TDDFT in section 2.3. First, we will take a look at the time-dependent extension to the KS equations, which is a valid expression according to the Runge-Gross theorem (section 2.3.1). However, we are only interested in optical properties such as excitation energies, transition moments, and polarizabilities. For weak external perturbations these can be obtained simply from linear response theory within the KS framework as we will see in section 2.3.2. Further, we will illustrate in section 2.3.3 how to calculate the absorption spectrum of extended systems using the imaginary part of the macroscopic dielectric function obtained from LDR-TDDFT-RPA.

In section 2.4 we will discuss how to compute the conductance, that is, the electronic transport properties, of nanosystems. We will derive the Landauer formula in section 2.4.1, which describes a current through a single-level channel. In section 2.4.2 we provide a basic introduction to two-point Green's functions that represent the electron propagation between points in space and time. Finally, in section 2.4.3, we will show how to calculate the Landauer-Bütticker conductance of an electron passing through a polymer-carbon nanotube junction using the NEGF method.

Sections in 2.5 provide paths to calculate charge distributions in heterojunctions, which gives an estimation of the charge transfer state at the donor–acceptor interface. The reader will learn how the electron and hole densities can be evaluated in section 2.5.1 and that the charge transfer between molecules is calculated using the Bader charge analysis (section 2.5.2).

Section 2.6 provides a guide to the fundamentals of SWNTs. The reader becomes familiar with how the symmetries of SWNT structures are classified into achiral and chiral (non-symmorphic) nanotubes, and how the former can be further separated into zigzag and armchair nanotubes (section 2.6.1). Further, it is shown how the band structure of nanotubes may be derived from the band structure of graphene in section 2.6.2. Finally, the reader will learn what makes nanotubes metallic or semiconducting in section 2.6.3.

Chapter 3 encompasses all the results and discussion contained within this thesis. We begin with the modelling of polymers from oligomers in section 3.1. To perform computational studies on large polymer–carbon nanotube systems, we must first find an oligomer with the minimal size of a polymer building block that reproduces the properties of interest of the full polymer. Only in so doing can we hope to reduce the computational costs sufficiently to subsequently model complex hybrid systems. Our results show that by using LDR-TDDFT-RPA the optical properties of PFO-BPy can be efficiently described by just the monomer unit Py-PFO-Py, where the PFO is sandwiched between two Pys.

We will see in section 3.2 that we can make use of such a polymer building block to identify the transition dipole moment of a polymer. This is useful in combination with angle-dependent polarized absorption spectroscopy to evaluate the supramolecular structure of the polymer–SWNT heterojunction by making use of the polarization of the material in a cristalline matrix.

In section 3.3 we discuss the modelling of photoinduced transient absorption in carbon nanotube systems. It is unclear what is causing the PA peak in transient pump-probe experiments of carbon nanotubes (systems) and how it can be used to interpret the electron dynamics of polymer-carbon nanotube junctions. It has previously been suggested that the PA peak arises due to a subsequent excitation of the carbon nanotube's excited electron. We modelled transient spectra from a ground and excited state difference spectra both obtained from LDR-TDDFT-RPA. Our results suggest that a subsequent excitation occurs next to the pumped exciton, which involves an electron in the valence band of the opposite spin channel. This excitation is blue shifted in energy due to gap widening as a result of the charge loading in the other spin channel.

In section 3.4 we present the modelling of charge transport across heterojunctions. In this case we consider not only polymer–carbon nanotube junctions, but as well polymer–C_{60} junctions. We aim to provide insight into the IQEs of OPVs consisting of different donor–acceptor materials by comparing the excited state formation energy, charge transfer, and zero-bias conductance within the Non-Equilibrium Green's Function method in the ground and excited state. We find the (6,5) and (10,5) SWNTs, with their smaller band gaps, have quite low conductivities, whereas for (6,4) SWNTs the conductivity is significantly larger.

In **chapter 4** we will discuss the conclusion and the outlook of this work. In section 4.1 we begin with the conclusions made from modelling polymers from oligomers. The good representation of the optical properties of the polymer PFO-BPy by the monomer unit Py-PFO-Py is due to the weak π-conjugation between the ortho-linked bipyridines. This suggests that excited state transitional are localized on the Py-PFO-Py unit. Altogether, we demonstrate that LDR-TDDFT-RPA is a good tool for ensuring that the electronic properties of a full polymer are well represented by a polymer subunit.

In section 4.2 we conclude that angle-dependent polarized absorption spectroscopy combined with LR-TDDFT offers a good tool to evaluate the supramolecular structure of a polymer–SWNT heterojunctions. Our results suggest that the TDM of the Py-PFO-Py unit is along the backbone of the polymer. Further, the angle-dependent polarized absorption spectrum of PFO-BPy sorted (6,5) SWNT shows that both, the polymer and the SWNT, have the same angle devolution and therefore polarization. From all our results we can suggest that the polymer PFO-BPy is alinged stretched out parallel to the tube axis, not wrapped as initially thought.

The conclusion of modelling photoinduced transient absorption in carbon nanotube systems are summarized in section 4.3. We conclude that due to the size of the extended system, two excitons may coexist next to each other. Hence, the blue shifted probe bleach causes the PA peak in the transient spectrum. The intensity and the visibility of the PA peak depends on the charge carrier density, but mainly on the peak width. The widths can be significantly increased due to charge transfer to other tubes. Altogether, we think that the PA peak may be used as a qualitative measure of exciton density and charge transfer within SWNT systems.

In section 4.4 we conclude from the results of our modelling of transport across heterojunctions that it is important to consider the hybridization of donor–acceptor levels in the excited state, and the resulting dependence on level alignment of the conductivity. As well, we conclude that by improving the level alignment of the polymer and SWNT through the use of larger band gap SWNTs, one may obtain a dramatic improvement in OPV efficiency.

Finally, we want to point out some potential sources for the low efficiencies of SWNT containing OPVs and approaches for possible improvements. As well, we will discuss the limitations of the applied theoretical tools for modelling optical and electronic processes in polymer–carbon nanotube heterojunctions and will suggest next steps for further studies.

Atomic units ($\hbar = m_e = e = a_0 = 1$) have been used throughout unless stated otherwise.

Chapter 2

Theoretical & Computational Background

2.1 Density Functional Theory

The Schrödinger equation is the fundamental equation from which one can extract all physical observables for a nonrelativistic quantum system. While the time-dependent Schrödinger equation describes the dynamics of the system's quantum states, the stationary solutions of the time-independent equation give the discrete energy levels of a system. Unfortunately, the many-electron wavefunction $\Psi(\mathbf{r}_1, \ldots, \mathbf{r}_N)$ depends on every electron's position $\mathbf{r}_1, \ldots, \mathbf{r}_N$. Thus, solving the electronic Schrödinger equation is far too complex for systems with many electrons N, especially for the bulk heterojunctions we are interested in herein. The development of computational methods that determine the ground-state energy as a functional of the electron density distribution $n(\mathbf{r})$, that depends only on the 3 coordinate $\mathbf{r}(x, y, z)$, made quantum mechanical calculations accessible to scientific fields studying nanoscale systems. One of the most used theories for the simulation of electronic structures and quantum phenomena at the nanoscale is the Density Functional Theory [167]. In the following sections we will illustrate how the ground-state energy and the electronic structure of a system with N electrons in an external potential (e.g. the electrostatic potential due to the nuclei) is calculated.

In section 2.1.1 we begin with the fundamentals of the Schrödinger equation and the limitations of wavefunction methods. We find that the Hartree-Fock Approximation, a wavefunction based method, can be simplified by using single-electron equations to represent the many-electron wavefunction $\Psi(\mathbf{r}_1, \ldots, \mathbf{r}_N)$ in section 2.1.2. The underlying basis of Density Functional Theory is explained in section 2.1.3, where the most important breakthough is the description of a variational principle based on trial densities $\tilde{n}(\mathbf{r})$ instead of trial wavefunctions $\tilde{\Psi}(\mathbf{r}_1, \ldots, \mathbf{r}_N)$. In section 2.1.4 the reader is familiarized with the Kohn-Sham (KS) Self-consistent Field Theory, where the KS System combines single-electron equations and the trial-density-based variational principle. In section 2.1.5 approximations to the exact exchange and correlation (xc) functional are introduced. A proper description of the exact xc functional is the missing piece to the exact theory. We begin with the local density approximation (LDA) and continue with the extension of the LDA, the generalized gradient approximation (GGA). Finally, the xc functionals used for our projects are the GGA Perdew-Burke-Ernzerhof xc functional (PBE) and the van der Waals xc functional (vdW-DF). The latter has an additional long-range interaction term, which is needed to describe van der Waals interactions of close lying molecules within bulk heterojunction.

2.1.1 The Schrödinger Equation and the Many-body Problem

The state of a molecular system, which is determined by the positions of the nuclei and the electrons, can be represented by its corresponding wave vector state Ψ,

$$\Psi(\mathbf{r}_1, s_1, \ldots, \mathbf{r}_N, s_N; \mathbf{R}_1, S_1, \ldots, \mathbf{R}_{N_{n^+}}, S_{N_{n^+}}), \tag{2.1}$$

which is a function of N electronic coordinates $\mathbf{r}$ and spins s and N_{n^+} nuclear coordinates $\mathbf{R}$ and spins S. Further, the electronic and nuclear kinetic energies and interactions are described by the many-body Hamiltonian $\hat{H}$,

$$\hat{H} = -\frac{1}{2}\sum_i \nabla_{\mathbf{r}_i}^2 - \sum_i \sum_I \frac{Z_I}{|\mathbf{r}_i - \mathbf{R}_I|} + \frac{1}{2}\sum_{i \neq j} \frac{1}{|\mathbf{r}_i - \mathbf{r}_j|} - \frac{1}{2}\sum_I \frac{1}{M_I}\nabla_{\mathbf{R}_I}^2 + \frac{1}{2}\sum_{I \neq J} \frac{1}{|\mathbf{R}_I - \mathbf{R}_J|}, \tag{2.2}$$

where $\nabla_{\mathbf{r}}^2 = \frac{\partial^2}{\partial x^2} + \frac{\partial^2}{\partial y^2} + \frac{\partial^2}{\partial z^2}$ and $\nabla_{\mathbf{R}}^2 = \frac{\partial^2}{\partial X^2} + \frac{\partial^2}{\partial Y^2} + \frac{\partial^2}{\partial Z^2}$ are the Laplacians of the electronic and nuclear coordinates, $\mathbf{r}$ and $\mathbf{R}$, respectively, and Z and M are the atomic number and mass of the nucleus, respectively. The first term of the many-body Hamiltonian $\hat{H}$ is the electronic kinetic energy operator $\hat{T}_{e^-}$, the second term is the potential energy arising from the attraction of the negatively charged electrons with the the positively charged nuclei $V_{e^- n^+}$, the third term is the electron-electron interaction $V_{e^- e^-}$, the fourth term is the nuclear kinetic energy operator $\hat{T}_{n^+}$, and the last term is the nuclear-nuclear repulsion $V_{n^+ n^+}$. So we can write the many-body Hamiltonian $\hat{H}$ simply as

$$\hat{H} = \hat{T}_{e^-} - V_{e^- n^+} + V_{e^- e^-} + \hat{T}_{n^+} + V_{n^+ n^+}. \tag{2.3}$$

If we now are interested in the system's evolution over time t, we have to take a look at the linear transformation of the vector state Ψ under the operation of the Hamiltonian $\hat{H}$,

$$\hat{H}\Psi(\mathbf{x}, t) = i\hbar \frac{\partial}{\partial t}\Psi(\mathbf{x}, t), \tag{2.4}$$

where i is the imaginary number, $\hbar = \frac{h}{2\pi}$ is the reduced Planck constant h, and for simplicity all nuclear, electronic, and spin coordinates are represented by $\mathbf{x} \equiv \{\mathbf{r}_1, s_1, \ldots, \mathbf{r}_N, s_N; \mathbf{R}_1, S_1, \ldots, \mathbf{R}_{N_{n^+}}, S_{N_{n^+}}\}$. This differential wave equation is known as the time-dependent Schrödinger equation[168], from which all physical observables for non-relativistic quantum systems can be deduced. However, in this work we are only interested in the electronic structures and ground-state energies. Since the nuclei are much heavier than electrons and therefore moving much slower, we may assume the nuclei remain stationary as the electrons relax. Hence, we can separate the complete many-body electron-nuclear wavefunction Ψ into an electronic and a nuclear part as follows,

$$\Psi(\mathbf{r}_1, s_1, \ldots, \mathbf{r}_N, s_N; \mathbf{R}_1, S_1, \ldots, \mathbf{R}_{N_n^+}, S_{N_n^+}) = \Psi_{e^-}(\mathbf{r}_1, s_1, \ldots, \mathbf{r}_N, s_N)\Psi_{n^+}(\mathbf{R}_1, S_1, \ldots, \mathbf{R}_{N_{n^+}}, S_{N_{n^+}}), \tag{2.5}$$

where Ψ_{e^-} and Ψ_{n^+} are electronic and nuclear wavefunctions, respectively. The separability of the electron-nuclear wavefunction is known as the Born-Oppenheimer approximation (BOA)[169]. The electronic wavefunction then depends on the nuclear coordinates only parametrically, through the potential. The full many-body Hamiltonian than reduces to the electronic Hamiltonian $\hat{H}_{e^-}$,

$$\hat{H}_{e^-} = -\frac{1}{2}\sum_{i=1} \nabla_{\mathbf{r}_i}^2 + \frac{1}{2}\sum_{i \neq j} \frac{1}{\mathbf{r}_i - \mathbf{r}_j} + V_{ext}^{\mathbf{R}_1, \ldots, \mathbf{R}_{N_{n^+}}}(\mathbf{r}_1, \ldots, \mathbf{r}_N), \tag{2.6}$$

where V_{ext} is the potential due to the external environment, e.g. the electrostatic potential due to the nuclei. If we are only interested in finding the ground-state energy E of a molecular system with fixed nuclear positions, we do not

need to consider a time-dependent evolution. In the time-independent case we simply obtain an eigenvalue equation. Thus, from the stationary solutions of the N-electron time-independent Schrödinger equation,

$$\hat{H}_{e^-}\Psi_{e^-}(\mathbf{r}_1, s_1, \ldots, \mathbf{r}_N, s_N) = E\Psi_{e^-}(\mathbf{r}_1, s_1, \ldots, \mathbf{r}_N, s_N), \tag{2.7}$$

we can obtain the ground-state energy E_0 consisting of the N lowest electronic eigenenergies.

One way to find the ground-state energy E_0 is by applying the variational principle [170], where the expectation value of the Hamiltonian $\hat{H}$ for a guessed trial wavefunction $\tilde{\Psi}$ is equal to or an upper bound for the true ground state energy E_0. Hence, the ground state energy E_0 of any state Ψ can be approached by varying over trial functions $\tilde{\Psi}$ using the minimal principle for the expectation value E_0,

$$E_0 \leq \frac{\langle\tilde{\Psi}|\hat{H}|\tilde{\Psi}\rangle}{\langle\tilde{\Psi}|\tilde{\Psi}\rangle}. \tag{2.8}$$

Since the quality of the trial function $\tilde{\Psi}$ depends on some parameters $p_1, p_2, \ldots, p_M$, the energy is a function of these parameters, $E = E(p_1, p_2..p_M)$. To achieve an acceptable accuracy, there is a number ($3 \leq p \leq 10$) of parameters needed. Including just spatial coordinates, the number of parameters required for N electrons is

$$M = p^{3N}, 3 \leq p \leq 10. \tag{2.9}$$

The exponential in equation 2.9 severely limits the range of N that can be simulated. This is known as the exponential wall.

For example, let us imagine a calculation including one carbon atom with 6 electrons. Considering the case where storing one parameter requires 8 bits, we need $10^{3\times6} = 10^{18}$ bytes to store this many parameters. This is almost a million Terabytes of memory. We clearly see that the memory requirements alone make solving this problem unfeasible. However, the wavefunction contains more information than we need. So, as we will see in the next sections, we can avoid using the (N-electron) wavefunctions if we only need the ground state energy of the system.

2.1.2 The Hartree-Fock Approximation

In 1928, Douglas R. Hartree [171] proposed describing the electronic structure of atoms by a set of self-consistent single particle equations. However, single particle equations can not be formed that easily since the eigenfunctions cannot be written as a Hartree Product of the orbitals,

$$\Psi(\mathbf{r}_i, s_i; \mathbf{r}_j, s_j) \neq \psi(\mathbf{r}_i, s_i)\psi(\mathbf{r}_j, s_j). \tag{2.10}$$

Hence, the Hamiltonian is not separable. This is due to the fact that we can not distinguish identical particles because the wave function Ψ changes only by a phase factor (e.g. + for bosons and for fermions) when two particles are interchanged. Thus, an exchange of electrons i and j in the spin orbitals leads to a change in the symmetry of the wavefunctions as follows

$$\Psi(\mathbf{r}_i, s_i; \mathbf{r}_j, s_j) = -\Psi(\mathbf{r}_j, s_j; \mathbf{r}_i, s_i). \tag{2.11}$$

Two years later, Vladimir A. Fock[172] suggested using a Slater determinant of individual one-electron eigenfunctions,

$$\Psi^{\text{HF}}(\mathbf{r}_1, s_1; \mathbf{r}_2, s_2; \ldots; \mathbf{r}_N, s_N) = \frac{1}{\sqrt{N!}} \begin{vmatrix} \psi_1(\mathbf{r}_1, s_1) & \psi_2(\mathbf{r}_1, s_1) & \cdots & \psi_N(\mathbf{r}_1, s_1) \\ \psi_1(\mathbf{r}_2, s_2) & \psi_2(\mathbf{r}_2, s_2) & \cdots & \psi_N(\mathbf{r}_2, s_2) \\ \vdots & \vdots & \ddots & \vdots \\ \psi_1(\mathbf{r}_N, s_N) & \psi_2(\mathbf{r}_N, s_N) & \cdots & \psi_N(\mathbf{r}_N, s_N) \end{vmatrix}, \tag{2.12}$$

which is a linear combination of the Hartree Products. Following the Hartree-Fock Approximation results in a single electron Schrödinger-like equation,

$$\hat{F}\psi_i(\mathbf{r}_i, s_i) = \epsilon_i \psi_i(\mathbf{r}_i, s_i), \tag{2.13}$$

where ψ_i are the N single-electron wavefunctions, ϵ_i their orbital energies, and $\hat{F}$ is the one-electron Fock operator,

$$\hat{F} = \sum_i^N \left(-\frac{1}{2}\nabla_{\mathbf{r}_i}^2 + \sum_k^{N_k} \frac{Z_k}{|\mathbf{r}_i - \mathbf{R}_k|} \right) + \sum_i^N \left(\int \frac{n(\mathbf{r}_j)}{|\mathbf{r}_i - \mathbf{r}_j|} d^3\mathbf{r}_j + \hat{V}_x(\mathbf{r}_i, s_i) \right). \tag{2.14}$$

The first two terms of the Fock operator $\hat{F}$ consist of the sum of the non-interacting kinetic energy and the external potential caused by the Coulomb attraction of the ith electron to all nuclei, with their charges given by their atomic numbers Z_k. The third term is the Coulomb repulsion of the ith electron to the other electrons in terms of their average density distribution $n(\mathbf{r}_j)$, also called a mean field description. The last term is the exchange potential, here written as integral operator,

$$\hat{V}_x[\psi_i](\mathbf{r}_i, s_i) = \left[\sum_{j=1}^N \int \psi_j^*(\mathbf{r}_j, s_j) \frac{1}{|\mathbf{r}_i - \mathbf{r}_j|} \psi_i(\mathbf{r}_j, s_j) d^3\mathbf{r}_j \right] \psi_j(\mathbf{r}_i, s_i), \tag{2.15}$$

which has no classical representation. This description of the ith electron depends on the wavefunctions of all other electrons. It represents the interchange of identical electrons and leads to an exchange of variables in two spin orbitals. Therefore, the Hartree-Fock methods treats the exchange interaction between electrons with the same spin exactly. As well, the Hartree-Fock (HF) method is self interaction free, since the Coulomb and exchange terms cancel each other exactly for the case of an electron interacting with itself.

If we want to know the ground-state energy E_0 within the HF Approximation, we begin by constructing the one-electron wavefunction ψ_i from a complete set of M basis functions ϕ_μ, with the linear combination of atomic orbitals *ansatz*,

$$\psi_i = \sum_{\mu=1}^M c_{i,\mu} \phi_\mu. \tag{2.16}$$

The coefficients $c_{i,\mu}$ can be obtained from the variational principle. From the general eigenvalue problem we obtain the following equations, known as Roothaan-Hall equations[173,174],

$$\sum_{\mu,\nu=1}^M c_{i,\mu}^* c_{i,\nu} \langle \phi_\mu | \hat{F} | \phi_\nu \rangle = \epsilon_i \sum_{\mu,\nu=1}^M c_{i,\mu}^* c_{i,\nu} \langle \phi_\mu | \phi_\nu \rangle, \tag{2.17}$$

where $\hat{F}_{\mu,\nu} = \langle \phi_\mu | \hat{F} | \phi_\nu \rangle$ are the Fock matrix elements and and $S_{\mu,\nu} = \langle \phi_\mu | \phi_\nu \rangle$ the overlap matrix elements. The nontrivial solutions of these equations

$$[\hat{F}_{\mu,\nu} - \epsilon_i S_{\mu,\nu}] = 0, \tag{2.18}$$

give as diagonal elements M eigenvalues ϵ, of which the N lowest eigenvalues correspond to the occupied states.

However, using a wavefunction based method for many electron systems is computationally very time consuming. Additionally, the mean field treatment of the Coulomb repulsion neglects the instantaneous electron correlation. This results in the "Hartree-Fock-limit", an upper bound of the *exact* energy. Especially for chemical bonding, a proper description of the correlation energy is significant. Hence, for calculations of binding energies, a more accurate description including a correlation term is preferable.

2.1.3 Hohenberg-Kohn Variational Principle

We already know that the many-body wavefunction, if known, can be used to evaluate all observables for a physical system. However, we are not interested in all physical properties, but only a few. Specifically, we are interested in the system's ground state energy and electronic structure. We have seen that the ground-state energy can be found by applying the Rayleigh-Ritz minimal principle[170]. Applying this to an electronic Schrödinger(-like) equation and considering only the spatial coordinates $\mathbf{r}_i$ yields

$$E_0 \leq \frac{\langle \tilde{\Psi}(\mathbf{r}_1 \ldots, \mathbf{r}_N)|\hat{H}|\tilde{\Psi}(\mathbf{r}_1 \ldots, \mathbf{r}_N)\rangle}{\langle \tilde{\Psi}(\mathbf{r}_1 \ldots, \mathbf{r}_N)|\tilde{\Psi}(\mathbf{r}_1 \ldots, \mathbf{r}_N)\rangle}, \tag{2.19}$$

where $\tilde{\Psi}(\mathbf{r}_1, \ldots, \mathbf{r}_N)$ is a normalized trial wavefunction which yields an electron density

$$n(\mathbf{r}) = N \int |\Psi(\mathbf{r}_1, \ldots, \mathbf{r}_N)|^2 \mathrm{d}\mathbf{r}_2 \ldots \mathrm{d}\mathbf{r}_N. \tag{2.20}$$

So, it should be possible to obtain an equation in terms of the electron density $n(\mathbf{r})$ alone. This reduces the problem from one in terms of the many-electron wavefunction $\Psi(\mathbf{r}_1, \ldots, \mathbf{r}_N)$, with $3N$ coordinates, to one in terms of the electron density $n(\mathbf{r})$, which is dependent on only a single three dimensional coordinate $\mathbf{r}$. In exchange we will lose all other information contained in the many-body wavefunction.

Already in the Thomas-Fermi Theory[175,176] we can find a simplified one-to-one implicit relation between the effective potential v_{eff} and the density distribution $n(\mathbf{r})$, considering the electrons moving in a given external potential $v_{ext}(\mathbf{r})$,

$$n(\mathbf{r}) = \gamma(\mu - v_{eff}(\mathbf{r}))^{3/2} \tag{2.21}$$

where μ is the $\mathbf{r}$-independent chemical potential, $\gamma = \frac{1}{3\pi^2}(\frac{2m}{\hbar^2})^{3/2}$, and v_{eff} is the effective potential

$$v_{eff} \equiv v_{ext}(\mathbf{r}) + \int \frac{n(\mathbf{r}')}{|\mathbf{r} - \mathbf{r}'|} d^3\mathbf{r}'. \tag{2.22}$$

consisting of the external potential v_{ext} minus the classical electrostatic potential.

On the basis of the Thomas-Fermi Theory, Pierre Hohenberg and Walter Kohn[177] proved by *reductio ad absurdum*, that there does not exist a second effective potential v_{eff} resulting in the same non-degenerate ground state density $n(\mathbf{r})$, Theorem 1.

Theorem 1 (Hohenberg-Kohn). The ground state density $n(\mathbf{r})$ of a bound system of interacting electrons in some external potential $v_{ext}(\mathbf{r})$ is uniquely determined.

In 1964, Hohenberg and Kohn published a formulation of the minimal principle using trial densities $\tilde{n}(\mathbf{r})$. They defined a constrained energy minimum with a fixed $\tilde{n}(\mathbf{r})$ and minimized in a second step over all $\tilde{n}$,

$$E = \min_{\tilde{n}} E_v[\tilde{n}] = \min_{\tilde{n}} \left\{ \int v_{ext}(\mathbf{r})\tilde{n}(\mathbf{r})d^3\mathbf{r} + F[\tilde{n}] \right\}, \tag{2.23}$$

where $F[\tilde{n}]$ represents the sum of the kinetic and interaction energy. $F[\tilde{n}]$ is a universal functional of the density $\tilde{n}$ and requires no knowledge of the external potential $v_{ext}(\mathbf{r})$. This formulation simplified the problem of finding the energy minimum of a $3N$-dimensional wavefunction to finding the minimum of $E_v[\tilde{n}]$ with respect to a three dimensional trial function $\tilde{n}(\mathbf{r})$, although, only when $F[\tilde{n}]$ is well defined.

2.1.4   Kohn-Sham Self-consistent Field Approach

Based on Hartree's idea and knowledge of the unique mapping of $n(\mathbf{r})$ to the external potential $v_{ext}(\mathbf{r})$, Walter Kohn and Leu Sham[178] devised the KS system.

Definition 1 (KS System). The KS system is a fictitious system of non-interacting electrons, which has the same ground state density as the real interacting system.

Now, we can find the ground state density $n(\mathbf{r})$, energy E_0, and forces $\mathbf{F}_I$ by following the self-consistent KS scheme[178] depicted in Figure 2.1. This involves the following five steps:

(1) Making an initial guess $n_0(\mathbf{r})$ for the trial density $\tilde{n}(\mathbf{r})$.

(2) Constructing an effective potential

$$v_{eff}[\tilde{n}](\mathbf{r}) = v_{ext}(\mathbf{r}) + \int \frac{\tilde{n}(\mathbf{r})}{|\mathbf{r} - \mathbf{r}'|} d^3\mathbf{r}' + v_{xc}[\tilde{n}](\mathbf{r}), \tag{2.24}$$

where $v_{ext}(\mathbf{r})$ is the external potential from the nucleus, the second term is the Hartree potential caused by the average density of the electrons, and v_{xc} is the local exchange-correlation potential. The v_{xc} term includes all corrections for the kinetic energies and electron-electron interactions, and thus the difference between the interacting and non-interacting system.

(3) Solving the single-electron Schrödinger equation with effective potential $v_{eff}[\tilde{n}](\mathbf{r})$ to obtain the KS wavefunctions φ_i,

$$\left(-\frac{1}{2}\nabla^2 + v_{eff}[\tilde{n}](\mathbf{r}) - \epsilon_i\right)\varphi_i(\mathbf{r}) = 0. \tag{2.25}$$

(4) Calculating a new trial density $\tilde{n}'(\mathbf{r})$ by summing over the N lowest eigenvalues φ_i,

$$\tilde{n}'(\mathbf{r}) = \sum_{i=1}^{N} |\varphi_i|^2, \tag{2.26}$$

(5) Repeating steps (2), (3), and (4) until the density is converged, that is, $\tilde{n}'(\mathbf{r}) \approx \tilde{n}(\mathbf{r}) \rightarrow n(\mathbf{r})$. This means $\tilde{n}'(\mathbf{r})$ from equation 2.26 is within a defined accuracy of $\tilde{n}(\mathbf{r})$, the latest input density to equation 2.24.

From the ground state density $n(\mathbf{r})$ and eigenvalues ϵ_i, the ground state energy E_0 can be calculated from

$$E_0 = \sum_{i=1}^{N} \epsilon_i + E_{xc}[n] - \int v_{ext}(\mathbf{r})n(\mathbf{r})d^3\mathbf{r} + \frac{1}{2} \iint \frac{n(\mathbf{r})n(\mathbf{r}')}{|\mathbf{r} - \mathbf{r}'|} d^3\mathbf{r}d^3\mathbf{r}'. \tag{2.27}$$

Neither the KS orbital energies ϵ_i nor the KS orbitals φ_i have any physical meaning other than the fact that the energy of the highest occupied orbital ϵ_N relative to the vacuum level gives the ionization energy, and that φ_i gives the true physical density $n(\mathbf{r})$. Other than the fact that an exact expression for v_{xc} can only be obtained for systems with a few atoms so that v_{xc} needs to be approximated for many-electron systems, the KS Theory and its equations are exact.
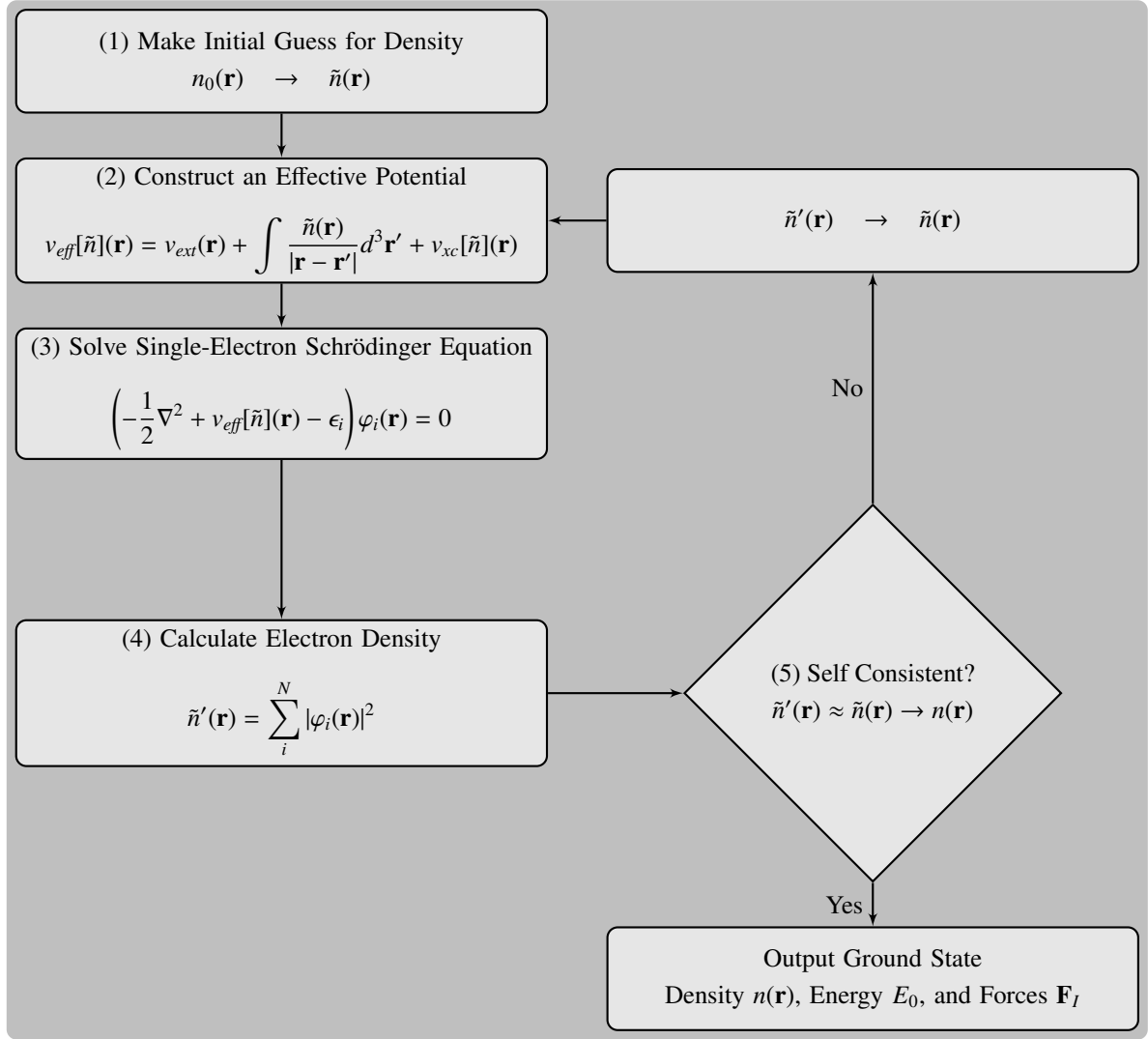
Figure 2.1: Kohn-Sham self-consistent scheme.

2.1.5 Exchange and Correlation Functionals

The xc energy E_{xc} of a particle at position $\mathbf{r}$ depends primarily on the electron density $n(\mathbf{r}')$ at positions $\mathbf{r}'$ near $\mathbf{r}$. More quantitatively, the xc energy depends on the density within a neighbourhood with a radius of the Fermi wavelength $\lambda_F(\mathbf{r}) = 2\pi[3\pi^2 n(\mathbf{r})]^{-\frac{1}{3}}$, the shortest de Broglie wavelength for non-interacting electrons.[179] Therefore, the xc energy is a nearsighted functional of $n(\mathbf{r}')$ and has a quasi-local description,

$$E_{xc}^{\text{LDA}}[n] = \int \epsilon_{xc}^{\text{LDA}}[n]n(\mathbf{r}')d^3\mathbf{r}', \tag{2.28}$$

where $\epsilon_{xc}^{\text{LDA}}[n]$ is the xc energy of a *uniform* electron gas of density n.[178,179] This LDA is obviously exact for a uniform electron gas. But for atomic systems, where the densities are not slowly varying and electron-electron

interaction effects dominate, such as in heavy fermion systems, LDA often fails. Nevertheless, LDA gives use-ful results for most applications with surprising accuracies of 1% for bond-lengths and geometries of molecules and solids. This can be ascribed to the fact that LDA includes a normalization of the exchange-correlation hole $n_{xc}(\mathbf{r}, \mathbf{r}')$ [179]. This means that the exchanged electron density at position $\mathbf{r}$ leaves a hole in the average density $n(\mathbf{r}')$ in comparison to the conditional electron density $g(\mathbf{r}, \mathbf{r}')$

$$n_{xc}(\mathbf{r}, \mathbf{r}') = g(\mathbf{r}, \mathbf{r}') - n(\mathbf{r}'), \tag{2.29}$$

where $g(\mathbf{r}, \mathbf{r}')$ is the conditional density at $\mathbf{r}'$ given that there is one electron at $\mathbf{r}$. The "screening" electron at $\mathbf{r}'$ integrates to one, so that

$$\int n_{xc}(\mathbf{r}, \mathbf{r}')d^3\mathbf{r}' = -1. \tag{2.30}$$

The xc energy E_{xc},

$$E_{xc} = \frac{1}{2} \iint \frac{n(\mathbf{r})\tilde{n}(\mathbf{r}, \mathbf{r}')}{|\mathbf{r} - \mathbf{r}'|} d^3\mathbf{r}d^3\mathbf{r}', \tag{2.31}$$

resulting from the average *xc* hole density $\tilde{n}(\mathbf{r}, \mathbf{r}')$, was proven to be exact for the uniform electron gas. [180–182]

Unfortunately, the LDA potential decays too fast in finite systems, which can lead to a poor description of orbital binding, especially for electron-rich species. This is mainly because the xc energy $E_{xc}[n]$ does not only depend on the density at a given point $\mathbf{r}$ but also on the density nearby, that is, within some neighbourhood $|\mathbf{r}' - \mathbf{r}| \lesssim \lambda_F(\mathbf{r})$. To account for this, the density at $\mathbf{r}'$, $n(\mathbf{r}')$, can be expanded around $\mathbf{r}$,

$$n(\mathbf{r}') \approx n(\mathbf{r}) + (\mathbf{r}' - \mathbf{r}) \cdot \nabla n(\mathbf{r}) + \frac{1}{2}(\mathbf{r}' - \mathbf{r}) \cdot ((\mathbf{r}' - \mathbf{r}) \cdot \nabla)\nabla n(\mathbf{r}) + \cdots. \tag{2.32}$$

Substituting the expansion 2.32 in equation 2.31 (the full derivation is more complex and found in Ref. 178) leads to the gradient expansion

$$E_{xc} = E_{xc}^{\text{LDA}} + \int G_2[n](\nabla n(\mathbf{r}))^2 d^3\mathbf{r} + \int G_4[n](\nabla^2 n(\mathbf{r}))^2 d^3\mathbf{r} + \cdots, \tag{2.33}$$

where $G_2[n]$ and $G_4[n]$ are universal functionals of n. In atomic systems this expansion produced worse results than LDA [183].

Over the years, important progress has been made towards more successful "generalized" gradient approxima-tions, or GGAs. In this work, the density functional theory (DFT) calculations were performed with the GGA functional developed by John P. Perdew, Kieron Burke, and Matthias Ernzerhof (PBE) [184]. This functional has a gradient fitted with parameters, which are fundamental constants and thus not derived from fits of experimental data. Specifically,

$$E_{xc}^{\text{PBE}} = E_{xc}^{\text{LDA}} + \int \left[\kappa \epsilon_x^{\text{LDA}}[n] \left(1 - \left(1 + \frac{\mu}{4\kappa(3\pi^2 n)^{2/3}} \frac{|\nabla n|^2}{n^2} \right)^{-1} \right) + \frac{\beta_c}{16(3n/\pi)^{1/3}} \frac{|\nabla n|^2}{n^2} \right] n(\mathbf{r})d^3\mathbf{r}, \tag{2.34}$$

where $\kappa = 0.804$ to ensure the Lieb-Oxford bound [185] is satisfied [186], $\mu = 0.21951$ to ensure cancellation of the second order xc terms [186], and $\beta_C = 0.0066725$ as derived by Ma and Brueckner [187]. It includes an accurate description of the linear response of the uniform electron gas, correct behaviour under uniform scaling, and a smoother potential.

The vdW-DF xc functional developed by Maxime Dion, H. Rydberg, Elsebeth Schöder, David C. Langreth, and Bengt I. Lundqvist [124] provides an improved description of the binding between molecular fragments at large

distances. The first term of the vdW-DF is the short-ranged correlation, which is evaluated in the local density approximation. The second term is the long-range part of a fully nonlocal correlation functional E_c^{nl},

$$E_c^{nl} = \frac{1}{2} \iint d^3\mathbf{r} d^3\mathbf{r}' n(\mathbf{r})\phi(q|\mathbf{r} - \mathbf{r}'|, q'|\mathbf{r} - \mathbf{r}'|)n(\mathbf{r}'), \qquad (2.35)$$

where $\phi(q|\mathbf{r} - \mathbf{r}'|, q'|\mathbf{r} - \mathbf{r}'|)$ is the vdW-DF kernel, and q and q' are the values of a universal function $q_0(n(\mathbf{r}), |\nabla n(\mathbf{r})|)$ evaluated at the two points $\mathbf{r}$ and $\mathbf{r}'$.[188]

2.2 Modelling Extended Systems

Even though DFT's KS equations are much easier to solve than the full many-body Schrödinger equation, the computational effort of calculating extended systems remains high. For condensed matter systems we can take advantage of their crystal-like structure and model an extended system using its periodically repeated unit cell. Calculations with open boundaries allow one to study extended one, two, or three dimensional structures such as nanotubes, graphene, or bulk systems, respectively. In addition, several numerical approximations can be made to reduce the computational cost even further. Such approximations include the treatment of the core electrons and the region near the atomic nuclei using pseudopotentials and the discretization of the description of the wavefunctions using plane-waves, real-space grids, and localized orbitals. This section provides an overview of the aforementioned approximations, which are all implemented in the GPAW code [125,126].

In section 2.2.1 we use Bloch's Theorem to describe particles in a periodically repeating environment. Bloch's Theorem provides motivation for employing a plane-wave expansion of the KS equations, as described in section 2.2.2. In section 2.2.3 we introduce the real-space description, which makes it possible to perform accurate calculations for large systems due to simple and very scalable parallelization through domain decomposition. In section 2.2.4, locally centered atomic orbital (LCAO) are introduced, a basis set of atomic orbital-like functions, that allow even more efficient calculations compared to grid-based wavefunctions due to the use of very compact basis sets. Finally, in section 2.2.5 we provide an overview of the projector augmented wave (PAW) method, which allows us to describe the all-electron (AE) wavefunction near the core of the atom using smooth pseudo (PS) wavefunctions.

2.2.1 Bloch's Theorem

Particles in a periodically repeated environment, such as in crystals or condensed matter systems, can be represented by a Bravais lattice. The Bravais lattice constructs a certain periodic system under translation of the system's unit cell or supercell by a lattice vector $\mathbf{R}$,

$$\mathbf{R} = N_1\mathbf{a}_1 + N_2\mathbf{a}_2 + N_3\mathbf{a}_3, \tag{2.36}$$

where $\mathbf{a}_\alpha$ are linearly independent vectors that span the lattice, that is, supercell or unit cell vectors, and $N = N_1 N_2 N_3$ gives the total number of unit cells spanned by $\mathbf{R}$.

We can describe electrons in crystal lattices by plane-waves based on the idea of Felix Bloch [189,190] that the periodicity of the lattice also enters in the potential of the system, so that $U(\mathbf{r} + \mathbf{R}) = U(\mathbf{r})$.

Theorem 2 (Bloch's Theorem). The eigenfunctions $\Psi_{n,\mathbf{k}}(\mathbf{r})$ of the wave equation for a periodic potential are the product of a plane wave $e^{i\mathbf{k}\cdot\mathbf{r}}$ times a function $u_{n,\mathbf{k}}(\mathbf{r})$ with the periodicity of the crystal lattice

$$\Psi_{n,\mathbf{k}}(\mathbf{r}) = e^{i\mathbf{k}\cdot\mathbf{r}} u_{n,\mathbf{k}}(\mathbf{r}), \tag{2.37}$$

where $\mathbf{k}$ are the allowed wave vectors in the primitive cell and n is the band index, which corresponds to independent eigenstates of different energies but with the same $\mathbf{k}$.

The wave vectors $\mathbf{k}$ have a unit of inverse length based on the *de Broglie* relation $|\mathbf{k}| = 2\pi/\lambda$. It is convenient to define a reciprocal lattice in $\mathbf{k}$-space that is related to the real space lattice, which we will discuss further in section 2.6.

Wave vectors that differ by a reciprocal lattice vector $\mathbf{k}$ are equivalent, $\mathbf{k} = \mathbf{k} + \mathbf{K}$, in the sense that they characterize the same set of Bloch states $\Psi_{n,\mathbf{k}}(\mathbf{r})$. Thus, any value of $\mathbf{k}$ outside the first Brillouin zone can be

reduced to the first Brillouin zone. The reciprocal lattice vector $\mathbf{K}$ can be composed from the reciprocal space vectors $\mathbf{b}_\beta$ with coefficients M_β,

$$\mathbf{K} = M_1\mathbf{b}_1 + M_2\mathbf{b}_2 + M_3\mathbf{b}_3 \tag{2.38}$$

where the real and reciprocal space vectors are related by $\mathbf{a}_\alpha \cdot \mathbf{b}_\beta = 2\pi\delta_{\alpha\beta}$ ($\delta_{\alpha\beta} = 0$ if $\alpha \neq \beta$ and 1 if $\alpha = \beta$) so that $e^{i2\pi M_\alpha N_\alpha} = 1$.

The Bloch expansion of the KS equations allows us to perform calculations with periodic boundary conditions in three dimensions. Every periodic calculation must be converged with respect to the Brillouin zone sampling, which in our case is a $\mathbf{k}$-point mesh after Monkhorst and Pack[191]. It is based on the idea of an equally spaced mesh in the Brillouin-zone with

$$M_\mathbf{r} = \frac{2\mathbf{r} - q_\mathbf{r} - 1}{2q_\mathbf{r}}, \tag{2.39}$$

where $M_\mathbf{r}$ is the integer of the reciprocal space vector, and $q_\mathbf{r}$ determines the number of $\mathbf{k}$-points in the $\mathbf{r}$-direction. The sums over $\mathbf{k}$ are performed over all Brillouin zone vectors, but can be reduced to sums on the irreducible Brillouin zone by taking advantage of the space group of the lattice. Hence, an integral of a function, $F(\mathbf{k})$, which is $\frac{1}{\Omega_{\text{BZ}}} \int_{\text{BZ}} F(\mathbf{k})d\mathbf{k}$, where Ω_{BZ} is the volume of the Brillouin zone, can be weighted as $\sum_\mathbf{k} w_\mathbf{k} F(\mathbf{k})$, where the sum is over all $\mathbf{k}$-points in the irreducible Brillouin zone and $w_\mathbf{k}$ are the weighting factors corresponding to the original number of $\mathbf{k}$-points of the reducible Brillouin zone. The "rule of thumb" we usually employ for the $\mathbf{k}$-point meshes, e.g., grid spacings, is $\Delta\mathbf{k} < 0.25$ Å^{-1}. In the case of a non-periodic calculation the boundary conditions force both the density and KS wavefunctions to be zero at the boundary, so we include just one $\mathbf{k}$-point, the Γ-point.

We will see in the next section (2.2.2) how just as we made use of Bloch's Theorem for periodic systems to describe the long-ranged behaviour of the KS wavefunctions *outside* the unit cell, we may similarly expand the KS equations into plane-waves to describe their short-ranged behaviour *inside* the unit cell. These methods may be used for calculating periodic systems such as isolated one dimensional nanotubes or three dimensional bulk structures.

2.2.2 Plane-Wave Expansion of the Kohn-Sham Equations

We have seen that we can describe particles in a periodically repeated environment by expanding the wavefunctions into plane-waves. The most natural but not exclusive basis in that case is a plane-wave basis set, which has for a given unit cell with volume Ω the form

$$u_n(\mathbf{r}) = \frac{1}{\sqrt{\Omega}} \sum_\mathbf{G} \tilde{u}_{n,\mathbf{G}} e^{i\mathbf{G} \cdot \mathbf{r}}, \tag{2.40}$$

where the reciprocal lattice vectors are usually denoted by $\mathbf{G}$ and satisfy the periodicity of the lattice by

$$\mathbf{G}_{i,j,k} = \left(i - \frac{M_1}{2}\right)\mathbf{b}_1 + \left(j - \frac{M_2}{2}\right)\mathbf{b}_2 + \left(k - \frac{M_3}{2}\right)\mathbf{b}_3, \tag{2.41}$$

with $0 \leq i < M_1$, $0 \leq j < M_2$, and $0 \leq k < M_3$. To obtain a finite basis, the infinite basis is truncated by defining a cut-off energy E_{cut}.

If we now apply Bloch's theorem on the KS system, we can rewrite the KS wave-functions $\varphi_{n,\mathbf{k}}(\mathbf{r})$ in terms of a plane-wave basis as follows

$$\varphi_{n,\mathbf{k}}(\mathbf{r}) = \sum_\mathbf{G} c_{n,\mathbf{G}}(\mathbf{k}) \frac{1}{\sqrt{\Omega}} e^{i(\mathbf{k}+\mathbf{G}) \cdot \mathbf{r}}. \tag{2.42}$$

The KS equations can then be expressed simply using the Bloch function coefficients $c_{n,\mathbf{G}}(\mathbf{k})$,

$$\sum_{\mathbf{G}'} \hat{h}_{\mathbf{G},\mathbf{G}'}(\mathbf{k}) c_{n,\mathbf{G}'}(\mathbf{k}) = \epsilon_{n,\mathbf{k}} c_{n,\mathbf{G}}(\mathbf{k}), \tag{2.43}$$

where the Hamiltonian $\hat{h}_{\mathbf{G},\mathbf{G}'}$ is a function of the wave vector $\mathbf{k}$. From this it follows that for a given $\mathbf{k}$, we get n different eigenvalues $\epsilon_{n,\mathbf{k}}$, such that the n bands at different $\mathbf{k}$-points describe the band structure of the material. The Hamiltonian $\hat{h}_{\mathbf{G},\mathbf{G}'}$ with $\mathbf{k}$-dependence is

$$\hat{h}_{\mathbf{G},\mathbf{G}'}(\mathbf{k}) = \frac{1}{2}|\mathbf{k} + \mathbf{G}|^2 \delta_{\mathbf{G},\mathbf{G}'} + v_{ext}(\mathbf{G} - \mathbf{G}') + v_H(\mathbf{G} - \mathbf{G}') + v_{xc}(\mathbf{G} - \mathbf{G}'). \tag{2.44}$$

The first term is the kinetic energy term, which is diagonal in reciprocal space. Thus, the kinetic energy can be accessed straightforwardly. The potentials, that is, the external potential $v_{ext}(\mathbf{G} - \mathbf{G}')$, the Hartree potential $v_H(\mathbf{G} - \mathbf{G}')$, and the xc term $v_{xc}(\mathbf{G} - \mathbf{G}')$ are described in terms of their Fourier components. To compute the xc potential $v_{xc}(\mathbf{G} - \mathbf{G}')$ it is more efficient to use the real space density. Since we have a different system of KS equations for each $\mathbf{k}$, we need to sum over all $\mathbf{k}$-point densities in the irreducible Brillouin zone,

$$n(\mathbf{r}) = \sum_{n,\mathbf{k}} w_{\mathbf{k}} |\varphi_{n,\mathbf{k}}(\mathbf{r})|^2, \tag{2.45}$$

with weighting factors $w_{\mathbf{k}}$, and all occupied states n. The density of the nth wavefunction $|\varphi_{n,\mathbf{k}}(\mathbf{r})|^2$ is expanded into plane-waves as follows,

$$|\varphi_{n,\mathbf{k}}(\mathbf{r})|^2 = \frac{1}{\Omega} \sum_{\mathbf{G},\mathbf{G}'} c_{n,\mathbf{G}}^*(\mathbf{k}) c_{n,\mathbf{G}'}(\mathbf{k}) e^{i(\mathbf{G}-\mathbf{G}')\cdot\mathbf{r}}. \tag{2.46}$$

Hence, we just need to know the coefficients of the KS orbitals and convert them to the real space grid using the fast Fourier transform (FFT) algorithm to get the real space density from which we can calculate the xc potential $v_{xc}[n] = \frac{\delta E_{xc[n]}}{\delta n(\mathbf{r})}$. The Hartree potential $v_H(\mathbf{G}) = 4\pi \frac{n(\mathbf{G})}{|\mathbf{G}|^2}$ can easily be obtained from the density in momentum space $n(\mathbf{G}) = \frac{1}{\Omega} \sum_{n,\mathbf{k},\mathbf{G}'} w_{\mathbf{k}} c_{i,\mathbf{G}}^*(\mathbf{k}) c_{i,\mathbf{G}'}(\mathbf{k})$.

Nevertheless, a plane-wave basis imposes periodic boundary conditions, whereas uniform real space grids or localized basis sets can flexibly treat free, mixed and periodic boundary conditions, as we will see in sections 2.2.3 and 2.2.4.

2.2.3   Real-Space Grid Description

Wavefunctions, electron densities, and potentials can be represented by their values at discrete grid points, which makes uniform real-space grids[192–195] a simple discretization tool for the KS and Poisson equations. Both the kinetic energy operator of the KS equations and Poisson's equation contain the Laplacian operator. This can be approximated with high-order finite difference techniques to control the error of the Laplacian. For an orthorhombic unit cell, where $\mathbf{a}_\alpha$ ($\alpha = 1, 2, 3$) are the lattice vectors, with N_α grid points along the three directions, and a grid spacing of $\mathbf{h}_\alpha = \mathbf{a}_\alpha / N_\alpha$, the Laplacian of the kinetic energy is discretized as

$$\nabla^2 \psi(\mathbf{r}) = \sum_{\alpha=1}^{3} \sum_{n=-N}^{N} \frac{c_n^N \psi(\mathbf{r} + n\mathbf{h}_\alpha)}{h_\alpha^2} + O(h_\alpha^{2N}), \tag{2.47}$$

where c_n^N are the Nth order finite difference coefficients for the second derivative expansion. Accuracy of the calculation depends on the finite difference stencil $O(h_\alpha^{2N})$ and can be improved systematically by decreasing the

grid spacing $h = \max_{\alpha} h_{\alpha}$, which is a single convergence parameter. The computational costs of operating on the wavefunction is proportional to the numbers of grid points. Accurate results are normally obtained by combining a grid spacing of $h = 0.2$ Å and a finite difference stencil with $O(h^6)$ error for the kinetic energy.

The advantage of real-space grids over discretizing by plane-wave basis sets lies in their flexible boundary conditions. The boundary conditions can be chosen to be non-periodic for finite systems, periodic for bulk systems, and mixed for one dimensional wires for example. As well, plane-waves are difficult to parallelize efficiently due to the non-local nature of the operations, whereas the real-space grid can be efficiently divided between different processors, called domain decomposition. Since the Laplacian is nearly local, only a minimal amount of communication between processors is required.

2.2.4 Locally Centred Atomic Orbitals

The GPAW code has also implemented LCAO[196], a basis set of atomic orbital-like functions for representing the Hamiltonian instead of on a real-space grid. This is important in situations where the higher accuracy real-space grid is too inefficient and the finite basis of LCAO describes the electronic density sufficiently that is, it spans the space of wavefunctions. The LCAO basis function ϕ centered at atom a has the form

$$\phi_{nlm}^a(\mathbf{r}) = R_{nl}^a(|\mathbf{r} - \mathbf{R}^a|)Y_{lm}(\mathbf{r} - \mathbf{R}^a), \tag{2.48}$$

where n, l, and m are the principal, angular, and magnetic quantum numbers, respectively, $\mathbf{R}^a$ is the position of nucleus a, R_{nl}^a is a radial function which vanishes beyond a certain cut-off radius, and Y_{lm} are the spherical harmonics. We obtain the basis set by solving the radial AE KS equations for the isolated atom after selecting a cut-off radius[196–198]. This gives the localized atomic-like orbitals ϕ^{AE}, from which the basis functions are then obtained using $\phi(\mathbf{r}) = T^{-1}\phi^{AE}(\mathbf{r})$, where T is the transform matrix.

In the LCAO mode the KS pseudo wavefunction $\tilde{\psi}_{n,s}(\mathbf{r})$ for the nth band spin s are expanded using a set of atomic-like orbitals $\phi_{\nu,s}(\mathbf{r})$

$$\tilde{\psi}_{n,s}(\mathbf{r}) = \sum_{\nu} c_{\nu,n,s}\phi_{\nu,s}(\mathbf{r}), \tag{2.49}$$

where $c_{\nu,n,s}$ are the coefficients, which are the quantities we have to minimize and solve for in the eigenvalue problem for the Hamiltonian $H_{\mu,\nu}$, overlap matrix $S_{\mu,\nu}$, and eigenvalues $\epsilon_{n,s}$,

$$\sum_{\nu} H_{\mu,\nu,s}c_{\nu,n,s} = \sum_{\nu} S_{\mu,\nu,s}c_{\nu,n,s}\epsilon_{n,s}. \tag{2.50}$$

The matrix elements then can be expressed as

$$\begin{aligned}\langle\psi_{n,s'}|\nabla|\psi_{m,s}\rangle &= \sum_{\mu\nu} c_{\nu,n,s'}^*c_{\mu,m,s}\Big[\langle\tilde{\phi}_\nu|\nabla|\tilde{\phi}_\mu\rangle + \\ &\sum_{a,i,j} P_{i,n,s'}^{a*}\left[\langle\phi_i^a|\nabla|\phi_j^a\rangle - \langle\tilde{\phi}_i^a|\nabla|\tilde{\phi}_j^a\rangle\right]P_{j,m,s}^a\Big],\end{aligned} \tag{2.51}$$

where $\tilde{\phi}_\nu$ and ϕ_i^a are the pseudo and all-electron LCAOs and $P_{i,n,s'}^{a*}$ are the PAW projectors (see section 2.2.5),

$$P_{i,n,s'}^{a*} = \langle\tilde{\psi}_{n,s'}|\tilde{p}_i^a\rangle, \tag{2.52}$$

of the nth spin s' pseudo KS wavefunction $\tilde{\psi}_{n,s'}$ onto the ith LCAO orbital of atom a.

The use of LCAO basis sets allows us to store the coefficients for each wavefunction in the basis of locally centered atomic orbitals, instead of storing the wavefunction itself at each of the grid points in real space. In comparison, for an isolated C atom, we would have a real space grid of $(10 \text{ Å}/0.2 \text{ Å}/\text{point})^3 = 125\,000$ points per wavefunction, whereas using an LCAO basis yields 13 coefficients. Hence, the efficiency of LCAO is mainly due to the fact that localized functions can provide a very compact basis set.

One modified atomic orbital for each valence electron forms the smallest atomic basis set, the single-zeta (SZ) basis set. Extra radial basis functions with the same angular momentum l (*multiple-zeta*) are constructed for each valence electron using the split-valence technique[199], that is, matching a polynomial to the tail of the atomic orbital. Next to the radial flexibility, the angular flexibility of the basis can be improved by adding to the lowest unoccupied angular momentum polarization functions. A double-zeta polarized (DZP) basis set for an atom with 2s and 2p valence electrons, such as carbon, which contains of two radial functions for each valence state, plus a polarization function of type d or f yields a total of 5 distinct radial functions. Each will be degenerate by $2l + 1$, meaning that GPAW will use a total of 13 basis functions to represent the atom during a calculation.

It is an important point that changing the basis set in LCAO calculations does not necessarily provide a systematic means for improving the accuracy of the results, whereas for plane wave and real space calculations, increasing the energy cutoff or reducing the grid spacing almost always provides a more accurate description of the wavefunctions. Normally, DZP basis set results are in good agreement with the grid based values, particularly for structural properties. Cohesive energies are more difficult to describe with a localized basis set. Atomic energies are systematically overestimated, leading to stronger binding. In summary, when we have long range interactions, or wavefunctions are significantly perturbed, so that they cannot be decomposed into atomic orbitals, then using an LCAO basis set will cause problems. This is not the case for real space or plane wave codes, as the spatial distribution of the wavefunctions is unspecified, and much more flexible. The GPAW combines localized basis functions with the PAW method and reuses most of its implementations. Only the evaluation of overlap integrals and matrix elements of the kinetic energy operator are done differently, in the sense that the integrals of the LCAO are expressed in terms of two-center integrals.[199]

We chose for our purposes LCAO DZP basis sets to ensure high efficiency and good accuracy. In addition, the use of a spatially localized basis set, such as LCAO, is a requirement for electron transport calculations within the non-equilibrium Green's function approach, as described in section 2.4.

2.2.5 Projector Augmented Wave Method

Near the nuclei the kinetic energy of electrons is large, resulting in rapid oscillations of the wavefunctions. On the other hand, the large kinetic energy makes the wavefunction "stiff" regarding their response to changes in the environment. Thus, small basis sets are sufficient to represent the wavefunctions in the core, whereas in the bonding region the opposite is true. To describe single-particle AE wavefunctions near the core accurately, grid-based methods require a very fine mesh. The PAW method[200,201] is a linear transformation of the AE wavefunctions, Ψ_n, into PS wavefunctions, $\tilde{\Psi}_n$,

$$\Psi_n = \hat{T}\tilde{\Psi}_n, \tag{2.53}$$

where $\hat{T}$ is the transformation operator,

$$\hat{T} = 1 + \sum_a \sum_i (|\varphi_i^a\rangle - |\tilde{\varphi}_i^a\rangle)\langle\tilde{p}_i^a| \tag{2.54}$$

given in terms of atom-centered AE partial waves, φ_i^a, the corresponding smooth partial waves, $\tilde{\varphi}_i^a$, and projector functions, $\tilde{p}_i^a$ of atom a. The projector functions are localized inside the predefined atom-centered augmentation spheres and are constructed as shown in Ref. 200, where the smooth partial waves, $\tilde{\varphi}_i^a$, are constructed by a smooth continuation of $\tilde{\varphi}_i^a$ such that outside the augmentation spheres the AE partial waves and smooth PS partial waves are equal.

The smooth Coulomb potential is calculated from the PS charge density, which has a Gaussian-type function and the same multipole moments as the AE charge density. The smooth effective potential $\tilde{v}_{eff}$ is additionally smoothed by a zero-potential, that is, a local potential, $\bar{v}^a$ that must be zero outside the augmentation sphere.

$$\tilde{v}_{eff} = \frac{\partial \tilde{E}}{\partial \tilde{n}} = v_H + v_{xc} + \sum_a \bar{v}^a \tag{2.55}$$

where v_H is the Hartree potential and v_{xc} is the xc potential. This zero-potential $\bar{v}^a$ can be used to improve the accuracy of a PAW calculation when using a finite number of partial waves and projector functions. The PAW approximation contains all the information about the nodal structure of wavefunctions near the nuclei. Therefore, it is always possible to reconstruct the AE wavefunctions from the PS wavefunctions. Hence, PAW provides access to the all-electron density, which will integrate to the number of electrons in the system, without the need to partition or separately consider valence and core electrons. This is in an important point for performing Bader calculations, which we will see in section 2.5.2. In essence, the PAW method avoids transferability problems related to the pseudopotential approach.

2.3 Linear Response Time-Dependent Density Functional Theory

To study time-dependent properties such as excited state dynamics we can apply the time-dependent density functional theory (TDDFT), which relates the time-dependent density of the KS system to the corresponding time-dependent potential. Unfortunately, the energy of the time-dependent state cannot be obtained by minimization of the energy functional, so that time-dependent properties need to be calculated in a different way. Herein, we are only interested in optical properties such as excitation energies, transition moments, and polarizabilities. These can be obtained simply from linear response theory within the KS framework, where the non-interacting density-density response function χ^0 relates the induced change in density $n_{ind}(\mathbf{r}, t)$ due to a weak external potential v_{ext} that perturbs the system. The following sections shall describe how we calculate optical properties of extended system. Specifically, we calculate the absorption spectrum from the dielectric matrix within the random phase approximation (RPA).

In section 2.3.1 we extend the KS equations to their time-dependent form, which is a valid expression according to the Runge-Gross theorem. The derivation of the linear response for small perturbations due to weak external potentials is explained in section 2.3.2, where the non-interacting density-density response function χ^0 is the functional derivative of the induced density n_{ind} with respect to the external potential v_{ext}. Finally, we show how the absorption spectrum of extended systems is calculated by reformulating χ^0 in reciprocal space to get the dielectric matrix $\varepsilon_{\mathbf{GG'}}^0$. From the imaginary part of the macroscopic dielectric function, which is the reciprocal of the inverse of the dielectric matrix, the absorption spectrum is obtained.

2.3.1 Runge-Gross Theorem

By extending the Hohenberg-Kohn Theorem, Erich Runge and Eberhard K. U. Gross showed that the time-dependent density $n(\mathbf{r}, t)$ is uniquely determined and the corresponding map from a time-dependent potential $v(\mathbf{r}, t) \rightarrow n(\mathbf{r}, t)$ is invertible.[202]

Theorem 3 (Runge-Gross). *Two potentials, $v(\mathbf{r}, t)$ and $v'(\mathbf{r}, t)$, which differ by more than a purely time-dependent function $c(t)^2$, cannot produce the same time-dependent density, $n(\mathbf{r}, t)$.*

Hence, we can extend the KS equations to a time-dependent form,

$$i\frac{\partial}{\partial t}\varphi_n(\mathbf{r}, t) = \left[-\frac{1}{2}\nabla^2 + v_{eff}(\mathbf{r}, t)\right]\varphi_n(\mathbf{r}, t), \tag{2.56}$$

where $\varphi_n(\mathbf{r}, t)$ are the KS wavefunctions and the Hamiltonian in brackets consisting of kinetic term and the effective potential $v_{eff}(\mathbf{r}, t)$.

Since the total energy is not a conserved quantity in time-dependent systems, it cannot be derived by minimization of the energy functional. Moreover, the full solution of the time-dependent KS equations can be quite demanding for very large systems. Nevertheless, we can calculate time-dependent observables such as excitation energies, polarizabilities or transition moments from the linear response formalism within the KS framework as we will see in the next section.

2.3.2 Linear Response

Let us consider a perturbation of a system by a small external potential, small in the sense that the perturbing external potential v_{ext} is much smaller than the external potential caused from the nuclei $v_{ext} \ll v^0$. The system, which was before t_0 ($t < t_0$) only subject to the nuclear potential, v^0, is after t_0 ($t > t_0$) also subject to the weak perturbation by the potential v_{ext} so that the total external potential is $v_{tot} = v^0 + v_{ext}$. For weak perturbations, we may expand until only the linear term v_{ext}. In the same way, we may expand the density in a perturbative series, such that $n(\mathbf{r}, t) = n^0(\mathbf{r}) + n_{ind}(\mathbf{r}, t)$, where n^0 is the ground-state density for $t < t_0$ and $n_{ind}(\mathbf{r}, t)$ the induced change in density after t_0. We may express the induced change in density $n_{ind}(\mathbf{r}, t)$ in terms of the response of the system to the weak external perturbation v_{ext} as follows,

$$n_{ind}(\mathbf{r}, t) = -i \int_{t_0}^{t} dt' \int d\mathbf{r}' \chi(\mathbf{r},\ t;\ \mathbf{r}', t') v_{ext}(\mathbf{r}', t') = \langle \Psi(t)|\hat{n}(\mathbf{r}, t)|\Psi(t)\rangle - \langle \Psi^0(t)|\hat{n}(\mathbf{r}, t)|\Psi^0(t)\rangle, \tag{2.57}$$

where Ψ^0 and Ψ refer to the ground state and perturbed state, respectively, and $\hat{n}(\mathbf{r}, t)$ is the density operator. The key quantity in equation 2.57 is the density-density response function $\chi(\mathbf{r},\ t;\ \mathbf{r}', t')$, which describes the resulting change in density $n_{ind}(\mathbf{r}, t)$ under the small change of the weak external potential v_{ext},

$$\chi(\mathbf{r}, t; \mathbf{r}', t') = \frac{\delta n_{ind}(\mathbf{r}, t)}{\delta v_{ext}} = -i\langle[\hat{n}(\mathbf{r}, t),\ \hat{n}(\mathbf{r}', t')]\rangle_0, \tag{2.58}$$

that is, the equilibrium average of the commutator of the density operators at $\hat{n}(\mathbf{r}, t)$ and $\hat{n}(\mathbf{r}', t')$, according to the Kubo formula.[203] Looking at equation 2.58 makes it clear that the linear response to a perturbation is not related to the perturbation and only depends on the properties of the sample, in the sense that it relates a given change in external charge density to the resulting change in charge density of the system which does the screening.

Using the equations 2.57 and 2.58, we can derive the non-interacting density-density response function $\chi^0(r, r', \omega)$ in the frequency space for the KS system with effective potential v_{eff},

$$\chi^0(\mathbf{r}, \mathbf{r}', \omega) = \frac{\delta n_{ind}(\mathbf{r}, t)}{\delta v_{eff}} = \lim_{\eta \to 0^+} \sum_{jk} (f_k - f_j) \frac{\varphi_j(\mathbf{r})\varphi_j^*(\mathbf{r}')\varphi_k(\mathbf{r}')\varphi_k^*(\mathbf{r})}{\omega - (\epsilon_j - \epsilon_k) + i\eta}, \tag{2.59}$$

as a summation over all KS wavefunctions, φ_j and φ_k, whose occupation is given by f_j and f_k, with respect to their single-electron orbital energy differences $(\epsilon_j - \epsilon_k)$. The optical absorption spectrum can be obtained from the polarizability tensor,

$$\alpha_{\mu,\nu} = -\frac{1}{\pi} \text{Im}\langle \mu|\chi(\omega)|\nu\rangle, \tag{2.60}$$

by summing over the diagonal elements of the 3×3 ($\mu, \nu = x, y, z$) matrix of the imaginary part of χ, which is also called the spectral function of χ.

When one needs to take into account local crystal field effects, for example, for ions or metals, one should solve the Dyson equation which includes matrix inversion over reciprocal vectors $\mathbf{GG}'$. However, in our case, including local crystal field effects is not essential as we will show later. The greatest difficulty we have is the underestimation of the energy gap, which strongly affects the results of linear response calculations. However, we can usually match the experiment by simply performing a scissors operation, that is, applying a constant shift to the energies.

2.3.3 Linear Dielectric Response within the Random Phase Approximation

The RPA [204] is known as an orbital-dependent energy functional obtained by applying the time-dependent Hartree approximation to the density response function. The exact-exchange plus correlation RPA is attractive due to (1) the exact-exchange energy cancellation of the spurious self-interaction error present in the Hartree energy, (2) the non-local correlation energy including long-range van der Waals (vdW) interactions, and (3) the electronic screening, which makes RPA applicable to small-gap or metallic systems where finite-order many-body perturbation theories fail. The non-local dependence of the exact xc functional is especially important in calculations of optical properties of long conjugated molecular chains or non-metallic solids such as wide-band gap semiconductors. This becomes even more important when looking at junctions with non-covalent interactions. In these cases the adiabatic local density approximation (ALDA) tends to fail, since it is local both in space and time coordinates. [205,206]

On the one hand, RPA has the same shortcomings present in LDA and GGA to the xc functionals. These include their systematic underestimation of binding energies, their failure to describe stretched radicals, and their underestimation of reaction barrier heights. [204] On the other hand, RPA usually describes the mentioned physical properties better than GGA PBE. However, these discrepancies do not influence the results of the studies presented herein.

For our purposes RPA is particularly advantageous, since it combines accuracy and tractability with transferability across different chemical environments and dimensionalities, such as molecules, clusters, tubes, surfaces, and solids. Therefore, it is especially suitable for linear response calculations of extended systems.

To calculate the linear non-interacting density-density response function χ^0 for systems with periodic boundary conditions, as explained in section 2.2.2, we may perform a Fourier transform in space, going from a function of two positions $\mathbf{r}$ and $\mathbf{r}'$, to a function of two reciprocal lattice vectors $\mathbf{G}$ and $\mathbf{G}'$,

$$\chi^0_{\mathbf{GG}'}(\mathbf{q}, \omega) = \frac{1}{\Omega} \sum_{\mathbf{k}} \sum_{nm} \sum_{ss'} \frac{f_{ns'\mathbf{k}} - f_{ms\mathbf{k}+\mathbf{q}}}{\omega + \varepsilon_{ns'\mathbf{k}} - \varepsilon_{ms\mathbf{k}+\mathbf{q}} + i\eta} \langle \varphi_{ns'\mathbf{k}} | e^{-i(\mathbf{q}+\mathbf{G})\cdot\mathbf{r}} | \varphi_{ms\mathbf{k}+\mathbf{q}} \rangle \langle \varphi_{ns'\mathbf{k}} | e^{i(\mathbf{q}+\mathbf{G}')\cdot\mathbf{r}'} | \varphi_{ms\mathbf{k}+\mathbf{q}} \rangle, \quad (2.61)$$

where η is the electronic broadening, i.e., twice the inverse lifetime Γ of the transitions, Ω is the supercell volume, $f_{ns'\mathbf{k}}$ is the Fermi-Dirac occupation, $\varepsilon_{ns'\mathbf{k}}$ is the eigenenergy, and $\varphi_{ns'\mathbf{k}}$ is the KS wavefunction of the nth band in spin channel s' at $\mathbf{k}$-point $\mathbf{k}$.

To calculate the absorption spectrum we first need to derive the inverse dielectric function ε^{-1}, which relates the total electric field $\mathbf{E}$ in a material to the external electric field $\mathbf{E}_{ext}$,

$$\mathbf{E} = \varepsilon^{-1} \mathbf{E}_{ext}, \quad (2.62)$$

and can be approximated in the long-wavelength limit as

$$\varepsilon^{-1} = \frac{v_{tot}}{v_{ext}} = 1 + v_H \frac{n_{ind}}{v_{ext}}, \quad (2.63)$$

where v_{ext} is the potential that induces the change in charge density n_{ind}, whereas $v_{tot} = v^0 + v_{ext}$ is the total, "screened" potential generated by the total charge density $n(\mathbf{r}, t)$, and v_H is the Hartree potential or Coulomb kernel $4\pi/\|\mathbf{q}+\mathbf{G}\|^2$.

The dielectric matrix within linear dielectric response (LDR)-TDDFT-RPA [119,120,207] in reciprocal space is given by

$$\varepsilon^0_{\mathbf{GG}'}(\mathbf{q}, \omega) = \delta_{\mathbf{GG}'} - \frac{4\pi}{\|\mathbf{q}+\mathbf{G}\|^2} \chi^0_{\mathbf{GG}'}(\mathbf{q}, \omega). \quad (2.64)$$

The optical absorption spectrum is obtained from the imaginary part of the macroscopic dielectric function for $\mathbf{G} = \mathbf{G}' = 0$,

$$\text{Absorption} = \text{Im}\left[\varepsilon_M(\mathbf{q}, \omega)\right] = \lim_{q \to 0} \frac{1}{\varepsilon_{00}^{-1}(q, \omega)}. \tag{2.65}$$

Although $\mathbf{q}$ is close to zero, we cannot simply set $\mathbf{q} = 0$ because the Coulomb kernel $v_{\mathbf{G}}(\mathbf{q}) = 4\pi/\|\mathbf{q} + \mathbf{G}\|^2$ diverges at $\mathbf{q} = \mathbf{G} = 0$. Instead, taking the limit as $\mathbf{q} \to 0^+$, the matrix elements in equation 2.61 then reduce to

$$\langle \varphi_{ns'\mathbf{k}} | e^{-i(\mathbf{q}+\mathbf{G})\cdot\mathbf{r}} | \varphi_{ms\mathbf{k}+\mathbf{q}} \rangle = -i\mathbf{q} \cdot \frac{\langle \varphi_{ns'\mathbf{k}} | \nabla | \varphi_{ms\mathbf{k}+\mathbf{q}} \rangle}{\varepsilon_{ns'\mathbf{k}} - \varepsilon_{ms\mathbf{k}}}. \tag{2.66}$$

Slowly varying external fields cause rapid oscillations on the microscopic scale, which are called local field effectss (LFEs). Neglecting LFEs, parallel to $\mathbf{q}$, i.e., $\hat{\mathbf{e}}_{\mathbf{q}}$, $\varepsilon(\omega) = \varepsilon_{00}(\omega)$, is valid for materials that are also homogeneous on the microscopic scale and results in $\varepsilon_M = \varepsilon_{00}$.

Substituting equations 2.61 and 2.66 into equation 2.64, and suppressing $\mathbf{k}$-point dependence, we obtain the simplified form

$$\text{Im}[\varepsilon(\omega)] = \frac{4\pi\eta}{\Omega} \sum_{nm} \sum_{ss'} \frac{f_{ms} - f_{ns'}}{(\omega - \varepsilon_{ns'} + \varepsilon_{ms})^2 + \eta^2} \left(\frac{\hat{\mathbf{e}}_{\mathbf{q}} \cdot \langle \varphi_{ns'} | \nabla | \varphi_{ms} \rangle}{\varepsilon_{ns'} - \varepsilon_{ms}} \right)^2. \tag{2.67}$$

where $\hat{\mathbf{e}}_{\mathbf{q}}$ is a unit vector parallel to $\mathbf{q}$.

2.4   Conductance in the Quantum Regime

In the next sections we will discuss the description of currents, which allows us to compute the conductance, that is, the electronic transport properties, of nanosystems. Using the Landauer formula we can obtain the conductance of a perfectly transmitted current through a single-level channel. Quantum effects such as quantum tunnelling are important and significant in the nanoregime. Properly describing conductance at the nanoscale needs to take these effects into account. So it requires a full quantum description given by the Landauer-Bütticker formalism. A suitable method to calculate the Landauer-Bütticker conductance is the non-equilibrium Green's function (NEGF) method, which can be used to efficiently describe electron and hole propagation in multi-level systems. We will see how we can make use of the NEGF method to calculate the transmission probability of an excited electron passing from a polymer to a carbon nanotube. This shall reflect the photoinduced current in organic photovoltaics (OPVs), from which we can deduce the internal quantum efficiency (IQE) of the device.

Section 2.4.1 begins with a derivation of the Landauer formula, which describes the current through a single-level channel in terms of the rate electrons enter the channel and the difference in potential of each electron reservoir placed at the terminals of the channel. For perfectly transmitting spin degenerate channels the Landauer conductance reduces to the quantum of conductance, $G_0 = \frac{2e^2}{h}$. In section 2.4.2 we provide a basic introduction to two-point Green's functions, which can be used to calculate electron propagation between points in space and time. Finally, in section 2.4.3, we will show how we set up a 4-terminal Hamiltonian to calculate the Landauer-Bütticker conductance using the NEGF method. From this we obtain the transmission probability of an electron passing a more complex channel with four terminals, e.g., a polymer-carbon nanotube junction shown schematically in Figure 2.2.
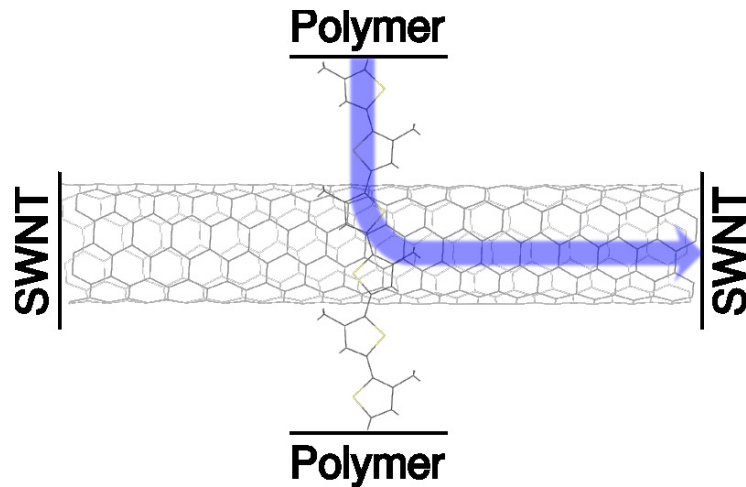

Figure 2.2: Schematic of a polymer/nanotube junction in a 4-terminal transport calculation resulting in the transmission probability of an excited electron to pass from the input lead (polymer) through the scattering region (heterojunction) to the output lead (nanotube) (blue arrow).

2.4.1 Landauer-Büttiker Conductance

Let us consider a nanotube acting as a channel for electronic transport, in the sense that electrons can move through a valence band from one end of the tube to the other. The part of the tube acting as a channel has to be sufficiently long that the contacts at the tube's ends are not interacting with each other, but only with the adjacent part of channel. We model the contacts as semi-infinite leads, which means that they are periodically repeated at the open ends of the tube. For simplicity, let us assume that only the lowest of the transverse eigenstates within the nanotube channel has an energy below the Fermi level, such that the channel becomes a one dimensional single-level channel. The leads are then ideal electron reservoirs, having no changes in potential, which are filled up to the chemical potential μ_{in} according to the Fermi-Dirac distribution $f(\epsilon)$,

$$f(\epsilon) = \frac{1}{1 + e^{(\epsilon - \epsilon_F)/k_B T}},$$

(2.68)

where $\epsilon_F = \mu + V$ is the Fermi energy, which in our case is the sum of the chemical potential μ and the applied bias V. In addition, we suppose that at zero Kelvin the potential of the input lead is slightly higher than the potential from the output lead μ_{out} due to additional electron filling. From this it follows that all states between μ_{in} and μ_{out} are fully occupied and electrons flow from the input lead through the channel to the output lead. The current due to the difference in potential $(\mu_{in} - \mu_{out})$ is given by

$$I = -(\mu_{in} - \mu_{out})e v_e \frac{\partial n}{\partial \mu},$$

(2.69)

where $\partial n/\partial \mu$ is the density of states including spin degeneracy, v_e is the velocity component along the tube at the Fermi surface, and e the electronic charge.[208] Since $\partial n/\partial \mu = 2/h v_e$, we have a net current flow of

$$I = -\frac{2e}{h}(\mu_{in} - \mu_{out})$$

(2.70)

We see that the current is the rate at which electrons jump into the channel multiplied by the difference in potential of the input and output leads. The zero-bias conductance of an ideal one dimensional conductor at the applied potential $V_{in} - V_{out} = \frac{\mu_{in} - \mu_{out}}{e}$ is then

$$G = \frac{I}{V_{in} - V_{out}} = \frac{2e^2}{h}.$$

(2.71)

Equation 2.71 is known as the quantum of conductance $G_0 = 2e^2/h$, which was derived by Rolf Landauer[209], and can be extended to n perfectly transmitting spin degenerate channels,

$$G = n\frac{2e^2}{h}.$$

(2.72)

If we have any kind of obstacle within the channel, which can be a localized barrier or a more extended and complex potential profile, the conductance G will be proportional to the transmitting probability $\overline{T}$ of that obstacle, such that G becomes

$$G = G_0\overline{T}.$$

(2.73)

Thus, describing the transmission from one lead to another can be done by relating the conductance to the transmission probability.[210]

Equation 2.73 can be generalized for channels that involve more than one transverse eigenstate with energy below the Fermi level. This extension is referred to as Landauer-Bütticker formalism[211], which includes a transmission matrix $\hat{t}\hat{t}^\dagger$ of the scattering obstacle with the transverse eigenstates of the channel as a basis,

$$G = G_0 \, \mathrm{Tr}[\hat{t}\hat{t}^\dagger].$$

(2.74)

In this way the transmitted wavefunctions relative to the incident wave can be evaluated.

We will see in section 2.4.3 that the Non-equilibrium Green's function method within the Landauer-Bütticker formalism offers an elegant way to calculate the transmission $\overline{T}$ of a polymer-carbon nanotube junction as shown in Fig. 2.2. First, we will discuss the basics of Green's functions in the next section.

2.4.2 Green's Functions

When we want to solve inhomogeneous differential equations of the form

$$\mathscr{L}_{\mathbf{r}}[u(\mathbf{r})] = f(\mathbf{r}),$$

(2.75)

where $\mathscr{L}_{\mathbf{r}}$ is a linear differential operator in $\mathbf{r}$ and $f(\mathbf{r})$ is a known function of $\mathbf{r}$, then we can express the solution $u(\mathbf{r})$ in terms of $f(\mathbf{r})$ and a two-point Green's function $\mathcal{G}(\mathbf{r}, \mathbf{r}')$ as

$$u(\mathbf{r}) = \int \mathcal{G}(\mathbf{r}, \mathbf{r}')f(\mathbf{r}')d\mathbf{r}'$$

(2.76)

where $\mathscr{L}_{\mathbf{r}}[\mathcal{G}(\mathbf{r}, \mathbf{r}')] \equiv \delta(\mathbf{r} - \mathbf{r}')$, so that

$$\mathscr{L}_{\mathbf{r}}[u(\mathbf{r})] = \mathscr{L}_{\mathbf{r}}\left[\int \mathcal{G}(\mathbf{r}, \mathbf{r}')f(\mathbf{r}')d\mathbf{r}'\right] = \int \mathscr{L}_{\mathbf{r}}\left[\mathcal{G}(\mathbf{r}, \mathbf{r}')\right]f(\mathbf{r}')d\mathbf{r}' = \int \delta(\mathbf{r} - \mathbf{r}')f(\mathbf{r}')d\mathbf{r}' = f(\mathbf{r}).$$

(2.77)

The Green's function $\mathcal{G}(\mathbf{r}, \mathbf{r}')$ reflects the action of $u(\mathbf{r})$ due to the application of $f(\mathbf{r})$.[212,213] A good example of such a problem is that of determining a potential $\Phi(\mathbf{r})$ generated by the charge density $n(\mathbf{r})$. Under the application of the Poisson equation and Coulomb's law $\nabla^2\Phi = n(\mathbf{r})$, and we obtain the solution for $\Phi(\mathbf{r})$,

$$\Phi(\mathbf{r}) = \int \frac{n(\mathbf{r}')}{|\mathbf{r} - \mathbf{r}'|}d\mathbf{r}'.$$

(2.78)

The Green's function $\mathcal{G}(\mathbf{r}, \mathbf{r}')$ to this equation is then the Coulomb kernel

$$\mathcal{G}(\mathbf{r}, \mathbf{r}') = \frac{1}{|\mathbf{r} - \mathbf{r}'|},$$

(2.79)

which is the integrand of the integral operator converting $n(\mathbf{r})$ in $\Phi(\mathbf{r})$,

$$\Phi(\mathbf{r}) = \int \mathcal{G}(\mathbf{r}, \mathbf{r}')n(\mathbf{r}')d\mathbf{r}'.$$

(2.80)

Similarly, we can use two-point one-particle Green's functions $\mathcal{G}(\mathbf{r}, t; \mathbf{r}', t')$ to describe the propagation of a particle between two points in space and time $(\mathbf{r}, t)$ and $(\mathbf{r}', t')$,

$$i\mathcal{G}(\mathbf{r}, t; \mathbf{r}', t') = \frac{\langle \Psi_0^N | \hat{T}[\hat{a}(\mathbf{r}, t), \hat{a}^\dagger(\mathbf{r}', t')] | \Psi_0^N \rangle}{\langle \Psi_0^N | \Psi_0^N \rangle},$$

(2.81)

where $\mathcal{G}(\mathbf{r}, t; \mathbf{r}', t')$ is constructed from the N-particle ground-state Ψ_0^N and the Heisenberg operators consisting of the annihilation operator $\hat{a} = e^{i\hat{H}t}\Psi(\mathbf{r})e^{-i\hat{H}t}$, and the creation operator $\hat{a}^\dagger$. $\hat{T}$ is the time-ordering operator, which returns the time-ordered product when applied to two operators

$$T(\hat{a}(\mathbf{r}, t), \hat{a}^\dagger(\mathbf{r}', t')) = \begin{cases} \hat{a}(\mathbf{r}, t)\hat{a}^\dagger(\mathbf{r}', t'), & \text{if } t < t' \\ \hat{a}^\dagger(\mathbf{r}', t')\hat{a}(\mathbf{r}, t), & \text{if } t > t' \end{cases}. \tag{2.82}$$

From the time-ordered Green's function it then follows that for $t < t'$ (lesser) an electron is created at $(\mathbf{r}', s', t')$, then propagated and annihilated at $(\mathbf{r}, s, t)$, and for $t > t'$ (greater) a hole is created at $(\mathbf{r}, s, t)$ and annihilated at $(\mathbf{r}', s', t')$.

The Green's function can be written in terms of 'retarded' and 'advanced' Green's functions, which are easier to analyze. The retarded $\mathcal{G}^r$ and advanced $\mathcal{G}^a$ Green's functions are defined by

$$\mathcal{G}^r(\mathbf{r}, \mathbf{r}'; t - t') = \Theta(t - t')\langle\Psi_0^N|\hat{a}(\mathbf{r}, t)\hat{a}^\dagger(\mathbf{r}', t')|\Psi_0^N\rangle, \tag{2.83}$$

$$\mathcal{G}^a(\mathbf{r}, \mathbf{r}'; t - t') = -i\Theta(t' - t)\langle\Psi_0^N|\hat{a}(\mathbf{r}, t)\hat{a}^\dagger(\mathbf{r}', t')|\Psi_0^N\rangle, \tag{2.84}$$

where Θ is the Heaviside step function,

$$\Theta = \begin{cases} 0, & \text{if } t < t' \\ 1, & \text{if } t > t' \end{cases}. \tag{2.85}$$

Equations 2.83 and 2.84 reflect a pair of linear response functions, where the operators $\hat{a}(\mathbf{r}, t)$ and $\hat{a}^\dagger(\mathbf{r}', t')$ give the expectation values in the presence and absence of the applied field, respectively. The retarded Green's function $\mathcal{G}^r$ describes the effect after the action and is therefore only nonzero for $t > t'$,

$$\mathcal{G}^r(\mathbf{r}, \mathbf{r}'; t - t') = \begin{cases} 0, & \text{if } t < t' \\ -ie^{i\hat{H}t}, & \text{if } t > t' \end{cases}. \tag{2.86}$$

In the equilibrium case retarded $\mathcal{G}^r$ and advanced $\mathcal{G}^a$ Green's functions are functions of the time difference $(t - t')$ only. The transform over time difference $\tau = t - t'$ of the retarded Green's function $\mathcal{G}^r(\epsilon)$ is

$$\mathcal{G}^r(\epsilon) = \lim_{\eta \to 0^+} \int_0^\infty \mathcal{G}^r(\tau)e^{i(\epsilon+i\eta)\tau/\hbar}d\tau, \tag{2.87}$$

where $\eta \to 0^+$ is a small positive complex part to which makes this integral well behaved in the upper limit, since equation 2.87 oscillates at long times. The Fourier-transformed retarded and advanced functions are complex conjugates of each other, so that $\mathcal{G}^r(\epsilon) = (\mathcal{G}^a(\epsilon))^\dagger$.

The physical meaning of the Green's functions is more illustrative in the form of the spectral function $A(\epsilon)$,

$$A(\epsilon) = i\left(\mathcal{G}^r(\epsilon) - \mathcal{G}^a(\epsilon)\right) = i\left(\mathcal{G}^>(\epsilon) - \mathcal{G}^<(\epsilon)\right), \tag{2.88}$$

where $\mathcal{G}^<$ and $\mathcal{G}^>$ are the kinetic lesser and greater Green's functions, respectively. Equation 2.88 is a valid expression in the wide-band limit ($t \to \infty$), at the energies $\epsilon - \epsilon_0 \ll 0$. There, $A(\epsilon)/2\pi$ can be interpreted as the available density of states. Hence, the density of states (DOS) can be obtained by tracing over the spectral function,

$$DOS = \text{Tr}[A(\epsilon)]. \tag{2.89}$$

In the next section we will see how we can make use of the Green's functions to describe the propagation of electrons (and holes) within the transport formalism referred to as the NEGF method.

2.4.3 Non-equilibrium Green's Function Method (NEGF)

NEGF[163,214–217] offer a way to predict electronic transport properties of a variety of systems such as superconducting nanostructures, resonant tunneling systems and junctions. The non-interacting one-electron description within NEGF is valid for coherent transport, where phase-coherence is preserved during the electron motion across the system. This means that there is no inelastic scattering due to electron-electron or electron-phonon collisions within the channel. That is the case for ballistic transport, where the mean free path between elastic collisions is longer than the dimension of the medium through which the electron travels. In this regime the momentum of the electron is constant and only limited by scattering with the boundaries of the sample. Experiments have shown that we find ballistic transport in carbon nanotubes, since the coherence length for nanotubes is quite long. Hence, NEGF is the perfect tool to study transport properties within carbon nanotube systems.

Before we can make use of the Landauer formula to calculate the transmission probabilities of an electron passing through a carbon nanotube, we have to include the full quantum description of the tube's KS orbitals. In the case of an isolated carbon nanotube, the Hamiltonian is written as

$$
\hat{H} =
\begin{pmatrix}
\ddots & \ddots & 0 & 0 & 0 & 0 & 0 & 0 & 0 \\
\ddots & \hat{H}^L_{in} & \hat{V}_{in} & 0 & 0 & 0 & 0 & 0 & 0 \\
0 & \hat{V}^\dagger_{in} & \hat{H}^L_{in} & \hat{V}_{inC} & 0 & 0 & 0 & 0 & 0 \\
0 & 0 & \hat{V}^\dagger_{inC} & \hat{H}_C & \hat{V}_{CC} & 0 & 0 & 0 & 0 \\
0 & 0 & 0 & \hat{V}^\dagger_{CC} & \hat{H}_C & \hat{V}_{CC} & 0 & 0 & 0 \\
0 & 0 & 0 & 0 & \hat{V}^\dagger_{CC} & \hat{H}_C & \hat{V}_{Cout} & 0 & 0 \\
0 & 0 & 0 & 0 & 0 & \hat{V}^\dagger_{Cout} & \hat{H}^L_{out} & \hat{V}_{out} & 0 \\
0 & 0 & 0 & 0 & 0 & 0 & \hat{V}^\dagger_{out} & \hat{H}^L_{out} & \ddots \\
0 & 0 & 0 & 0 & 0 & 0 & 0 & \ddots & \ddots
\end{pmatrix}
\tag{2.90}
$$

where $\hat{H}^L_{in}$ and $\hat{H}^L_{out}$ are Hamiltonians of the semi-infinite input and output leads and $\hat{H}_C$ are the Hamiltonians of the channel. When we construct the Hamiltonian matrix it is essential that the size of the leads and the channel is sufficient so that the ends of the channel or the leads are not interacting with each other. Only when the interactions are limited to two adjacent principle layers is the Hamiltonian matrix tridiagonal, so that the off-diagonal terms $\hat{V}_{in/outC}$, $\hat{V}_{CC}$ and $\hat{V}_{in/out}$ describe channel-to-lead, channel-to-channel and lead-to-lead coupling, respectively. As well, the Hamiltonian should be Hermitian, so we have

$$
\hat{V}_{Cin} = \hat{V}^\dagger_{inC}, \hat{V}_{CC} = \hat{V}^\dagger_{CC}, \hat{V}_{Cout} = \hat{V}^\dagger_{outC}.
\tag{2.91}
$$

However, we are not interested in the transmission probability of an electron passing through a carbon nanotube, since we know that ballistic transport occurs at 100%. Rather we would like to know the probability of an excited electron passing from a polymer across a junction to the carbon nanotube. These results can be linked to the internal efficiency of a donor–acceptor blend in OPV devices. For a polymer-carbon nanotube junction, we have to construct

a 4-terminal Hamiltonian,

$$
\hat{H} = \begin{pmatrix}
\hat{H}_{in}^{CNT} & 0 & \hat{V}_{in}^{CNT} & 0 & 0 \\
0 & \hat{H}_{in}^{P} & \hat{V}_{in}^{P} & 0 & 0 \\
\hat{V}_{in}^{CNT} & \hat{V}_{in}^{P} & \hat{H}_{C} & \hat{V}_{in}^{P} & \hat{V}_{Cout}^{CNT} \\
0 & 0 & \hat{V}_{in}^{P} & \hat{H}_{out}^{P} & 0 \\
0 & 0 & \hat{V}_{out}^{CNT} & 0 & \hat{H}_{out}^{CNT}
\end{pmatrix},
\tag{2.92}
$$

where $\hat{H}_{in/out}^{CNT}$, $\hat{H}_{in/out}^{P}$, and $\hat{H}_C$ are the Hamiltonians for the carbon nanotube input/output leads, the polymer input/output leads, and the channel, respectively. The channel includes the carbon nanotube junction. All the Hamiltonians can be extracted from independent periodic calculations, where the periodic boundary conditions are removed from the Hamiltonian. The coupling matrices $\hat{V}_{in/out}^{CNT}$ of the carbon nanotubes can be obtained from an isolated periodic carbon nanotube calculation and inserted identically for the input and output leads as well as for the complex conjugates. This is reasonable to do when the junction itself is far away from the lead-channel contact and we have only tube-tube interactions close to the lead-channel contact. A similar procedure can be employed to obtain the coupling matrices $\hat{V}_{in/out}^{P}$ of the polymers. We may similarly construct the 4-terminal overlap matrix,

$$
\hat{S} = \begin{pmatrix}
S_{in}^{CNT} & 0 & S_{in}^{CNT} & 0 & 0 \\
0 & S_{in}^{P} & S_{in}^{P} & 0 & 0 \\
S_{in}^{CNT} & S_{in}^{P} & S_{C} & S_{in}^{P} & S_{Cout}^{CNT} \\
0 & 0 & S_{in}^{P} & S_{out}^{P} & 0 \\
0 & 0 & S_{out}^{CNT} & 0 & S_{out}^{CNT}
\end{pmatrix}.
\tag{2.93}
$$

Since our focus is on what happens within the channel, all quantities of interest can be obtained just from the channel's retarded Green's function $\mathcal{G}_C^r$ given by

$$
\mathcal{G}_C^r = \left[(\epsilon + i\eta) S_C - \hat{H}_C - \sum_\alpha \Sigma_\alpha \right]^{-1},
\tag{2.94}
$$

where S_C is the overlap matrix, $\eta = 25$ meV is the electronic broadening at the room temperature, and Σ_α are the contact self-energies of the four leads. The concept of self-energy is used in many-body physics to describe electron-electron and electron-phonon interactions. Here, it is used to describe the effect of a semi-infinite contact, where only the coupling between adjacent layers of the reservoir ($\mu \times \nu$) and the channel ($m \times n$) are taken into account and the whole reservoirs themselves are neglected. The self-energy Σ_α of lead α is given by

$$
\Sigma_\alpha = \left[(\epsilon + i\eta) S_{C\alpha} - \hat{V}_{C\alpha} \right] \mathcal{G}_\alpha \left[(\epsilon + i\eta) S_{C\alpha}^\dagger - \hat{V}_{C\alpha}^\dagger \right],
\tag{2.95}
$$

where $\mathcal{G}_\alpha$ is the surface Green's function, a much smaller $\mu \times \nu$ matrix to invert to obtain the self-energies. Thus, the self-energy Σ_α is determined only by the energy $E = \epsilon + i\eta$, the coupling overlaps $S_{C\alpha}$ and Hamiltonians $\hat{V}_\alpha$ of the channel's end sites to the leads and the surface Green's function of the leads $\mathcal{G}_\alpha$,

$$
\mathcal{G}_\alpha = \left[(\epsilon + i\eta) S_\alpha - \hat{H}_\alpha^0 \right]^{-1}.
\tag{2.96}
$$

From this it follows that the contact self-energy is independent of the state of the nanosystem itself and just describes the influence of the leads. The coupling strength is described by the complex self-energy, where the real part gives

the energy shift of the level, and the imaginary part gives the broadening. The process of coupling to the channel inevitably broadens the level, which is described by the broadening, or coupling to the lead input/output, $\Gamma_{in/out}$,

$$\Gamma_{in/out} = i\left(\Sigma_{in/out} - \Sigma_{in/out}^{\dagger}\right). \tag{2.97}$$

In the wide-band limit the real part of the self-energy can be neglected, so that there is only level broadening. The self-energy of the lead then becomes

$$\Sigma_{in/out} = -i\frac{\Gamma_{in/out}}{2}. \tag{2.98}$$

Returning to the conductance G through a device, this is given in the Landauer formalism by

$$G = G_0 T(\epsilon), \tag{2.99}$$

where $T(\epsilon)$ is the transmission probability at energy E. This can be obtained using the NEGF formalism by including the channel's retarded $\mathcal{G}_C^r$ and advanced $\mathcal{G}_C^a$ Green's functions in addition to the broadenings of the leads Γ_α as

$$T(\epsilon) = \mathrm{Tr}\left(\mathcal{G}_C^a \Gamma_{in} \mathcal{G}_C^r \Gamma_{out}\right) = \mathrm{Tr}\left(\mathcal{G}_C \Gamma_{in} \mathcal{G}_C^{\dagger} \Gamma_{out}\right), \tag{2.100}$$

since $\mathcal{G}_C^r = (\mathcal{G}_C^a)^{\dagger}$. The transmission $T(\epsilon)$ gives the probability for an electron to pass through the available densities of states. The available density of states is given by the spectral function $A(\epsilon) = i(\mathcal{G}^r(\epsilon) - \mathcal{G}^a(\epsilon))$ weighted by the broadening with respect to the amount of coupling to the leads $\Gamma_{in/out}$. If we want to know the conductance G of a polymer-carbon nanotube junction, we choose the polymer to be the input lead and the nanotube to be the output lead to obtain the transmission of an electron passing from the polymer to the nanotube.

In summary, an NEGF calculation in GPAW follows the scheme depicted in Figure 2.3. This involves the following five steps:

(1) Generating the Hamiltonian and overlap matrices such as those provided in equations 2.92 and 2.93. These may be obtained from density functional theory calculations employing locally centered atomic orbitals or maximally localized Wannier orbitals, or based on tight-binding models.

(2) Calculating the influence of the leads on the scattering region by the surface Green's function and the self energy using equations 2.95 and 2.96. This step only requires the inversion of the smaller $\mu \times \nu$ surface Green's functions $\mathcal{G}_\alpha$.

(3) Calculating the retarded Green's function of the channel from equation 2.94. Since this step requires the inversion of the larger $m \times n$ channel Green's function $\mathcal{G}_C$, it is the bottle-neck of the NEGF calculation.

(4) Calculating the coupling to the input and output lead using equation 2.97.

(5) Calculating the transmission $T(E)$ with equation 2.100. Note that steps (2–5) must be repeated for each energy E to obtain the conductance as a function of energy $G = G_0 T(E)$.

Even though the NEGF method is rather sophisticated, it is only valid for coherent transport, as its self-consistent mean-field description does not include electron interactions and correlation effects. This is of importance for nanoscale devices with weak coupling to contacts such as the floating gate in flash memory devices. There, *Coulomb blockade* has been experimentally observed for systems where the charging energy U_0 exceeds the broadening
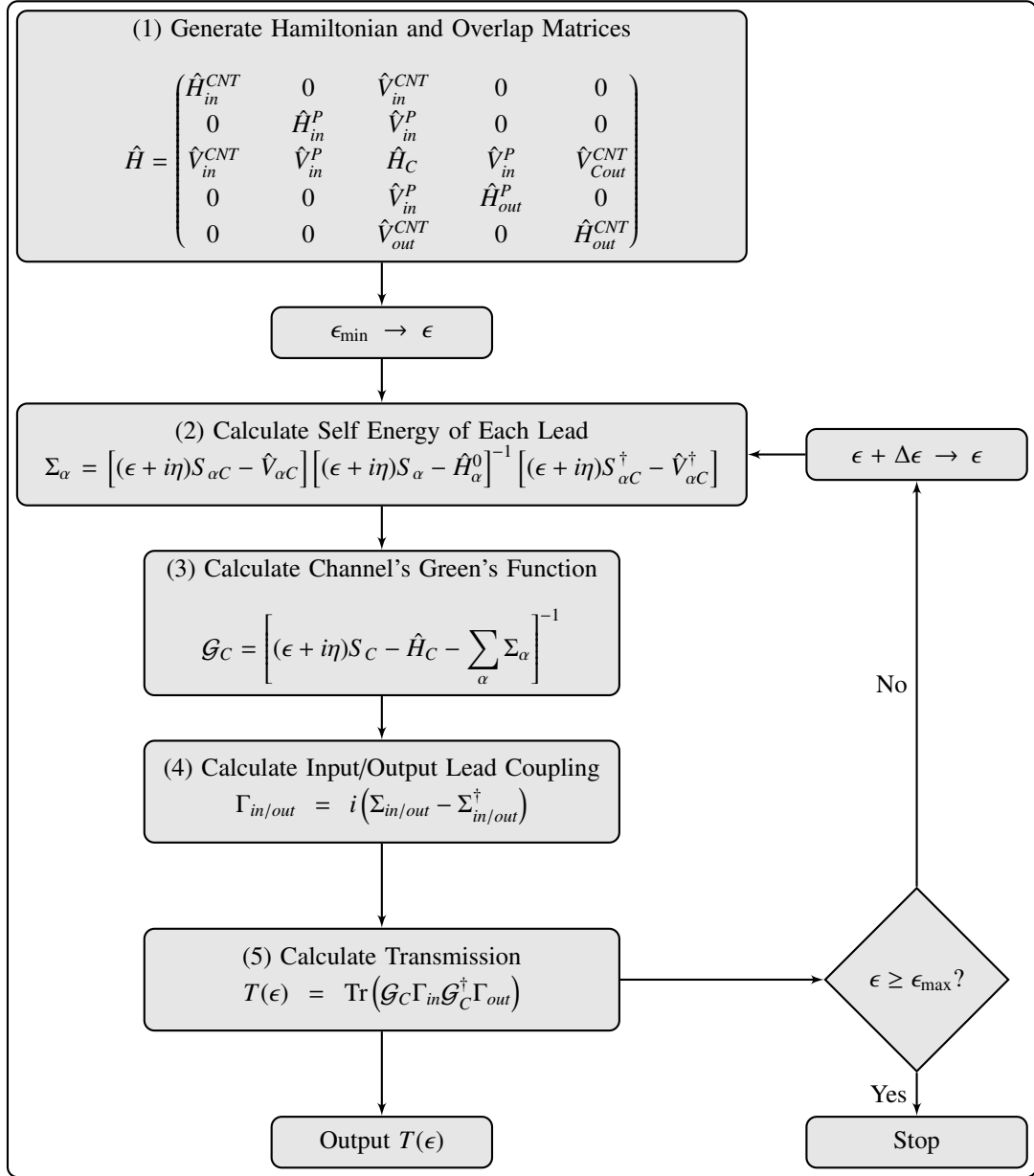
Figure 2.3: NEGF Scheme

$\gamma = \gamma_L + \gamma_R$ and $k_B T$ due to the connection to the surroundings. This leads to a split of the up and down spin density of states into two parts separated by the single-electron charging energy

$$U_0 \equiv e^2/C. \tag{2.101}$$

where C is the capacitance of the junction. In this case very little current flows when a small bias is applied, since there are few states between μ_L and μ_R. Nevertheless, the NEGF method can be extended to include the Coulomb

interaction with the help of the Anderson-Hubbard Hamiltonian $\hat{H}_{AH} = \frac{1}{2} \sum_{\alpha \neq \beta} U_{\alpha,\beta} \hat{n}_\alpha \hat{n}_\beta$ in the form of a density-density interaction to take into account *Coulomb blockade* amongst other phenomena.[218] For non-coherent transport it is possible to include the self-energy of the channel and the scattering region Γ_C.[219] As well, the NEGF method can be extended by the electron-vibron model to study the effect of vibrations on the transport properties.[218] This versatility makes the NEGF method an interesting playground for studying quantum charge transport in different regimes.

2.5 Calculation of Charge Distributions

For OPVs the charge transfer state within the donor–acceptor interface plays an essential role, since the degree of exciton splitting allows one to qualitatively compare the efficiency of donor–acceptor materials. A simple method to estimate charge transfer states is to calculate the amount of electrons transferred from the donor to the acceptor material or to localize the excitonic electron-hole pair within the heterojunction. Basically, all we need for this is to calculate some charge density distributions. Even in the case of the exciton, we can obtain the average electron and hole charge densities from ground-state calculations, either by extracting the two-point excitonic wavefunction for the electron-hole pair $\Psi_n(\mathbf{r}_e, \mathbf{r}_h)$ from a linear response calculation or by calculating the difference in electron densities between the triplet (excited) and singlet ground state. The triplet often gives a reasonable estimation of the singlet excited state and can easily be obtained by fixing a total magnetic moment μ in the ground-state calculation. After all, we have to keep in mind that charge distributions do not provide any direct information about the amount of exciton splitting, since we do not know the bound and dissociated electron and hole binding energies. Still, it allows us to estimate qualitatively the ability of the donor and the acceptor material to act as hole and electron acceptors, respectively.

In the following two sections we will illustrate methods for evaluating electron and hole densities (section 2.5.1) and calculating the charge transfer between molecules using the Bader charge analysis (section 2.5.2).

2.5.1 Electron Hole Densities

We can express the two-point excitonic wavefunction $\Psi_n(\mathbf{r}_e, \mathbf{r}_h)$ for the nth electron-hole pair in terms of the occupied, $\phi_i(\mathbf{r}_h)$, and unoccupied, $\phi_j(\mathbf{r}_e)$ KS wavefunctions as

$$\Psi_n(\mathbf{r}_e, \mathbf{r}_h) = \sum_{i=0}^{n_{occ}} \sum_{j=n_{occ}+1}^{n_{unocc}+n_{occ}} f_{nij} \phi_i(\mathbf{r}_h) \phi_j(\mathbf{r}_e), \tag{2.102}$$

where f_{nij} is the contribution of the $i \to j$ transition to the nth excitation, so that $\sum f_{nij}^2 = 1$, and $\mathbf{r}_e$ and $\mathbf{r}_h$ are the positions of the electron and hole, respectively.

The spatial distribution of a particular excitonic wavefunction $\Psi_n(\mathbf{r}_e, \mathbf{r}_h)$ may be quantified in terms of the average density of the electron $\rho_e(\mathbf{r}_e)$ and the average density of the hole $\rho_h(\mathbf{r}_h)$. The electron/hole average density is obtained by integrating the density of the excitonic wavefunction with respect to the hole/electron's position, i.e.

$$
\begin{aligned}
\rho_e(\mathbf{r}_e) &= \int d\mathbf{r}_h \Psi_n(\mathbf{r}_e, \mathbf{r}_h) \Psi_n^*(\mathbf{r}_e, \mathbf{r}_h) \\
&= \int d\mathbf{r}_h \sum_{i,i'} \sum_{j,j'} f_{nij} f_{ni'j'} \phi_i(\mathbf{r}_h) \phi_j(\mathbf{r}_e) \phi_{i'}^*(\mathbf{r}_h) \phi_{j'}^*(\mathbf{r}_e) \\
&= \sum_{i=0}^{n_{occ}} \sum_{j,j'=n_{occ}+1}^{n_{unocc}+n_{occ}} f_{nij} f_{nij'} \phi_j(\mathbf{r}_e) \phi_{j'}^*(\mathbf{r}_e) \approx \sum_{i=0}^{n_{occ}} \sum_{j=n_{occ}+1}^{n_{unocc}+n_{occ}} f_{nij}^2 \phi_j(\mathbf{r}_e) \phi_j^*(\mathbf{r}_e) \tag{2.103}
\end{aligned}
$$

$$
\rho_h(\mathbf{r}_h) = \sum_{i,i'=0}^{n_{occ}} \sum_{j=n_{occ}+1}^{n_{unocc}+n_{occ}} f_{nij} f_{ni'j} \phi_i(\mathbf{r}_h) \phi_{i'}^*(\mathbf{r}_h) \approx \sum_{i=0}^{n_{occ}} \sum_{j=n_{occ}+1}^{n_{unocc}+n_{occ}} f_{nij}^2 \phi_i(\mathbf{r}_h) \phi_i^*(\mathbf{r}_h). \tag{2.104}
$$

To compute the average electron/hole densities, we include transitions ranked by their weight f_{nij} until $\sum f_{nij}^2 > 0.95$.

2.5.2   Bader Charge Distribution

An intuitive way of partitioning charge between molecules and atoms is using the charge density minima between the atoms. In more detail, this can be done by determining the zero flux surfaces, that is, where the gradient of the charge density is zero along the surface normal. This is known as the Bader analysis. [220] We use the Bader analysis to define charge distributions after comparing the charge enclosed within the Bader volume with the total electronic charge of an atom or a whole molecule. This way we can compute where the partial charges are localized and if any charge transfer occurs between molecules.

Explicitly finding and representing the dividing surfaces is a challenging task. Therefore in GPAW [125], Henkelman et al. [221] implemented a fast and robust algorithm, that associates the Bader charge region with grid points instead. This is done by following a path of steepest ascent along the 26 possible directions, $\mathbf{r}_{\Delta i, \Delta j, \Delta k}$, towards adjacent grid points, using

$$\nabla n_{i,j,k} \cdot \mathbf{r}_{\Delta i, \Delta j, \Delta k} = \frac{\Delta n}{|\Delta \mathbf{r}|} = \frac{n_{i+\Delta i, j+\Delta j, k+\Delta k} - n_{i,j,k}}{|\mathbf{r}_{i+\Delta i, j+\Delta j, k+\Delta k} - \mathbf{r}_{i,j,k}|} \tag{2.105}$$

where the steepest ascent step selected, $\mathbf{r}_{\Delta i, \Delta j, \Delta k}$, is the one that maximizes the positive values of $\nabla n_{i,j,k}$ until the point $\mathbf{r}_{i,j,k}$ associated with a charge density maximum is found. [222] The total electronic charge of each Bader region is then given by summing over the grid points assigned to that region, that is, all points along paths of steepest ascent which terminate at the region's maximum. The computational time scales linearly with the number of grid points and analyzing a given charge density grid requires approximately 50 arithmetic operations per grid point.

However, for large systems with more than 100,000 grid points, this process can still prove quite demanding. Moreover, the above method typically associates a separate Bader region with each atom. To estimate the charge transfer between molecules, much of this partitioning between atoms proves unnecessary. For molecules which are well separated along the z-axis, one may partition the density into that associated with the lower and upper molecules using the projection of the density onto the z-axis, $n_k = \sum_{i,j} n_{i,j,k}$. The projected density is then partitioned by locating the point $k_{\min}$ which minimizes the projected density $\min_k n_k$ in between the molecules, with the charge associated with the lower and upper molecules being $\sum_{i,j,k<k_{\min}} n_{i,j,k}$ and $\sum_{i,j,k>k_{\min}} n_{i,j,k}$, respectively.

If the lower charge density region is further partitioned between two molecules separated along the y-axis, we may similarly partition the density in the lower region into a portion associated with the left and right molecules using the projection of the density onto the y-axis in the lower region, $n_j = \sum_{i,k<k_{\min}} n_{i,j,k}$. The projected density can again be partition by locating the point $j_{\min}$ which minimizes the projected density $\min_j n_j$ in between the molecules, with the charge associated with the left and right molecules being $\sum_{i,j<j_{\min}, k<k_{\min}} n_{i,j,k}$ and $n_{i,j>j_{\min}, k<k_{\min}} n_{i,j,k}$, respectively. Such methods are exceedingly efficient, as they employ a Newton's method to find a minimum, and only need to consider one coordinate direction at a time.

2.6 Single-Walled Carbon Nanotubes

There are different ways of folding a graphene sheet which each form distinctly different carbon nanotubes. The resulting symmetry of the honeycomb lattice within the nanotube, that is, the orientation and the number of six membered carbon rings along the circumference, gives rise to different bandstructures. In the next sections we will discuss how the symmetry influences the bandstructure and why there are metallic and semiconducting nanotubes.

In section 2.6.1 we will take a look at the different folding possibilities and the structure classification that can be made from it. Then we will discuss the tight binding band strucure of graphene and the resulting energy dispersion relation in section 2.6.2. Imposing periodic boundary conditions in the circumferential direction results in the band structure of single-walled carbon nanotubes, which we will show in section 2.6.3. Finally, we will discuss the resulting electronic properties from the different band structures.

2.6.1 Structure Classification and Symmetry

Single-walled carbon nanotubes (SWNTs) are cylindrical graphene sheets with a diameter of about 0.7 to 1.0 nm, with the majority of those observed having diameters smaller than 2 nm.[223,224] Due to their large length to diameter ratio of about 10^4 to 10^5, SWNTs are considered to be one dimensional nanostructures.

The orientation of the six-membered carbon ring within the lattice relative to the axis of the nanotube depends on which carbons of the graphene sheet are linked while folding. The different folding possibilities give rise to different lattice symmetries. The primary symmetries are classified into achiral (symmorphic) and chiral (non-symmorphic) nanotubes. The achiral nanotubes have identical mirror images and can be separated into two types named after the carbon sequence along the circumference of the nanotubes: zigzag (blue line) and armchair (red line) nanotubes shown in Figure 2.4. Chiral SWNTs have mirror images that cannot be superposed onto the original SWNT due to the spiral symmetry of the lattice. As a result, their circumferences have mixed patterns. All nanotubes terminate in so-called end caps, which resemble hemispheres of fullerenes.
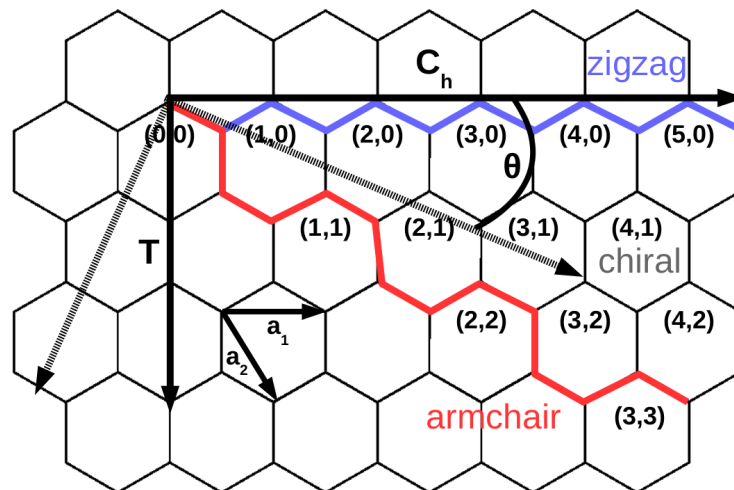

Figure 2.4: Rectangular slicing of graphene by chiral ($\mathbf{C}_h$) and translational ($\mathbf{T}$) vector to obtain zigzag $(n, 0)$ (blue), armchair (n, n) (red), or chiral (n, m) nanotubes depending on chiral angle θ.

Figure 2.4 shows the chiral vector $\mathbf{C}_h$, which points along the circumference of the tubes and is normal to the translational vector $\mathbf{T}$ along the nanotube axis. The symmetry of the nanotube is defined by the chiral angle θ between the chiral vector $\mathbf{C}_h$ and the real space lattice vector $\mathbf{a}_1$, which coincides with the zigzag line. The chiral angle θ is 0° for zigzag, 30° for armchair, and 0° < θ < 30° for chiral nanotubes. The chiral vector $\mathbf{C}_h$, expressed by the real space unit vectors $\mathbf{a}_1$ and $\mathbf{a}_2$ of the hexagonal lattice, is

$$\mathbf{C}_h = n\mathbf{a}_1 + m\mathbf{a}_2 \equiv (n, m), \tag{2.106}$$

where n and m are integers ($0 \leq m \leq n$). From this it follows that armchair nanotubes correspond to the case of $n = m$, that is $\mathbf{C}_h = (n, n)$ and zigzag to $m = 0$, or $\mathbf{C}_h = (n, 0)$. The chiral angle θ can be obtained from the inner product of $\mathbf{C}_h$ and $\mathbf{a}_1$,

$$\cos \theta = \frac{\mathbf{C}_h \cdot \mathbf{a}_1}{|\mathbf{C}_h||\mathbf{a}_1|} = \frac{2n + m}{2\sqrt{n^2 + m^2 + nm}}, \tag{2.107}$$

where the circumference is

$$C = |\mathbf{C}_h| = \sqrt{\mathbf{C}_h \cdot \mathbf{C}_h} = a\sqrt{n^2 + m^2 + nm}, \tag{2.108}$$

where the lattice constant $a \approx 1.42 \times \sqrt{3} \approx 2.49$ Å.

The translational vector $\mathbf{T}$ can also be expressed in terms of the basis vectors $\mathbf{a}_1$ and $\mathbf{a}_2$,

$$\mathbf{T} = t_1\mathbf{a}_1 + t_2\mathbf{a}_2 \equiv (t_1, t_2), \tag{2.109}$$

with $t_1 = \frac{2m+n}{d_R}$ and $t_2 = -\frac{2n+m}{d_R}$. d_R is the greatest common divisor (gcd) of $(2m + n)$ and $(2n + m)$, which can be related to d the gcd of n and m by

$$d_R = \begin{cases} d & \text{if } n - m \text{ is not a multiple of } 3d \\ 3d & \text{if } n - m \text{ is a multiple of } 3d \end{cases} \tag{2.110}$$

The length L of the translational vector $\mathbf{T}$ is then given by

$$L = |\mathbf{T}| = \sqrt{3}C/d_R. \tag{2.111}$$

From this it follows that the length L is greatly reduced when (n, m) have a common divisor or when $(n - m)$ is a multiple of $3d$. In fact, this leads to very short unit cells for symmetric nanotubes such as the (5,5) SWNT, where $d_R = 3d = 15$ and so $L = a$. This is an important point when performing periodic calculations on SWNTs, where L is the length of the repetition unit. For the case of (6,5) and (7,5) SWNTs, which have $L > 40$ Å, the computational effort is significantly increased due to the size of the calculation box and the number of atoms. However, nanotubes with short unit cells can still have significant numbers of atoms for large diameter nanotubes.

Perhaps at a first glance the lattice symmetries may not seem so critical. From other chiral molecules it is known that rarely do intramolecular or physical properties change with chirality, with the exception of the optical activity. However, in the case of carbon nanotubes, the carbon atom periodicity within the lattice has a huge impact on the band structure and therefore the electronic properties of SWNTs. The dependence of the band structure on the symmetry of SWNTs is explained in the next sections (2.6.2 and 2.6.3).

2.6.2 Tight Binding Band Structure of Graphene

To understand the band structure of SWNTs and its dependence on the lattice symmetry, we need to first take a look at the band structure of graphene.[225,226] The periodicity of crystals means that many levels of energy are possible for a given momentum and that some energies might not be available at any momentum. The collection of all possible energies and momenta is known as the band structure of a material.

The wavefunction *ansatz* is given by Bloch's Theorem

$$\psi_{\mathbf{k}} = \sum_{\mathbf{R}} e^{i\mathbf{k}\cdot\mathbf{R}} \phi(\mathbf{r} - \mathbf{R}) \tag{2.112}$$

where $\mathbf{R}$ are lattice vectors and ϕ is the atomic wavefunction of the p_z orbital. The unit cell of graphene consists of two inequivalent sublattices A and B, with the environments of the corresponding atoms being mirror images of one another. Since the unit cell includes the two orbitals, ϕ_1 and ϕ_2, the total function ϕ is a linear combination of ϕ_1 and ϕ_2

$$\phi(\mathbf{r}) = b_1 \phi_1(\mathbf{r}) + b_2 \phi_2(\mathbf{r}). \tag{2.113}$$

Since there are two unknown parameters b_1 and b_2 in equation 2.113, two equations are required to solve this eigenvalue problem. These are given by projecting $\psi_{\mathbf{k}}$ onto ϕ_1 and ϕ_2,

$$E_{\mathbf{k}} \langle \phi_j | \psi_{\mathbf{k}} \rangle = \langle \phi_j | U_j | \psi_{\mathbf{k}} \rangle \tag{2.114}$$

where U_j is only the potential of the Hamiltonian ($\hat{H} = K + U$), since the kinetic energy is set to $\epsilon_1 = \epsilon_2 = \epsilon_{2p_z} = 0$ for both electrons. When only on-site and nearest-neighbour overlaps are taken into account, $\langle \phi_j | \psi_{\mathbf{k}} \rangle$ is obtained from

$$\langle \phi_j | \psi_{\mathbf{k}} \rangle = b_j + b_i \gamma_0 (1 + e^{-i\mathbf{k}\cdot\mathbf{a}_1} + e^{-i\mathbf{k}\cdot\mathbf{a}_2}) \tag{2.115}$$

and $\langle \phi_j | U_j | \psi_{\mathbf{k}} \rangle$ from

$$\langle \phi_j | U_j | \psi_{\mathbf{k}} \rangle = b_i \gamma_1 (1 + e^{-i\mathbf{k}\cdot\mathbf{a}_1} + e^{-i\mathbf{k}\cdot\mathbf{a}_2}) \tag{2.116}$$

where $\gamma_0 = \langle \phi_j | \phi_i \rangle$ and $\gamma_1 = \langle \phi_j | U_j | \phi_i \rangle$ are the overlap integrals, which are both considered to be real and the change of indices should not matter due to symmetry. In this way the eigenvalue problem can be formulated as

$$\begin{pmatrix} E_{\mathbf{k}} & \alpha (\gamma_0 E_{\mathbf{k}} - \gamma_1) \\ \alpha^\dagger (\gamma_0 E_{\mathbf{k}} - \gamma_1) & E_{\mathbf{k}} \end{pmatrix} \begin{pmatrix} b_1 \\ b_2 \end{pmatrix} = \begin{pmatrix} 0 \\ 0 \end{pmatrix}, \tag{2.117}$$

where $\alpha = 1 + e^{-i\mathbf{k}\cdot\mathbf{a}_1} + e^{-i\mathbf{k}\cdot\mathbf{a}_2}$. Making use of the fact that γ_0 is small, the approximate dispersion relation is[227]

$$E_{\mathbf{k}} \approx \pm\gamma_1 |\alpha(\mathbf{k})| = \pm\gamma_1 \sqrt{3 + 2\cos(\mathbf{k}\cdot\mathbf{a}_1) + 2\cos(\mathbf{k}\cdot\mathbf{a}_2) + 2\cos(\mathbf{k}\cdot(\mathbf{a}_2 - \mathbf{a}_1))}. \tag{2.118}$$

This equation can be reformulated expressing $\mathbf{k}$ in its (x, y) components[226,228],

$$E_{(k_x,k_y)} = \pm\gamma_1 \sqrt{1 + 4\cos\left(\frac{\sqrt{3}k_x a}{2}\right)\cos\left(\frac{k_y a}{2}\right) + 4\cos^2\left(\frac{k_y a}{2}\right)}, \tag{2.119}$$

where $a = \sqrt{3}a_0$ is the lattice constant. Switching from real space vectors to $\mathbf{k}$-space results in expressing the energy dispersion in reciprocal space.

For graphene, the reciprocal lattice points (grey) also from a hexagonal lattice as shown in Figure 2.5. It is constructed from the reciprocal lattice vectors $\mathbf{b}_1$ and $\mathbf{b}_2$, which are defined to be normal to the real space lattice
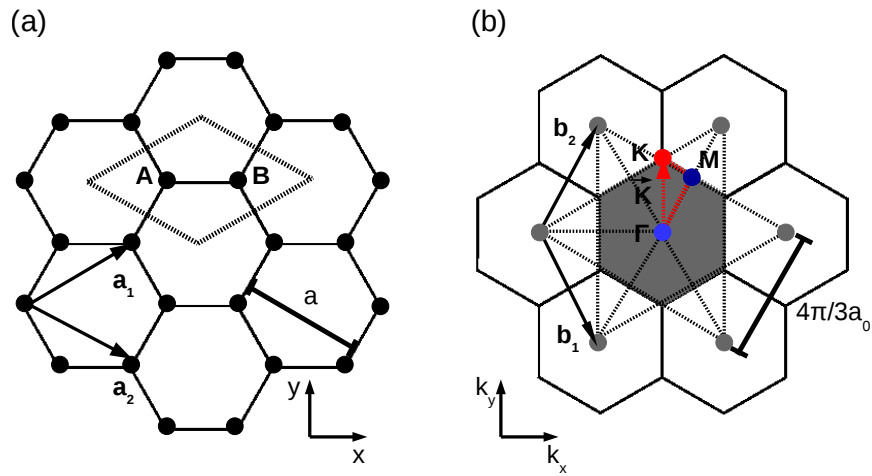
(a)

(b)

Figure 2.5: (a) Real-space lattice of graphene with unit cell in dashed lines and (b) reciprocal lattice points (grey) with first Brillouin zone in grey.
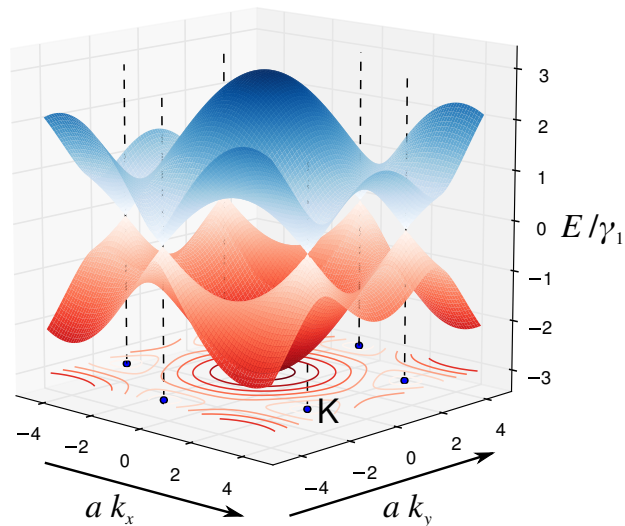

Figure 2.6: Energy dispersion relation of graphene with bonding states at $E_{\mathbf{k}} < 0$ (red) and anti-bonding states $E_{\mathbf{k}} > 0$ (blue).

vectors $\mathbf{a}_1$ and $\mathbf{a}_2$. The first Brillouin zone (FBZ) is then obtained by dividing all connecting lines between reciprocal points in half by normal intersections. The FBZ consists of high symmetry points, the Γ-point in the center, the K-points at the corners, and the M-points at the midways of the intersections.

Plotting the dispersion relation such as in Figure 2.6 yields bands with $E_{\mathbf{k}} < 0$ for the antisymmetric wavefunctions, which are the bonding states, and bands with $E_{\mathbf{k}} > 0$ for the symmetric wavefunctions, which are the antibonding states. As well, it is shown that $E_{\mathbf{k}}$ is zero for $\mathbf{k} = \frac{4\pi}{3\sqrt{3}a_0}\hat{\mathbf{e}}_y$, which is exactly at the corners, or K-points, of the Brillouin zone. There, the two states are degenerated and the DOS of the bonding state goes to zero. This point is called Dirac point, and the energy dispersion close to the K-point is called the Dirac cone. Since the DOS

is filled up to the Dirac point and empty above, the Fermi level is located exactly at the Dirac point. This means 2D graphite is a semimetal. It will exhibit some conduction at finite temperatures, since the carriers are easily excited into the conduction band. However, it does not conduct like a metal, since only a few electrons can pass the narrow Dirac point.

The existence of a zero gap at the K-points comes from a symmetry requirement that the two carbon sites A and B in the hexagonal lattice be equivalent to each other. If they are not equivalent, as is the case for hexagonal boron-nitrite, the differences in on-site energies ϵ_{2p_z} will open a band gap. In the next section (2.6.3) we will discuss how changes in symmetry and quantization along the circumference of the SWNT will influence its band structure and the band gap.

2.6.3 Band Structure of Single-Walled Carbon Nanotubes

In comparison to the unit cell of graphene, the unit cell of a carbon nanotube is given by the rectangle generated by the chiral vector $\mathbf{C}_h$ and the translational vector $\mathbf{T}$ as explained in section 2.6.1.[223,224] The unit cell includes $2N$ carbon atoms, and therefore N bonding and N anti-bonding π bands, where N is the number of hexagons.

The nanotube's reciprocal lattice vectors $\mathbf{B}_1$ and $\mathbf{B}_2$ are obtained from the relations

$$\begin{aligned}
\mathbf{C}_h \cdot \mathbf{B}_1 &= 2\pi, \quad \mathbf{T} \cdot \mathbf{B}_1 = 0, \\
\mathbf{C}_h \cdot \mathbf{B}_2 &= 0, \quad \mathbf{T} \cdot \mathbf{B}_2 = 2\pi.
\end{aligned} \tag{2.120}$$

In terms of the reciprocal lattice vectors $\mathbf{b}_1$ and $\mathbf{b}_2$ of graphene, $\mathbf{B}_1$ and $\mathbf{B}_2$ can be expressed as

$$\mathbf{B}_1 = \frac{1}{N}(-t_2\mathbf{b}_1 + t_1\mathbf{b}_2), \quad \mathbf{B}_2 = \frac{1}{N}(-m\mathbf{b}_1 + n\mathbf{b}_2). \tag{2.121}$$

The electronic structure of a single-walled carbon nanotube can be simply obtained from that of graphene by using periodic boundary conditions in the circumferential direction. This implies that the wave vector associated with the $\mathbf{C}_h$ direction becomes quantized. Note that we consider the wave vector associated with the translational
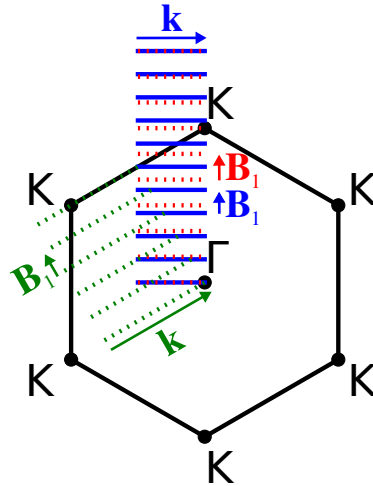

Figure 2.7: Hexagonal Brillouin zone of graphene with the first Brillouin zones of the (9,0) SWNT (red dashed), (10,0) SWNT (blue) and (5,5) SWNT (green dashed) carbon nanotubes.
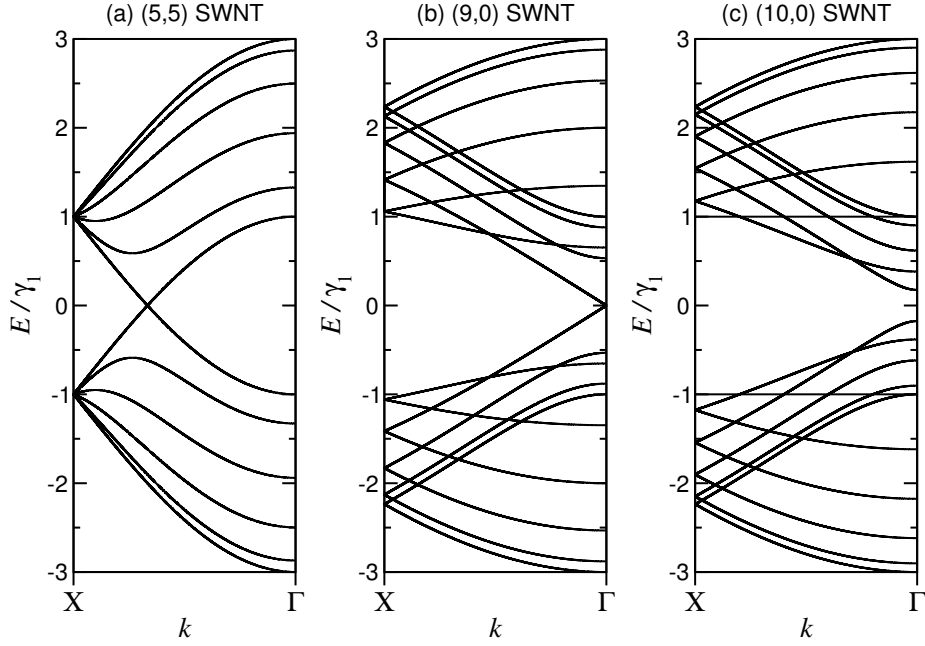
Figure 2.8: One dimensional energy dispersion relations for (a) armchair (5,5) (b) zigzag (9,0), and zigzag (10,0) carbon nanotubes. The X-point for armchair and zigzag carbon nanotubes corresponds to $k = \pm\frac{\pi}{a}$ and $k = \pm\frac{\pi}{\sqrt{3}a}$, respectively.

vector $\mathbf{T}$ to be continuous due to the macroscopic length of SWNTs. For short SWNTs, the wave vector associated with $\mathbf{T}$ would be discrete. The quantization of the wave vector associated with $\mathbf{C}$ gives rise to parallel line segments along the $\mathbf{B}_1$ direction, as depicted in Figure 2.7. This irreducible set of equidistant cutting-lines is the SWNT's first Brillouin zone. Hence, the first Brillouin zone of a nanotube is a subset of the unfolded graphene Brillouin zone.

As shown before, the indices (n, m) uniquely specify the geometry of a nanotube, such as the diameter, the chiral angle, the length of the unit cell along the tube axis, and the number of graphene unit cells inside the SWNT unit cell. This implies that the spacing, the length, the orientation, and the number of the cutting lines depends on the indices (n, m). The spacing between cutting lines is inversely proportional to the SWNT circumference $(2\pi/C)$, the length of the lines is inversely proportional to the length of the SWNT unit cell along the tube axis $(2\pi/L)$, and the orientation of the cutting lines depends on the SWNT chiral angle θ. Since there are N graphene unit cells inside the SWNT unit cell, there are N wave vectors $\mu\mathbf{B}_1(\mu = 0, \cdots, N-1)$ giving rise to N discrete $\mathbf{k}$ vectors. This means any two wave vectors which differ by $N\mathbf{B}_1$ are equivalent.

When a cutting line crosses graphene's Brillouin zone's K-points, the SWNT is metallic. This is the case for (9,0) and (5,5) as shown in Figure 2.7. Such a crossing occurs when $\frac{2n+m}{3}$ is an integer, which means the K-point can be folded onto the Γ-point. This means that for metallic nanotubes the condition $n - m \equiv 0 \pmod 3$ is also valid. When $n - m \equiv 1 \pmod 3$, the SWNT is semiconducting such as the (10,0) SWNT, as shown in Figure 2.7. It has to be mentioned that the effects of curvature can be reasonably neglected for large diameter nanotubes. However, small diameter nanotubes can have metallic features even when $n - m \neq 0 \pmod 3$, such as for the (5,0) SWNT.

The energy dispersion relations $E_{(k_x,k_y)}$ are obtained by applying appropriate periodic boundary conditions along
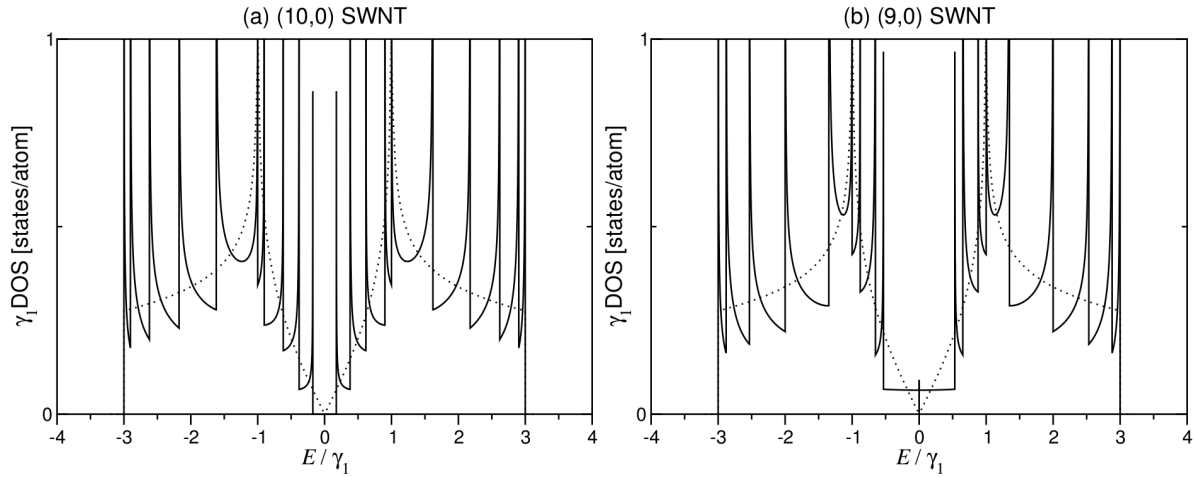
Figure 2.9: DOS of (a) semiconducting $(10, 0)$ SWNT with band gap and (b) metallic $(9, 0)$ SWNT with constant non-zero DOS at Fermi level ($E = 0$), both superposed on DOS of graphene (dotted lines).

the direction of $\mathbf{C}_h$. This is done by substituting k_x and/or k_y by the small number of allowed wave vectors $k_{\alpha,q}$ ($\alpha = x, y; q = 1, \cdots, 2n$), which are $n\sqrt{3}k_{x,q}a = 2\pi q$ for the armchair nanotube and $nk_{y,q}a = 2\pi q$ for the zigzag nanotube. For the (n, n) armchair nanotube, this boundary conditions invoke a crossing of the valence and conduction bands at two thirds of the distance from Γ to the zone boundary at X, as shown in Figure 2.8 (a). For the case of metallic zigzag nanotubes a crossing occurs at the Γ-point (Figure 2.8 (b)), whereas for semiconducting zigzag nanotubes there is a band gap, as shown in Figure 2.8 (c).

A clear picture of the differences between SWNTs and graphene is given by comparing their density of states, as provided in Figure 2.9. Of particular interest is the DOS near the Fermi level E_F located at $E = 0$. On the one hand, for a metal nanotube the DOS is non-zero. Moreover, the DOS per unit length along the nanotube axis is constant. This is the case for all metal nanotubes, independent of their diameter and chirality. On the other hand, semiconducting nanotubes have a zero DOS at the Fermi level and a band gap. It was shown[229] that the size of the energy gap E_g depends upon the reciprocal nanotube diameter d_t

$$E_g = \frac{|\gamma_1|a_0}{d_t}, \tag{2.122}$$

and is independent of the chiral angle of the semiconducting nanotube. Another difference can be found in the fluctuation of the DOS. At certain energies, where the dispersion relation has an extremum, the DOS diverges. These Van Hove singularities give rise to certain energy levels and occur more often in 1D SWNTs than in 2D graphene.

Chapter 3

Results & Discussion

3.1   Modelling Polymers from Oligomers*

Sorting small band gap nanotubes with photoactive polymers would be a straightforward approach to the production of polymer-single-walled carbon nanotube (SWNT) thin films for organic photovoltaics (OPVs). Still, the polymer–SWNT interface is not well understood. To be able to perform computational studies on such hybrid systems, we must first find an oligomer with the minimal size of a polymer building block that reproduces the properties of interest of the full polymer. Only in so doing can we hope to reduce the computational costs sufficiently to subsequently model complex hybrid systems.

In this section we show that the electronic properties of PFO-BPy, such as optical absorption and electron hole densities of the polymer, are already well described by the monomer unit of Py-PFO-Py, shown schematically in Figure 3.1. This is accomplished by performing time-dependent density functional theory (TDDFT) calculations of the optical absorption spectra for isolated monomers, dimers, and trimers of Py-PFO-Py and PFO-BPy, and the periodically repeated polymer. Further, we compare the calculated spectra for diethyl ($R_1 = CH_2CH_3$) and dioctyl ($R_1 = (CH_2)_7CH_3$) side chains. These results suggest one may accurately model a complex polymer-SWNT hybrid heterojunction using the simplified monomer–SWNT hybrid system including Py-PFO-Py depicted in Figure 3.2.

3.1.1   Computational Details

All density functional theory (DFT) calculations were performed with the real-space projector augmented wave (PAW) method code GPAW [125,126]. We used a grid spacing of 0.2 Å for representing the density and the wavefunctions and the Perdew-Burke-Ernzerhof xc functional (PBE) exchange and correlation (xc)-functional [184]. Structural minimization was performed within the atomic simulation environment (ASE) [230], until a maximum force below 0.05 electronvolt (eV)/Å was obtained.

Non-periodic boundary conditions were applied for the isolated polymer units, employing more than 5 Å of vacuum to the cell boundary, where both the electronic density and wavefunctions are set to zero. To model an infinitely long polymer, we repeated one Py-PFO-Py unit periodically along the polymer's length, and obtained a
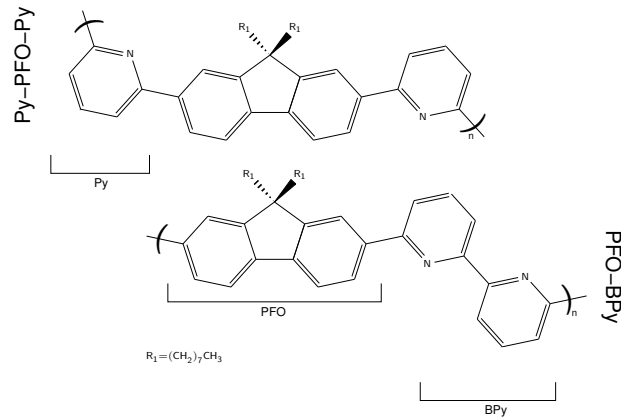

Figure 3.1: Chemical structure of a Py-PFO-Py unit (upper panel) and the PFO-BPy unit (lower panel) of the PFO-BPy polymer.
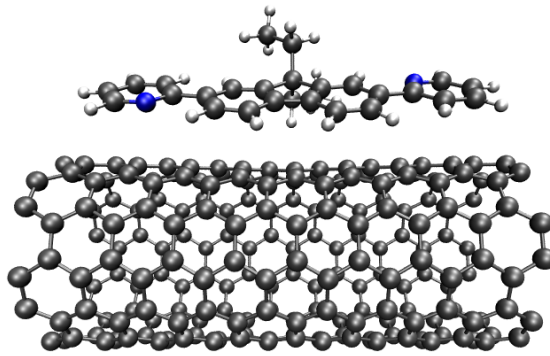
Figure 3.2: Schematic of Py-PFO-Py monomer adsorbed on a SWNT.

converged separation between repeated Py-PFO-Py units of $L = 14.866$ Å.

The optical absorption spectra were calculated from the transition dipole matrix elements, which were obtained with linear response TDDFT[231]. For these calculations we increased the number of unoccupied bands included n_{unocc} to twice the number of occupied levels n_{occ}. We find this resulted in a converged optical spectra up to 6 eV.

To compare directly with the full polymer, we have also performed calculations for the periodically repeated monomer unit. In this case, the optical absorption has been calculated from the imaginary part of the macroscopic dielectric response function $\varepsilon_m(\omega)$ obtained from linear dielectric response (LDR) TDDFT within the random phase approximation (RPA)), as recently implemented within GPAW[119,120]. The macroscopic dielectric function is calculated including local field effectss (LFEs) by solving Dyson's equation in terms of the non-interacting density-density response function. To ensure the 1D Coulomb kernel retains all interactions within the unit cell, while excluding spurious interactions between periodic images, we have doubled the unit cell dimensions in the non-periodic directions, "padding" the Kohn-Sham (KS) wavefunctions with zeros, and employed a Coulomb cutoff R equal to the original unit cell dimensions in the non-periodic directions.[232]
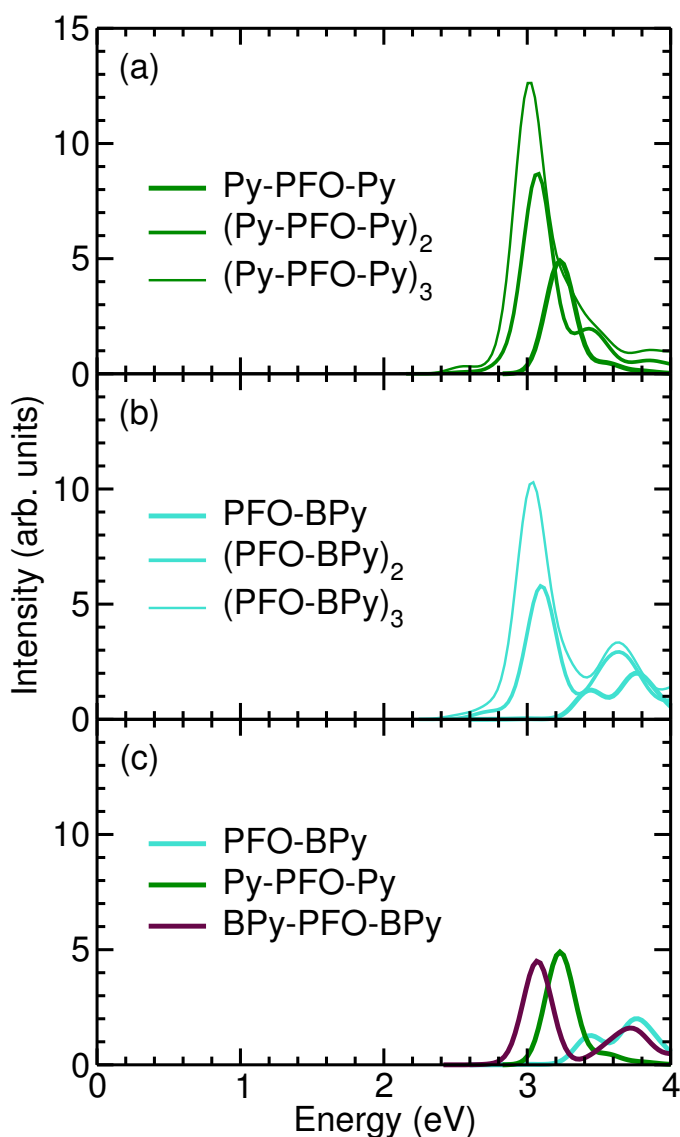
Figure 3.3: TDDFT absorption spectra of the (a) monomer Py-PFO-Py, dimer (Py-PFO-Py)$_2$, and trimer (Py-PFO-Py)$_3$, (b) monomer (PFO-BPy), dimer (PFO-BPy)$_2$, and trimer (PFO-BPy)$_3$, and (c) monomers of PFO-BPy and Py-PFO-Py and the extended monomer BPy-PFO-BPy.

3.1.2 Monomer, Dimer, Trimer, and Polymer Absorption Spectra

The TDDFT spectra for the monomer, dimer, and trimer of the PFO-BPy polymer are shown in Figure 3.3, based on the (a) Py-PFO-Py and (b) PFO-BPy units. In both cases there is no significant red shift from the dimer to the trimer (~ 0.05 eV). The absorption peak of the low energy transition band of the monomer PFO-BPy is blue shifted up to the absorption of the bipyridine part. In comparison to the peak maximum of the monomer, Py-PFO-Py is found only 0.15 eV higher in energy than its corresponding dimer. This is in contrast to PFO-BPy, which is more

Figure 3.4: LDR-TDDFT-RPA absorption spectra, $\Im[\varepsilon_m(\omega)]$, for the monomer Py-PFO-Py, dimer (Py-PFO-Py)$_2$, and repeated polymer (Py-PFO-Py)$_\infty$.

than 0.2 eV higher in energy. Perhaps more importantly, the relative intensities of the two lowest energy peaks differ qualitatively between the PFO-BPy monomer and either the dimer or trimer.

In Figure 3.3(c) we compare the spectra of the two monomers with the spectrum of the extended monomer BPy-PFO-BPy. The BPy-PFO-BPy monomer has on each side an additional terminating pyridine forming bipyridine. With the inclusion of these terminating pyridine units in BPy-PFO-BPy, the peak maximum of the spectrum is found to be identical to the dimer (Py-PFO-Py)$_2$. This suggests there is only a rather weak π-conjugation between subunits of the polymer.
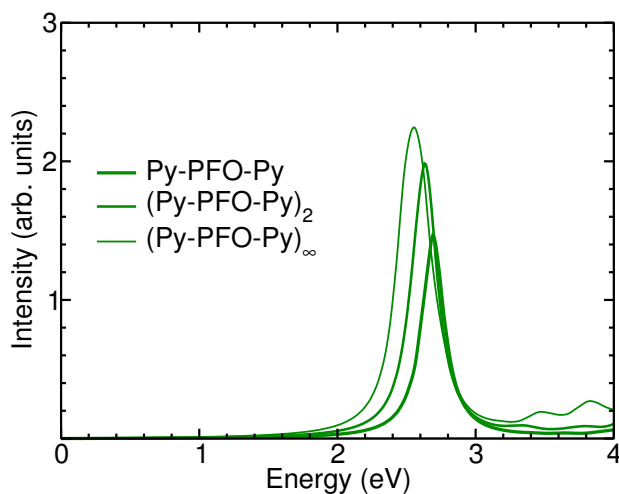
The LDR-TDDFT-RPA absorption spectra are shown in Figure 3.4 for the periodically repeated polymer (PFO-BPy)$_\infty$, dimer (PFO-BPy)$_2$ and monomer (PFO-BPy). Although, all spectra are red shifted up to 0.5 eV compared to linear response TDDFT shown in Fig 3.3(a), we still find the oligomer spectra quickly converged to that of an infinitely long polymer. Furthermore, the monomer and the dimer peak positions differ by only 0.1 eV, which is even less than with linear response TDDFT, as shown in Figure 3.3(a). Moreover, the difference between the dimer and the infinite chain is around 0.08 eV.

Within linear response TDDFT, 90% of the brightest excitation is a highest occupied molecular orbital (HOMO)-lowest unoccupied molecular orbital (LUMO) transition. Given a calculated HOMO-LUMO band gap of 2.6 eV for the monomer, LDR-TDDFT-RPA reproduces a fully HOMO-LUMO transition, whereas linear response TDDFT includes more higher lying terms. This is due to tha fact that screening included in LDR-TDDFT-RPA suppresses the linear response (LR)-TDDFT higher lying terms.

3.1.3 Electron and Hole Densities

To understand the spatial distribution of the exciton, we next consider the averaged densities of the electron and hole within the most intense low energy peak in the spectra shown in Figure 3.3(c). In Figure 3.5 the isosurfaces of the average density of the hole (red) and the average density of the electron (blue) for the most intense excitonic transition of the monomers PFO-BPy (a), Py-PFO-Py (b), and the extended monomer BPy-PFO-BPy (c) are plotted.

(a) PFO–BPy

(b) Py–PFO–Py

(c) BPy–PFO–BPy

Figure 3.5: Isosurfaces of the average electron (blue) and hole (red) densities, $\rho_e(\mathbf{r}_e)$ and $\rho_h(\mathbf{r}_h)$, of the exciton belonging to the most intense transition of the low energy absorbance band, i.e. the peak maximum, for (a) PFO-BPy, (b) Py-PFO-Py, and (c) BPy-PFO-BPy.

For all the monomers, the hole is mainly located on the 9,9-dioctylfluorenyl-2,7-diyl (PFO) with small weights on the neighbouring pyridines. For the monomer PFO-BPy, the density of the electron is almost only located on the bipyridine, whereas for Py-PFO-Py and BPy-PFO-BPy it is distributed over the same space as the hole densities within the antibonding π-system. More importantly, we clearly see a localization of the electron-hole pair on the central Py-PFO-Py portion of the BPy-PFO-BPy unit, which has only a minor weight of the electron on the additional terminating pyridines in BPy-PFO-BPy. This suggests that the PFO-BPy polymer lacks significant π conjugation between Py-PFO-Py units.

The dimer (Py-PFO-Py)$_2$, and the trimer (Py-PFO-Py)$_3$ in Figure 3.6 show the same excitonic structure as the latter oligomers repeating with every attached unit. In the dimer, there is some weight of the electron densities on the pyridines, whereas for the trimer this is almost completely lost. The exciton and the absorption band of the polymer seem to be composed of a sum of repeating excitons located on the Py-PFO-Py units. For the dimer (PFO-BPy)$_2$ and the trimer (PFO-BPy)$_3$, it is found that there are fewer excitons. Since for PFO-BPy units there is no stabilizing pyridine next to the PFO on one end, there is no exciton on this side contributing to that transition. Nevertheless, there is almost no blue shift of these larger PFO-BPy oligomers compared to the Py-PFO-Py oligomers, as shown in Figure 3.3(a) and (b).
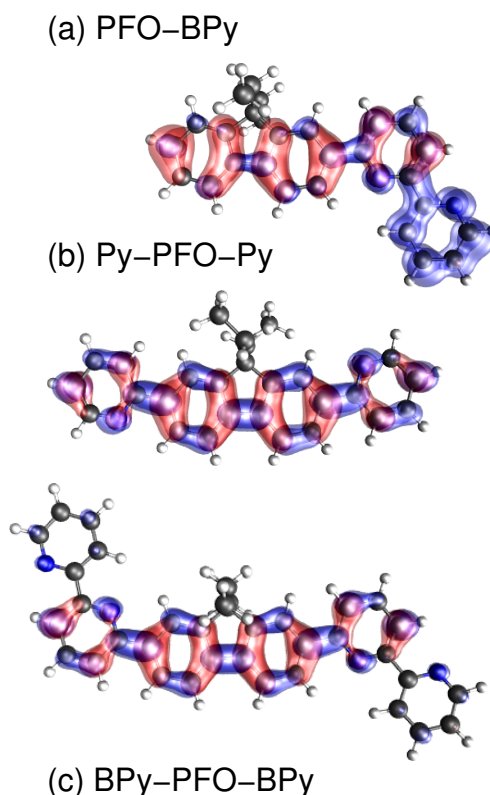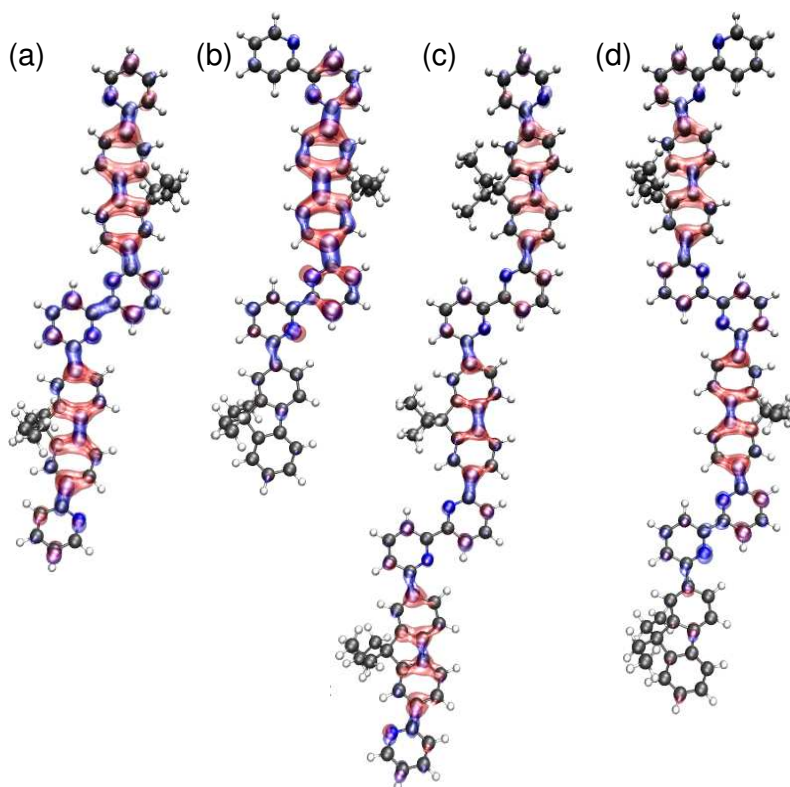
Figure 3.6: Isosurfaces of the average electron (blue) and hole (red) densities, $\rho_e(\mathbf{r}_e)$ and $\rho_h(\mathbf{r}_h)$, of the exciton belonging to the most intense transition of the low energy absorbance band, i.e. the peak maximum, for (a) (Py-PFO-Py)$_2$, (b) (PFO-BPy)$_2$, (c) (Py-PFO-Py)$_3$, and (d) (PFO-BPy)$_3$.

3.1.4   Twisting and Side Chain Independence of the Absorption Spectra

In Figure 3.7 we compare the absorption spectra for the dimer (Py-PFO-Py)$_2$ and monomer Py-PFO-Py spectra with that of a (Py-PFO-Py)$_2$ dimer which has been twisted to break its π-conjugation. Specifically, we rotated the Py-Py bond of the dimer (Py-PFO-Py)$_2$, twisting both monomer units 90 degrees to each other ($\theta = 90°$). In this way, one Py-PFO-Py unit is perpendicular to the other. The resulting spectra of the dimer (Py-PFO-Py)$_2$ $\theta = 90°$ now consists of two components. The spectrum maxima lies between the peak maxima of dimer (Py-PFO-Py)$_2$ $\theta = 0°$ and the monomer Py-PFO-Py, forming a broad band which includes the monomer spectrum.

By completely breaking the π-conjugation of the dimer, we obtain an average spectra which is much closer to that of the monomer. This indicates that the small red shift of ~ 0.15 eV of the dimer (Py-PFO-Py)$_2$ is related to the small degree of π-conjugation between the monomer units seen in Figure 3.6(a). This shift is also captured by using a BPy-PFO-BPy monomer model, as shown in Figure 3.3(c). Here, it is related to an extension of the exciton's electron into the terminating Py rings, shown in Figure 3.3(c).
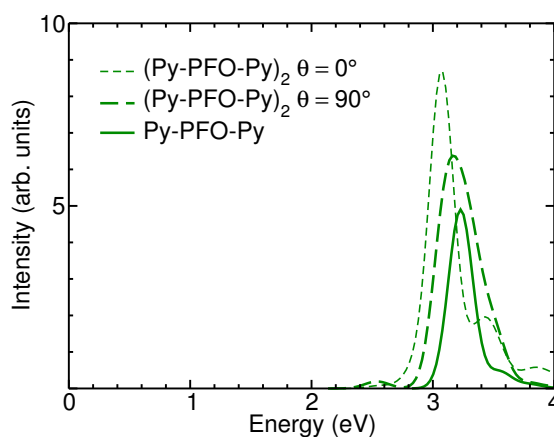
Figure 3.7: TDDFT absorption spectra of planar (Py-PFO-Py)$_2$, i.e. $\theta = 0°$, (Py-PFO-Py)$_2$ having the two pyridines in the bipyridine turned 90 degrees, i.e. $\theta = 90°$, and the Py-PFO-Py monomer.
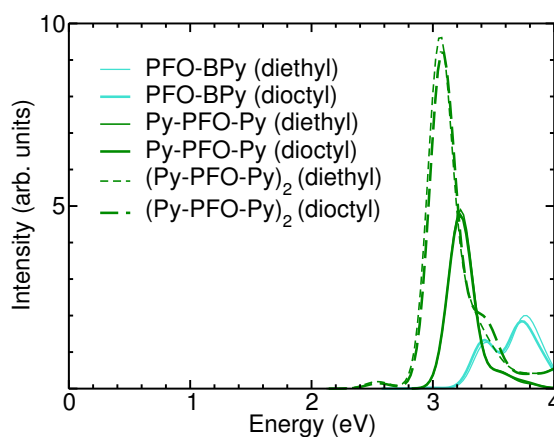
Figure 3.8: TDDFT spectra of Py-PFO-Py (green solid line), (Py-PFO-Py)$_2$ (green dashed line), and PFO-BPy (blue line) with side chains of dioctyl (R$_1$ = (CH$_2$)$_7$CH$_3$, thick lines) and (R$_1$ = CH$_2$CH$_3$, thin lines) side chains (thin line) on the PFO.

To test whether a Py-PFO-Py monomer model would include the steric influence of the side chains on the adsorption on the tube, we reduced the length of the side chain to an ethyl group. The spectra for both monomers as well as for the dimer (Py-PFO-Py)$_2$ show no peak shift in the absorption spectrum after reducing the length of the side chains, as shown in Figure 3.8. These results clearly demonstrate that the length of the side chains has little influence on the optical absorption spectra of the polymer.

This is consistent with what was found by Namal *et al.* while studying the effect of alkyl chain length on the electrochemical properties of fluorine and benzimidazole containing conjugated polymers[233]. In this case, the first absorption band in the visible at 425 nm experiences a blue shift of 20 nm when the length of the side chains is doubled. The slight shift and the measured change of the optical band gap by only 0.08 eV is ascribed to a better solubility of the polymer and a stronger conjugation of the π–system[233].

3.2 Supramolecular Structure Evaluation of Polymer–SWNT Heterojunctions*

Knowing the supramolecular structure of heterojunctions is an important step towards understanding the mechanisms behind the interactions at the interfaces and the sorting behaviour of polymers. The angle of the polymer backbone with respect to the nanotube axis is a key element when defining the supramolecular structure of the polymer–carbon nanotube heterojunction. This angle can be identified using polarized angle-dependent absorption spectroscopy. The experiment can be performed simply with a broadband polarisator (Glan-Thompson-prism) and a ultraviolet spectral region (UV)/visible spectral region (VIS)/near infrared spectral region (NIR) absorption spectrometer. The technique makes use of the anisotropy in a crystalline matrix. The polarization direction of the absorbed light provides information about the orientation of the molecules within the matrix, yet only in the case where one knows the transition dipole moment (TDM) of the molecules. For conjugated polymers the TDM is typically along the polymer's backbone. In cases where there is uncertainty, LR-TDDFT is a good tool for evaluating the TDM. We can illustrate the polarization direction of the light absorbed by resolving the LR-TDDFT spectrum in the x, y, and z directions of the dipole oscillator strengths, whose magnitudes are proportional to the TDM. As shown in the previous section, only the subunit is needed to simulate the spectrum. We used angle-dependent absorption spectroscopy in combination with LR-TDDFT to determine the orientation of the PFO-BPy with respect to the (6,5) SWNT. Our results show that the PFO-BPy is aligned nearly parallel to the nanotube axis. The finding of a straight alignment of the polymer on the SWNT has an impact on the development of future selective polymers.

3.2.1 Sample Fabrication

The sorted PFO-BPy–(6, 5) SWNT heterojunctions and the (6, 5) SWNT as well as the PFO-BPy references were dissolved in chlorobenzene. Polystyrol was then added to the dispersion. The probe was brought onto a glass substrate and heated to $175°C$ until the solvent was evaporated. The probe was pushed together by tweezers, then pressed to a thin film between two glass substrates before cooling down. These steps were repeated until a transparent film was obtained. The 2D matrix was heated again and stretched with tweezers to the final thin film while being adsorbed on one side onto a glass substrate. The detailed sample fabrication can be found in Ref. 234.

3.2.2 Optical Characterization

The PFO-BPy–SWNT and SWNT films were placed in the holder in front of a Glan-Thompson-prism, which was incorporated in the measurement chamber of a Cary 5000-Spectrometer (Varian/Agilent). From each probe the spectrum of parallel polarized light I_p was recorded rotating the probe along the z-axis from 0° to 90° in 15° steps as shown in Figure 3.9. From all spectra the corresponding reference spectrum was subtracted. The data was fitted by global analysis using IGOR Pro 6.3 (WaveMetrics). The detailed measurement procedure and fitting of the data can be found in Ref. 234.

3.2.3 Computational Details

All DFT calculations were performed with locally centered atomic orbitals (LCAOs) and the PAW implementation within the GPAW code [125,126,196]. We used a double-zeta polarized (DZP) LCAO basis set and a grid spacing of 0.2 Å for representing the density and the wavefunctions and the PBE xc-functional [184]. All structural minimizations were performed within the Atomic Simulation Environment (ASE) [230], until a maximum force below 0.05 eV/Å was obtained. We employed more than 5 Å of vacuum to the cell boundaries.

The dipole spectra for the singlet excitations were obtained from transition dipole matrix elements, which we obtained from LR-TDDFT calculations using the local density approximation (LDA) exchange correlation (xc)-functional.

The electron/hole average density is obtained by integrating the density of the excitonic wavefunction with respect to the hole/electron's position. To compute the average electron/hole densities, we include transitions ranked by their weight f_{nij} until $\sum f_{nij}^2 > 0.95$, as explained in section 2.5.1.

3.2.4 Polarized Angle-Dependent Absorption Measurements

When the polymer–SWNT systems are brought into a 2D matrix, the systems are forced into an ordered network. The ordered, in this case parallel, arrangement of the SWNTs leads to an anisotropic behaviour of the matrix. The TDM of the SWNTs first excited state in SWNTs (E_{11}) and second excited state in SWNTs (E_{22}) transitions are along the tube axis.[130,131] Therefore, both transitions occur when light polarized parallel to the SWNT axis is absorbed, as shown in the angle-dependent spectra in Figure 3.10 (a). The strongest absorption occurs when the SWNT's axes are along the x-direction in the experimental setup, that is, when the sample is at $0°$. In Figure 3.10 (b) the angle devolutions of the SWNT (red) and PFO-BPy (blue) are shown. We clearly see that the polymer absorbance has the
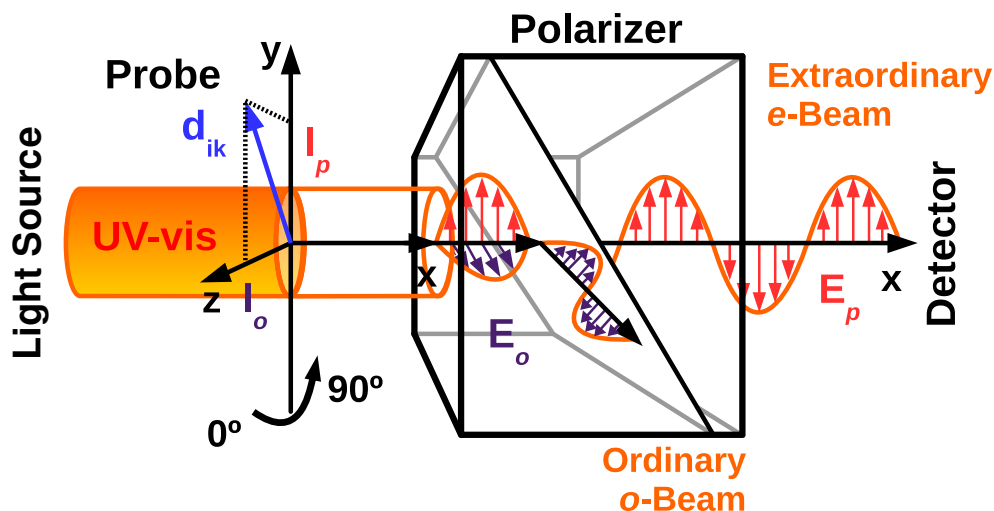
Figure 3.9: Schematic of polarized angle-dependent spectroscopy setup: Rotating transition dipole moment vector $\mathbf{d}_{ik}$ due to rotation of probe from $0°$ to $90°$ around the x-axis, projected partial absorption of parallel polarized light I_p on the y-axis and orthogonal polarized light I_o on the z-axis, and the detection of the % absorbed of parallel/vertical polarized light after its retrieval from a polarizer (Glan-Thompson-prism).
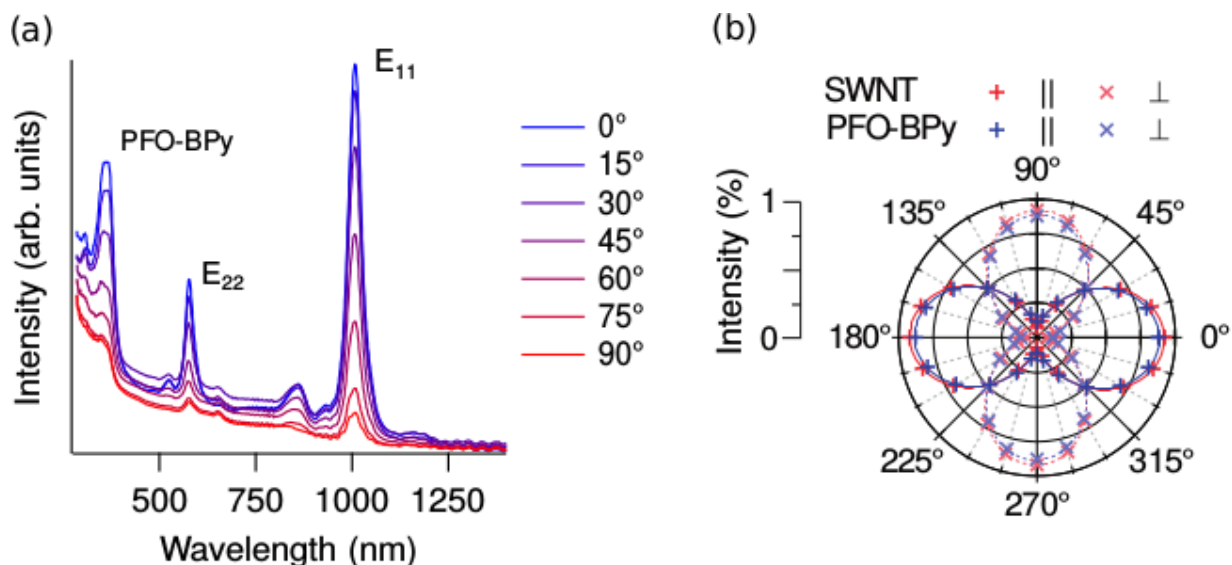
Figure 3.10: (a) Polarized angle-dependent spectra or spectra of parallel polarized light of PFO-BPy–SWNT sample with rotation from 0° (blue) to 90° (red). (b) Angle devolution of SWNT (red) and PFO-BPy (blue) components.

same angle-dependence as the carbon nanotubes and therefore the same polarization. Knowing the polarization of the polymer, its orientation with respect to the SWNT can be determined by the TDM of the polymer's transitions at 365 nm. It has to be mentioned that the PFO-BPy reference sample shows anisotropic behaviour as well due to the stretching of the matrix. However, the reduction of the peak intensity from 0° (blue) to 90° (red) in the PFO-BPy–SWNT sample is 1.7 times stronger compare to the PFO-BPy Ref. 234.

3.2.5   Linear Response TDDFT Calculations

A parallel polarized electromagnetic wave has its electric field vector $\mathbf{E}_p$ (red) oscillating in the y-direction, as shown in Figure 3.9. A single-photon transition including the molecules' states $i \rightarrow k$ depends on the polarization (direction) of the transition given by the TDM, $\mathbf{d}_{ik}$, relative to the polarization of electric field of the wave, $\mathbf{E}$. Thus, the intensity of light absorption is maximal or zero, respectively, in the case the electric field vector $\mathbf{E}_p$ of the excitation wave oscillates parallel or orthogonal to $\mathbf{d}_{ik}$, respectively.

Figure 3.11 shows the LR-TDDFT absorption spectrum of the Py-PFO-Py unit, the dipole oscillator strengths contributions in the x, y, and z directions, and the molecular structure of the Py-PFO-Py unit. The hydrogen atoms marked in black in the Py-PFO-Py unit denote the links of the units in the polymer. The results reveal that the Py-PFO-Py transitions occur when the electric field is polarized along the y-direction (blue), that is, along the polymer's backbone. From this it follows that the PFO-BPy polymer backbone has to be streched out along the y direction in the experimental setup shown in Figure 3.9, when the sample is at 0°. Only when aligned in the y-direction does Py-PFO-Py absorb parallel polarized light, $\mathbf{E}_p$, which oscillates in the y direction.
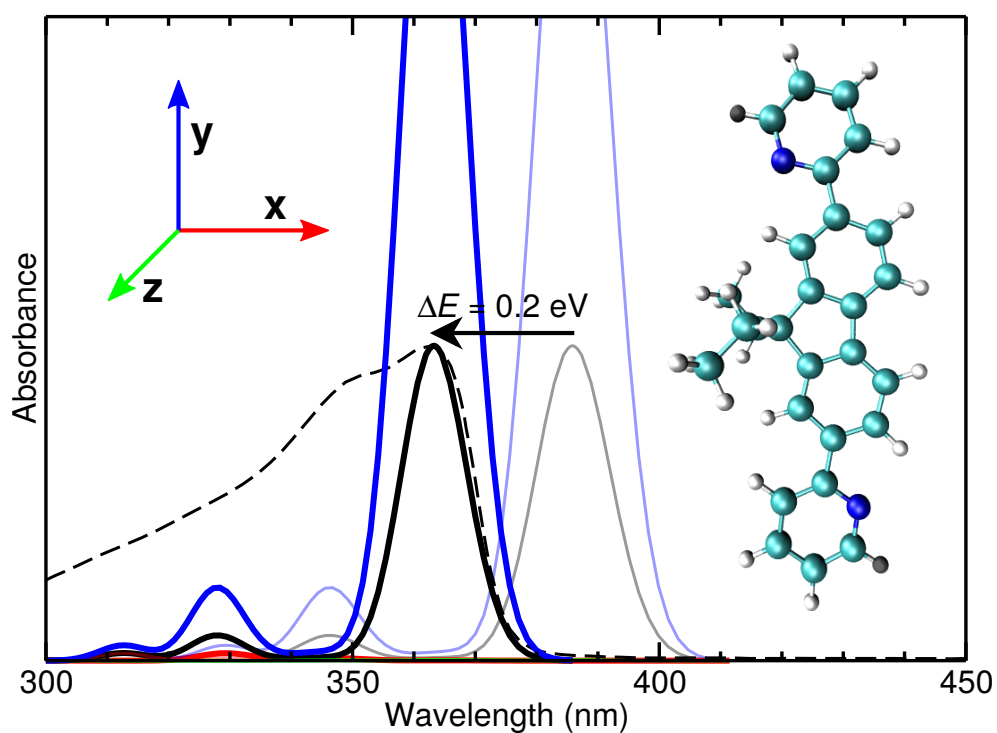
Figure 3.11: Comparison of the average (black) LR-TDDFT absorption spectrum (solid lines) of the Py-PFO-Py unit, and dipole oscillator strength contributions in the *x* (red), *y* (blue), and *z* (green) directions, with the measured spectra (black dashed line) before (light thin lines) and after (dark thick lines) applying a common energy shift of $\Delta E = 0.2$ eV. The molecular structure of the Py-PFO-Py unit aligned in the *y*-direction is shown as an inset, with C and H atoms depicted by cyan and white balls, respectively, while black balls denote links between units in the polymer.

3.3   Modelling Photoinduced Transient Absorption Spectroscopy*

In this work, we employ state-of-the-art pump-probe transient absorption spectroscopy to measure the excited state dynamics of a (6,5) and (7,5) SWNT mixture, and combined with poly(3-hexylthiophene-2,5-diyl) (P3HT) and phenyl-C_{61}-butyric acid methyl ester (PCBM) in P3HT:PCBM:SWNT blended samples in the NIR. We then employ LR TDDFT in frequency-reciprocal space within the RPA to model the measured transient spectra for (6,5) and (7,5) SWNTs and blended P3HT:PCBM:SWNT samples.

We begin by providing details of the sample fabrication in section 3.3.1, optical characterization of the sample in section 3.3.2, the theoretical methods employed in section 3.3.3, and computational parameters used in section 3.3.4. In section 3.3.5 we provide a detailed comparison of the absorbance and differential transmission spectra obtained for our SWNT and blended P3HT:PCBM:SWNT samples with those available in the literature in the near-infrared spectral region (IR) region as a function of the pump-probe delay. We show in section 3.3.6 how the differential transmission spectra may be interpreted in terms of a difference in absorption spectra. After briefly justifying our method for modelling optically excited states in section 3.3.7, we employ LDR-TDDFT-RPA calculations of (6,5) SWNTs, (7,5) SWNTs, and a combined polythiophene (PT):PCBM:(6,5) SWNT system in section 3.3.8 to simulate the measured differential transmission spectra, and explain the dependence of the observed photoinduced absorption (PA) peak on charge carrier density in section 3.3.9 and the photobleach (photobleach (PB)) peak width in section 3.3.10. This is followed by concluding remarks. A derivation of the LDR-TDDFT-RPA formalism, and the influence of LFEs on the SWNT spectra are provided in Appendix B.

3.3.1   Sample Fabrication

The glass substrates were pre-cleaned with acetone and isopropanol and dried under a flow of dry nitrogen. For preparation of the samples, regular P3HT and PCBM were dissolved in ortho-dichlorobenzene (ortho-dichlorobenzene (ODCB)) at a 1:1 ratio. We employed 704148-SWNTs produced using the cobalt-molybdenum catalyst (CoMo-CAT®)® catalytic chemical vapour deposition (chemical vapor deposition (CVD)) method. The SWNTs were also dispersed in ODCB and then sonicated for 1 hour. No debundling or removal of metallic SWNTs was performed on the sample, which was most likely aggregated. The resulting solution was then spin-coated on top of the glass substrates to obtain the SWNT sample. In the case of the P3HT:PCBM:SWNT sample, the dispersed SWNTs were added to the P3HT:PCBM solution at a 1:1:1 ratio and then sonicated for 1 hour. The solution was then spin-coated on top of the glass substrates at 1000 rpm for 2 minutes. All the materials were bought from Sigma-Aldrich.

3.3.2   Optical Characterization

The ground state absorption spectra were collected with a PerkinElmer spectrophotometer (Lambda 1050 WB In-GaAs 3D WB Detection Module). The laser system employed for ultrafast transient absorption was based on a Ti-Sapphire chirp pulse amplified source; with a maximum output energy of about 800 µJ, 1 kHz repetition rate, central wavelength of 780 nm and pulse duration of about 180 fs. Excitation pulses at 590 and 900 nm were generated by noncollinear optical parametric amplification in a β-barium borate (BBO) crystal, with a pulse duration of around 100 fs. Pump pulses were focused in a 200 µm diameter spot. Probing was achieved in the visible and near
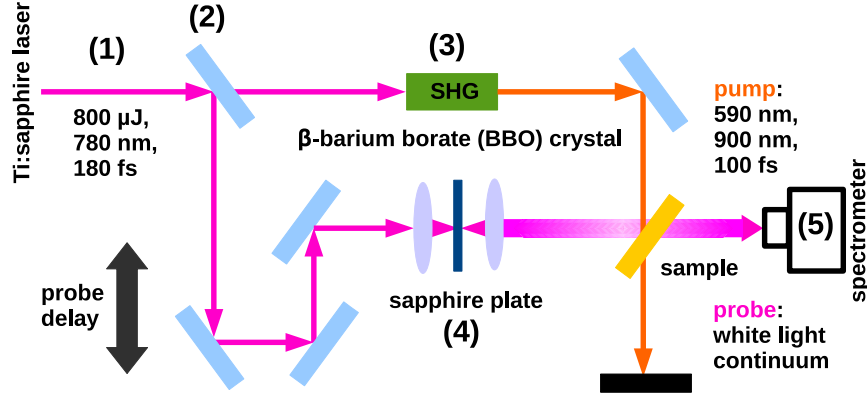
Figure 3.12: Schematic of simplified femtosecond transient absorption spectroscopy setup; (1) pulse generation in self-mode-locked Ti:sapphire laser, (2) beam splitting, (3) second harmonic generation (SHG) by BBO crystal to obtain pump pulses, (4) white light continuum generation by sapphire plate to obtain probe pulse, (5) detection of pump and delayed probe by spectrometer with fast optical multichannel analyzer (OMA) with a dechirping algorithm.

IR region by using white light generated using a thin sapphire plate. Chirp-free transient transmission spectra were collected by using a fast optical multichannel analyzer (OMA) with a dechirping algorithm. The measured quantity is the differential transmission, $\Delta T = T(t) - T(t = 0)$. Once normalized, the differential transmission $\Delta T/T$ may be directly compared with the change in absorbance $\Delta \text{Im}[\varepsilon] = \text{Im}[\varepsilon(t = 0)] - \text{Im}[\varepsilon(t)]$. The excitation energy has been set to 11 nJ when pumping at 590 nm and then increased to 200 nJ when pumping at 900 nm, i.e., selectively pumping the SWNTs. All measurements were performed in air at room temperature.

3.3.3 Theoretical Methods

To model differential transmission measurements, we use the difference between the optical absorption of the system in the ground and excited states. We model the system in the excited state within DFT by fixing the total magnetic moment μ, and through the addition of charge Q to the system. Specifically, we use the singlet ($S = 0$) to model the ground state, the triplet ($S = 1$) to model a single exciton, the quintet ($S = 2$) to model a pair of excitons, and the quartet ($S = 3/2$) with an additional charge $Q = -e$ to model a negative trion, i.e., a pair of excited electrons and a single hole.

The optical absorption spectra are obtained via LDR-TDDFT-RPA [119–121,207,232], from the imaginary part of the macroscopic dielectric function, $\text{Im}[\varepsilon(\mathbf{q}, \omega)]$, in the limit $\|\mathbf{q}\| \rightarrow 0^+$. Details of our implementation are provided in Appendix B.

To model an excited singlet state of the system based on a fixed magnetic moment calculation, we "swap" between the spin channels ($s \in \{\uparrow, \downarrow\}$ or $\{0, 1\}$) the eigenvalues and eigenfunctions of the levels beyond half the number of electrons, $N_e/2$. More precisely, we define

$$s' = \begin{cases} s + 1 \mod 2 & \text{if } n > N_e/2 \\ s & \text{otherwise} \end{cases}. \tag{3.1}$$

In this way we obtain the electronic structure of a singlet excited state that is constrained to have the same total electron density as the triplet ground state, $\rho_{ex}^{S=0}(\mathbf{r}) \equiv \rho_{gs}^{S=1}(\mathbf{r})$.

Note that, as we are primarily interested herein with the absorption spectra near their onsets, LFEs may be neglected without impacting our results. This is demonstrated in Appendix B, where we compare ground state LDR-TDDFT-RPA spectra for a (6,5) SWNT with and without including LFEs.

3.3.4 Computational Details

All DFT calculations were performed with LCAOs and the projector augmented wave (PAW) implementation within the GPAW code[125,126,196]. We used a double-zeta polarized (DZP) basis set for representing the density and the wavefunctions and the PBE exchange correlation (xc)-functional[184]. All calculations employed a room temperature Fermi filling ($k_B T \approx 25$ meV), with total energies extrapolated to $T \to 0$ K, i.e., excluding the electronic entropy contribution to the free energy $-ST$. In this was we avoided an unrealistic smearing of the excited electron and hole in the triplet calculations. We included $\frac{2}{3}N_e$ many bands within the calculations, which has been shown to be sufficient to converge the first $\pi \to \pi^*$ transitions within graphene[232].

Structural minimization was performed within the Atomic Simulation Environment (ASE)[230], until a maximum force below 0.05 eV/Å was obtained. We employed more than 5 Å of vacuum to the cell boundaries orthogonal to the (6,5) SWNT, (7,5) SWNT and polythiophene (PT), and obtained optimized unit cells parameters of 40.92, 44.79, and 7.87 Å along their axes, respectively. Here, PT is modeled using two thiophene units in s-trans configuration. We have used PT as a simplified model for P3HT, that is, removed the hexyl side chains of P3HT, since the influence of the P3HT side chains on the level alignment and charge transfer is negligible[121,233]. Moreover, as we shall see in section 3.3.5, the influence of P3HT/PT on the IR spectrum of the SWNT is solely through hole-transfer.

The PT:PCBM:(6,5) SWNT bulk was modeled by a 39.34×40.92 Å^2 layered structure of ten thiophene units orthogonal to the SWNT axis, as shown in Figure 3.13(a). In so doing, this configuration describes the limit of a minimal SWNT–PT overlap. To determine the impact of increasing the SWNT–PT overlap, we also consider a truncated ten unit PT chain aligned with the SWNT and PCBM as shown in Figure 3.13(b).

It has previously been shown that changes in the orientations of PCBM next to P3HT only cause energy differences within the accuracy of DFT[118]. Since the potential energy surface is rather flat[118], we have chosen a smallest C–C intramolecular distance of ~ 3.3 Å between the relaxed P3HT, PCBM, and SWNT structures, and performed single-point calculations for the resulting configurations shown in Figure 3.13. Although this C–C separation is 0.1 Å smaller than the interlayer distance of multi-walled carbon nanotubes (MWNTs) and graphite[235], it has been chosen to ensure an overlap between the SWNT and PT outer LCAO orbitals. An increase of the PT–PCBM:SWNT distance to ~ 3.4 Å changes the total energy by less than 50 meV, i.e., within the accuracy of DFT. In each case we found the repulsive forces for the close lying C atoms were $\lesssim 0.1$ eV/Å.
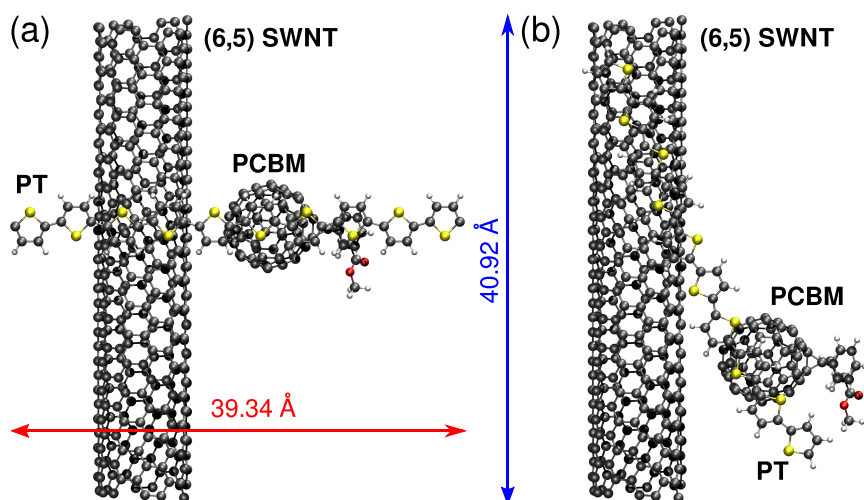
Figure 3.13: Schematic of the PT:PCBM:SWNT system with (a) a periodically repeated PT polymer aligned orthogonal to the SWNT and (b) a finite ten unit PT chain aligned with the SWNT. C, H, O, and S atoms are depicted by gray, white, red, and yellow balls, respectively.

3.3.5 Differential Transmission Measurements

Figure 3.14 shows the transient spectra of the SWNT and blended P3HT:PCBM:SWNT samples versus probing delay times up to 5 ps. In both spectra, we find a peak with a maximum around 1025 nm. Comparing the transient spectra with the absorbance (black) in Figure 3.15(a), this peak can be assigned to the photobleach (PB) of mainly (6,5) and (7,5) SWNT E_{11} transitions[237]. For the blended sample, we have an additional PA peak around 960 nm. The samples show a remarkable difference in the decay rate of the PB peak. In the case of the SWNT sample, the E_{11} transitions seem to be completely accessible again after 1 ps, while the decay of the E_{11} exciton in the blended sample is 4–5 times longer.

The UV/VIS/NIR absorption spectra of the SWNT sample are shown as an inset to Figure 3.15(a). The E_{22} transitions of (6,5) and (7,5) SWNTs are clearly visible, with the E_{11} transition of (11,5) SWNTs seen as a shoulder.

By comparing the transient spectra of the SWNT sample (black) at delay times of 0.2, 0.3, and 1 ps with the spectra of similar SWNT samples of the literature at the same delay times, we found a discrepancy within the measured peak width and structure of the SWNT sample spectrum and those of the literature[144,145,236], as shown in Figure 3.15(b-d). The (6,5) SWNT enriched samples of Refs 144 (blue) and 145 (magenta) show a much smaller peak width and an additional PA peak between 940 and 975 nm. The PA peak in the sample of Ref. 236 (cyan) is overlaid by the PB of the (8,3) SWNT (~ 966 nm)[237] and therefore not strongly pronounced. As well, the width is broader due to the mixture of tubes. This is consistent with the differential transmission of our SWNT sample.

To determine whether the pump energy has an influence on the peak width, the SWNT sample was pumped at two different wavelengths: 590 nm in the VIS and 900 nm in the IR. These pump energies are comparable to those reported the literature[144,145,236]. For example, Ref. 236 pumped in the infrared region at 930 nm, while the pump beams at 570 nm employed in Refs 144 (blue) and 145 (magenta) were tuned to the E_{22} transition.

As shown in Figure 3.15(b,c,d), the differential transmission spectra for our SWNT sample is rather insensitive to whether pumping is in the VIS or IR. This suggests that the broader PB peak within our SWNT sample, shown in
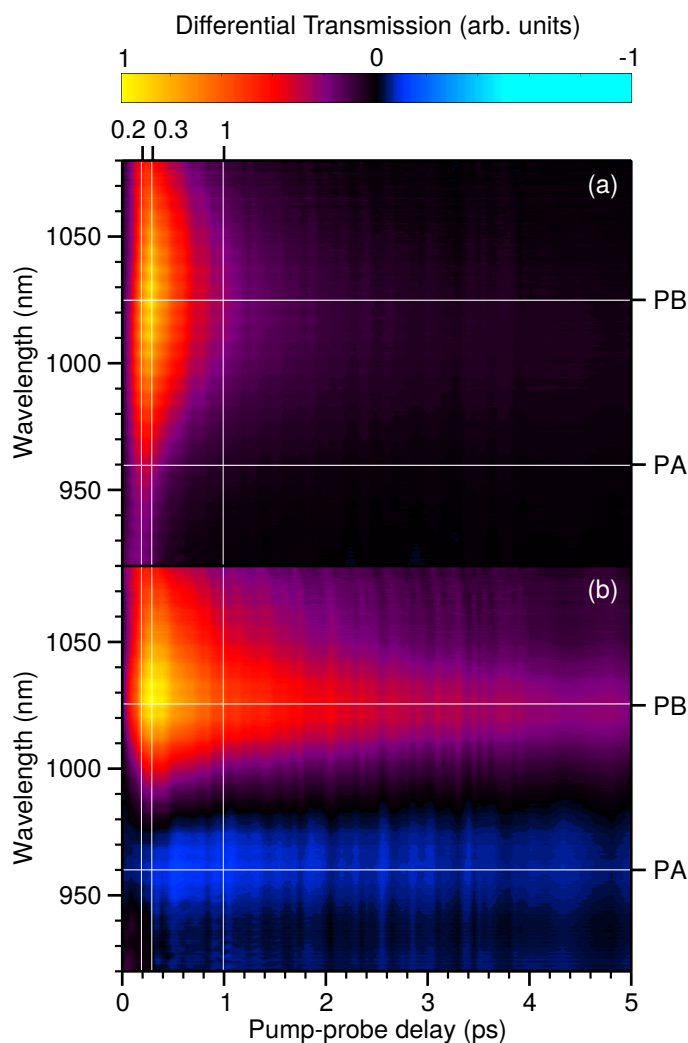
Figure 3.14: Normalized differential transmission $\Delta T/T$ of (a) SWNT and (b) P3HT:PCBM:SWNT devices versus pump-probe delay in ps and probe wavelength in nm. Pump-probe delays of 0.2, 0.3, and 1.0 ps (spectra in Figure 3.15) are marked by vertical lines, while photobleach (PB) and photoabsorption (PA) peaks (spectra in Figure 3.16) are marked by horizontal lines.

Figure 3.15(a), is related to the sample itself. It has previously been argued that SWNT mixtures have an increased exciton transfer and electron-hole trapping between tubes[74,97]. Thus, the greater PB peak width in our SWNT sample may be related to having a mixture of both (6,5) and (7,5) SWNTs. However, having a SWNT mixture does not explain the occurrence of the PA peak in the blended P3HT:PCBM:SWNT sample (red).

Taking a closer look at the transient spectrum of the SWNT sample in Figure 3.15(b,c,d), we notice it exhibits a small asymmetry. Nevertheless, including a range of ±50 nm from the peak maximum, this asymmetry cannot be completely verified, as it is within the noise of the measurement. Thus, the PA appears to completely vanish in the spectra of the SWNT sample.
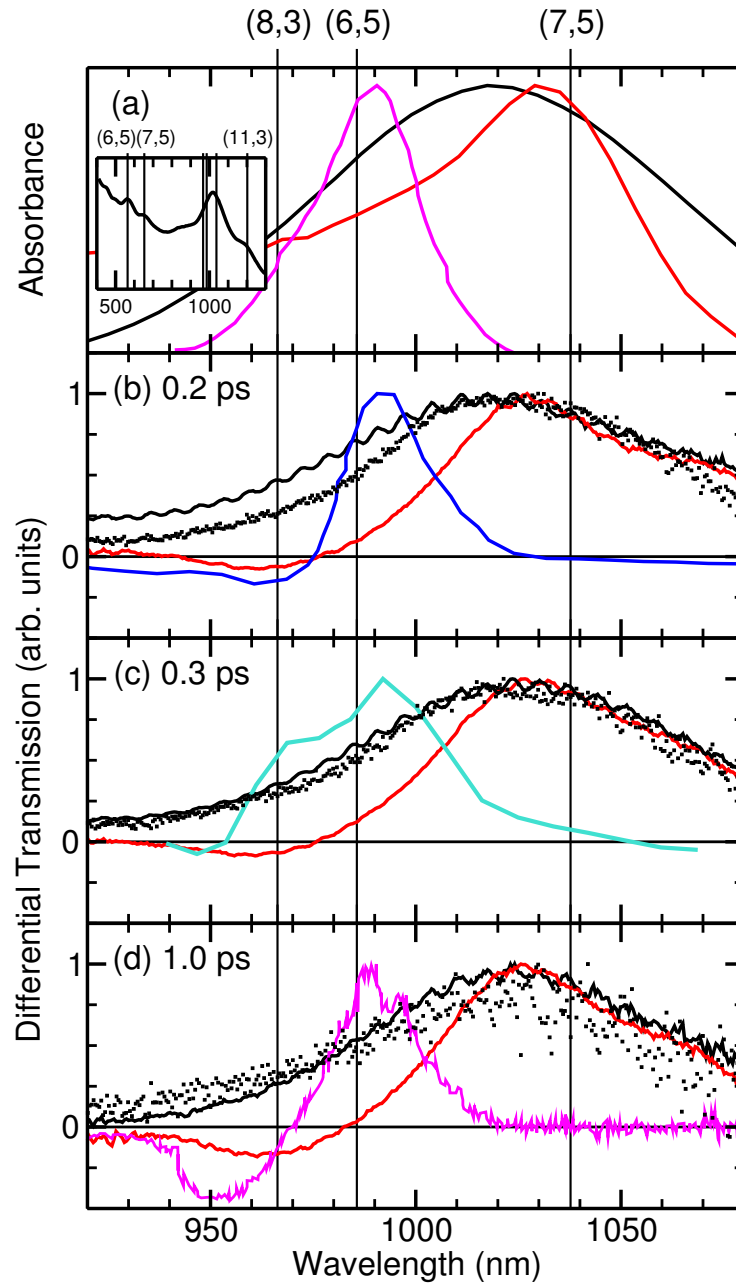
Figure 3.15: Normalized (a) absorption and (b-d) differential transmission $\Delta T/T$ versus probe wavelength in nm for our SWNT sample (black) pumped at 900 nm (solid line) and 590 nm (squares), combined P3HT:PCBM:SWNT device (red) and from Refs 144 (blue), 236 (cyan), and 145 (magenta) for pump-probe delays of (b) 0.2 ps, (c) 0.3 ps, and (d) 1.0 ps. Wavelengths of the E_{11} transitions for (8,3), (6,5), and (7,5) SWNTs from Ref. 237 are marked above.
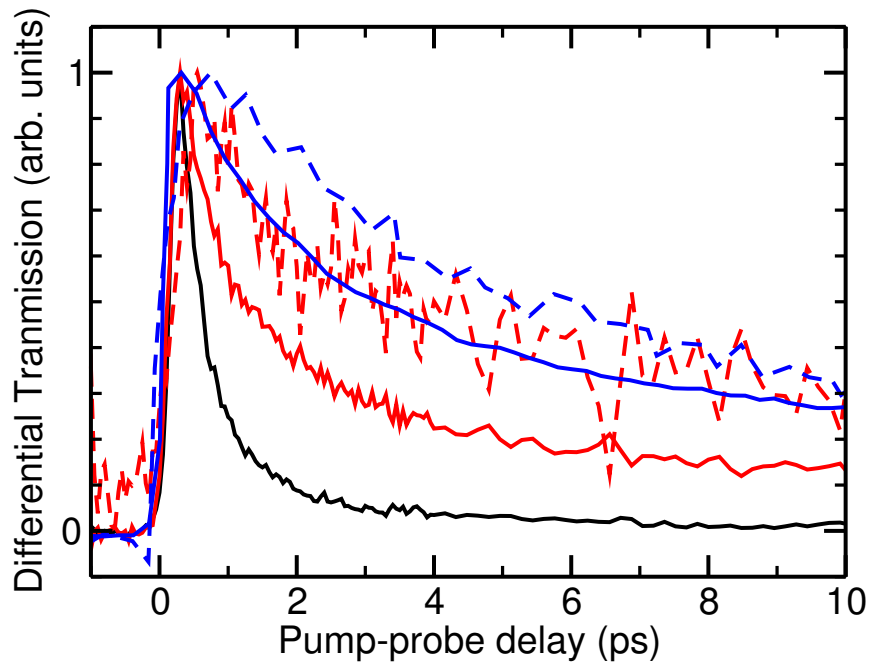
Figure 3.16: Normalized differential transmission $\Delta T/T$ as a function of the pump-probe delay in ps measured at the maximum of the photobleach (PB) peak (solid lines) and photoabsorption (PA) peak (dashed lines) for our SWNT sample (black), combined P3HT:PCBM:SWNT device (red), and for (6,5) SWNTs from Ref. 144.

The recovery time dynamics of the PB and PA peaks for the mixed SWNT sample and the P3HT:PCBM:SWNT blended sample are shown in Figure 3.16.

We find the mixed SWNT sample's recovery time is much shorter than that of the blended P3HT:PCBM:SWNT sample, with the recovery time reported in Ref. 144 for a predominantly (6,5) SWNT sample even longer. In each case, the PA peaks seem to recover as fast as the PB peaks or slightly slower.

The main reason for the extinction of the PA peak is the large peak width, which is crucial for the visibility of the PA peak. However this does not explain its origin.

3.3.6   Interpreting Differential Transmission as a Difference Spectra

Zhu et al. [144] found a PA peak, and suggested it is due to a biexcitation. In a subsequent paper, Zhu [145] suggested coupling to the radial breathing mode as a reason for the PA peak.

Evaluating the experimental data of Ref. 145 shown in Figure 3.17, we identified the peak causing the PA peak by taking the difference between the normalized absorbance (violet) and the normalized transient spectrum (magenta). This results in the difference spectrum of the probe beam (green), when the system is fully excited by the pump beam, that is, all electrons of the E_{11} transition are in the conduction band minimum (CBM). In this case, the excited system gives rise to an absorbance of more than 50% of the PB peak but at the energy of the PA peak.

Suppose the PA peak is due to absorption by an excited electron, i.e., an excited electron transition E_{**}, as depicted schematically in Figure 3.17. It should be noted that the single particle picture employed here refers to the
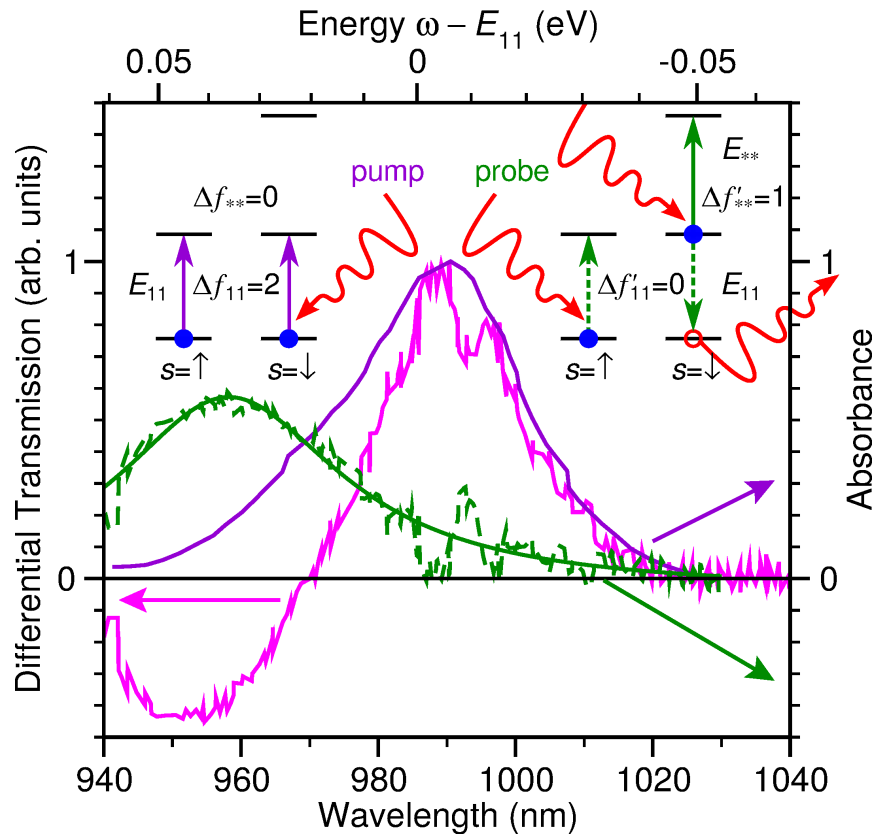
Figure 3.17: Normalized initial absorbance (violet) and differential transmission $\Delta T/T$ with a pump-probe delay of 1 ps (magenta) from Ref. 145, and their difference (green) versus probe wavelength in nm and energy in eV relative to the E_{11} transition. A Lorentzian fit to the difference between the initial absorbance and differential transmission is also shown. An excited electron transition E_{**} model for the measured absorbance/differential transmission is shown schematically in the upper left/right inset.

system being excited, rather than the excitation process itself. When the system is initially excited by the pump, the difference in filling for the E_{11} transition, $\Delta f_{11} = 2$, while the difference in filling for the E_{**} transition's levels $\Delta f_{**} = 0$. When the system is subsequently excited by the probe, that is, in the presence of an exciton, $\Delta f'_{11} = 0$, while $\Delta f'_{**} = 1$. Since a transition's intensity is proportional to the difference in filling, the 2:1 ratio between PB and PA peaks is already accounted for by $\Delta f_{11} : \Delta f'_{**}$. This requires the E_{11} and E_{**} transitions to have almost the same overlaps.

Although this does not rule out the possibility of an E_{**} transition being responsible for the PA peaks close to the PB peaks within the SWNT systems, it makes it rather unlikely. More importantly, it suggests the PA and PB peaks most likely arise from the same E_{11} transition. In fact, in section 3.3.8 we will show that the E_{11} transition is blue shifted by a band gap widening in the excited state, potentially explaining the origin of the PA peak.

3.3.7 Modelling Optically Excited States

As discussed in section 3.3.3, we model the optically excited state using a singlet excited state whose total electron density is constrained to be that of the triplet ground state. This singlet excited state is a suitable approximation to the optically excited state if the spin densities associated with the KS valence band maximum (VBM) and CBM eigenfunctions, $|\psi_{\text{VBM}s}|^2$ and $|\psi_{\text{CBM}s}|^2$, are only weakly dependent on the spin channel s. In other words, if the two spin channels in the triplet DFT calculation are basically equivalent up to a phase factor, i.e., $|\langle \psi_{n\uparrow}^{S=1} | \psi_{n'\downarrow}^{S=1} \rangle| \approx \delta_{nn'}$, the optically excited state should have a similar electron density. If, moreover, the singlet and triplet ground state eigenfunctions are also basically equivalent up to a phase factor, i.e., $|\langle \psi_{ngs}^{S=1} | \psi_{n'gs}^{S=0} \rangle| \approx \delta_{nn'}$, this singlet excited state should describe the optically excited state quite well.

We find this is indeed the case for the (6,5) and (7,5) SWNTs, with the KS eigenfunctions having approximately the same spatial distribution in the singlet and triplet ground states. For the blended SWNT/PT/PCBM systems, the KS eigenfunctions have similar spatial distribution in both spin channels for the triplet DFT calculation, but differ from the singlet ground state KS eigenfunctions. In particular, the occupied CBM level of the triplet DFT calculation is a hybridization of the first three conduction band (CB) eigenfunctions from the singlet ground state calculation. This is indicative of charge transfer in the blended SWNT/PT/PCBM system.

Overall, these results strongly suggest that the total electron density of the triplet DFT calculation should be quite similar to that of the optically excited state. This justifies our use of the singlet excited state electronic structure, obtained by "swapping" between spin channels the CB eigenvalues and eigenfunctions of the triplet ground state, to model the optically excited state.

3.3.8 LDR-TDDFT-RPA Simulated Spectra

The differential transmissions in the long term limit of the (6,5) SWNT (black) and bulk PT:PCBM:SWNT systems (red) in Figure 3.18 are calculated using the difference between the LDR-TDDFT-RPA ground state (violet) and excited state (green) absorbances. The ground state absorbance of the bulk system (dashed) shows the onset of PT absorbance at ~ 925 nm, orthogonal to the E_{11} transition. In the range of 925 to 1100 nm, both systems, the (6,5) SWNT and the bulk, overlap. This suggests that neither PT nor PCBM transitions are involved within this energy range, and there are only (6,5) SWNT transitions. The excited state absorbances (green) of both systems show two significant changes: the PB peak is shifted to higher energy and there is a new transition at ~ 880 nm. This new peak with rather low intensity is absorbing orthogonal to the tube axis, and can be assigned to an intratube interband transition E_{**} of the excited electron in the CBM to an energy level ~ 1.1 eV above the CBM. However, this peak vanishes when LFEs are included, as shown in Appendix B, which may be related to modelling debundled SWNTs[238].

The schematic in Figure 3.18 explains the origin of the E_{11} transition shifts in the excited states. As discussed in section 3.3.3, we modeled the excited state by computing a triplet state in the first step. The singlet excited state is obtained by swapping the eigenenergies and eigenfunctions between spin channels for the originally unoccupied states, i.e., $n > N_e/2$. In this way, the electron and the hole are arranged in the same spin channel. As a result, the bands including the electron and hole are shifted closer in energy (electron-hole binding), while the other channel with the electron in the valence band (valence band (VB)) increases its band gap. This is not seen in the triplet calculation itself. Due to this widening of the band gap, the second excitation of an electron in the VB is at higher energy.
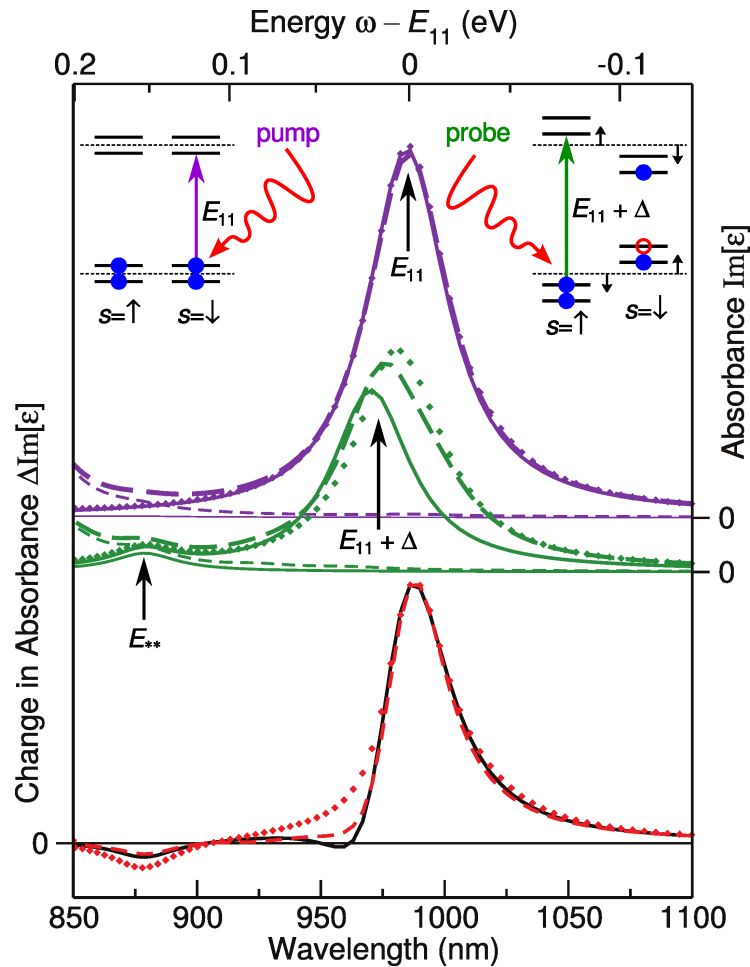
Figure 3.18: The LDR-TDDFT-RPA absorbance Im[ε] of a (6,5) SWNT (solid lines) and for the combined PT:PCBM:SWNT system depicted in Figure 3.13(a) (dashed lines) and (b) (diamonds) in the ground/excited state by the pump/probe (violet/green) as depicted schematically in the upper left/right inset, and change in absorbance between the ground and excited state for a (6,5) SWNT (black) and a combined PT:PCBM:SWNT system (red) versus wavelength in nm and energy in eV relative to the E_{11} transition. Total absorbance (thick lines) and absorbance for light polarized perpendicular to the SWNT axis (thin lines) are shown.

In the changes of the absorbance, i.e., differential transmission in the long term limit, the E_{**} transitions give rise to negative peaks. However, they are at much higher energy than the PA peaks measured experimentally. On the other hand, the shifts Δ of the E_{11} transitions in the excited state cause a reduction of the transient absorbance peaks at ~ 960 nm. The larger shift within the (6,5) SWNT system even leads to a small negative peak in the change in absorption. Overall, the (6,5) SWNT difference spectrum agrees qualitatively with that of Ref. 144, shown in Figure 3.15(b).

This is exactly the opposite from what we see in the experimental data obtained from the SWNT and the blended samples. There, we have no PA in the transient spectrum of the SWNT sample, but a more pronounced reduction of

the peak at the higher energy end for the blended sample spectrum. To understand the origin of this discrepancy, we consider the role of charge carrier loading, i.e., addition and removal of electrons and holes, and peak broadening on the differential transmission spectra in the following sections.

3.3.9 Role of Charge Carrier Loading
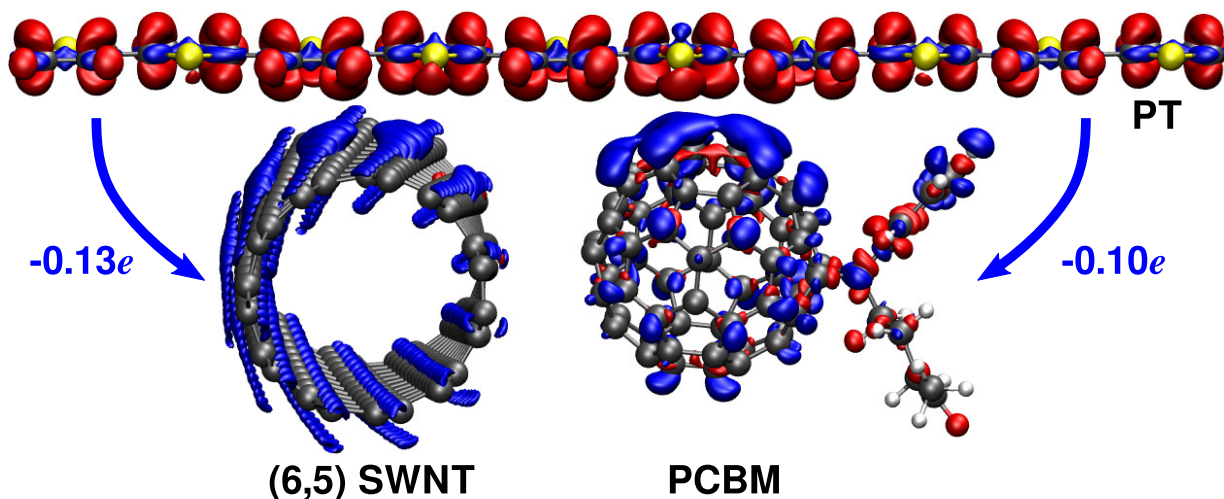
Figure 3.19: Electron (blue) and hole (red) densities for a combined PT:PCBM:SWNT system from the DFT total electron density difference between the excited and ground state. The charge transfer upon excitation of $-0.13e$ from the PT to the (6,5) SWNT and of $-0.10e$ from PT to PCBM is depicted schematically. C, H, O, and S atoms are depicted by gray, white, red, and yellow balls, respectively.

We calculated the excited electron (blue) and hole (red) densities as the difference between the electron density in the ground state and triplet configuration, as shown in Figure 3.19.

In this way we include all electron redistributions in the VB and CB. The difference in the densities reveals a hole located mainly on P3HT/PT, whereas the electron is predominantly on the (6,5) SWNT and the PCBM. This results in a net charge transfer of 0.23 electrons from the PT to its neighbouring molecules. The amount of calculated charge transfer within the bulk system is in agreement with previous DFT results for P3HT–fullerene and P3HT–SWNT heterojunctions[160,161].

The charge transfer within the bulk system partially fills the hole in the excited state. This transfer of charge from PT into the (6,5) SWNT VBM stabilizes it, making the band gap widen less than in the isolated (6,5) SWNT system. Even though the transition is more intense, due to the additional electrons, the reduction of the PB peak at the high energy end is less pronounced due to the smaller shift Δ.

To determine how the amount of hole transfer from the SWNT and higher loading of charge carriers influences the shape of the transient spectrum at the E_{11} transition of SWNT systems, we have increased the amount of charge carriers on the (6,5) and (7,5) SWNTs from 0.24 and 0.22 to 0.49 and 0.45 e/nm, respectively. In Figure 3.20 we compare the change in LDR-TDDFT-RPA absorption Im[ε] (from eq 2.67 of Appendix B) of (6,5) and (7,5) SWNTs with (a) a single exciton, (b) a negative trion, i.e., a pair of excited electrons and a single hole, and (c) a pair of excitons. Unsurprisingly, with the addition of a second exciton, as shown in Figure 3.20(c), the widening of the band
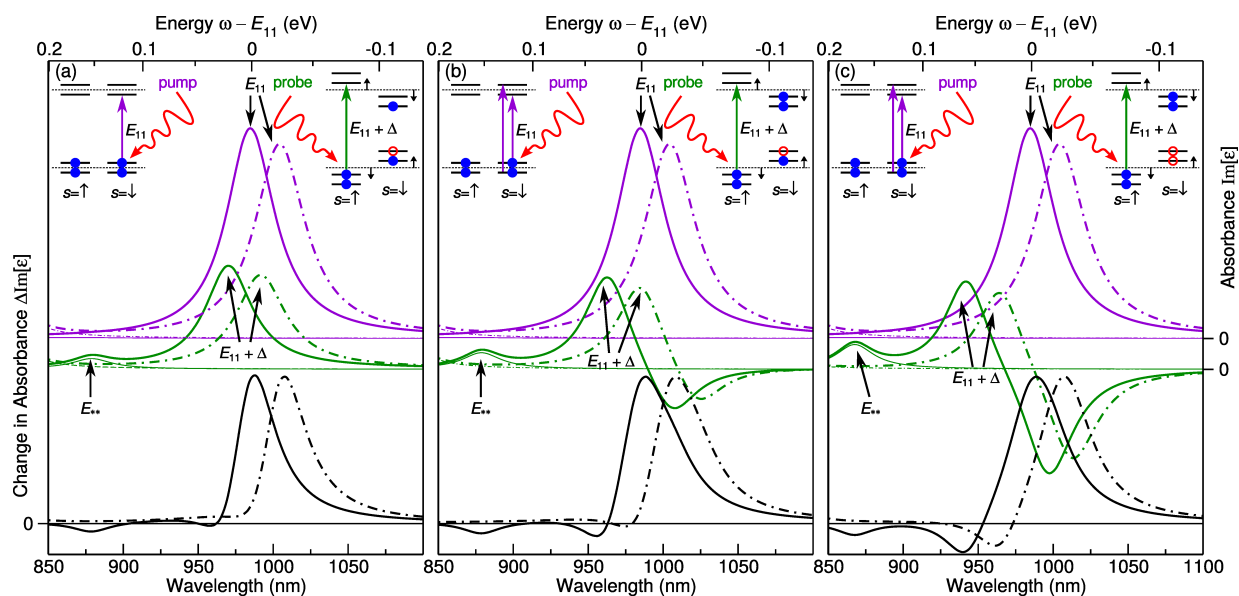
Figure 3.20: LDR-TDDFT-RPA absorbance Im[ε] of a (6,5) SWNT (solid lines) and (7,5) SWNT (dashed-dotted lines) in the ground/excited state by the pump/probe (violet/green) as depicted schematically in the upper left/right inset, and change in absorbance between the ground and excited state versus wavelength in nm and energy in eV relative to the E_{11} transition of a (6,5) SWNT. The excited state is modeled by (a) a single exciton, (b) a negative trion, and (c) a pair of excitons. Total absorbance (thick lines) and absorbance for light polarized perpendicular to the SWNT axis (thin lines) are shown.

gap Δ is significantly increased, resulting in a stronger PA peak at higher energy ($\sim$ 940 nm for the (6,5) SWNT). These results are consistent with the predominantly (6,5) SWNT measurements of Ref. 145 after a 1 ps pump-probe delay, as shown in Figure 3.15(d). There, the PA peak is at $\sim$ 950 nm and even gains half of the intensity of the PB peak. Additionally, the existence of a second exciton within a 4 nm unit cell is quite reasonable, as compared to the calculated exciton size of $\sim$ 2 nm[134]. In Figure 3.20(b) one of the holes is filled, e.g., through charge transfer from P3HT to a SWNT, the PB peak becomes more asymmetric, and the PA peak becomes less intense. These results are more in agreement with the measurements after a 0.2 ps pump-probe delay of Ref. 144 shown in Figure 3.15(b). Overall, this suggests the strength of the PA peak, and the degree to which it is blue shifted from the PB peak Δ, may be used as qualitative measures of the charge transfer and charge carrier load within SWNT systems.

Unfortunately, this still does not explain, why the blended P3HT:PCBM:SWNT sample has a more pronounced PA peak, since actually we would expect the opposite considering the amount of charge carriers, that is, the amount of hole, on the SWNT.

Comparing the calculated change in absorbance for (6,5) and (7,5) SWNTs in Figure 3.20, we find the (7,5) SWNT exhibits a less pronounced PA peak than the (6,5) SWNT for a single exciton, a negative trion, and a pair of excitons. In each case, the (7,5) SWNT excited state calculation gave a smaller gap widening Δ than the (6,5) SWNT. More importantly, the (7,5) SWNT PA peak overlaps with the PB peak of the (6,5) SWNT. This suggests that for a mixture of (6,5) and (7,5) SWNTs, a PA peak will only be visible when excited electrons remain on the (6,5) SWNT.

3.3.10   Influence of Photobleach Peak Width

It was already shown that the intensity and visibility of a PA peak decreases, if the broadening is too high[140]. To see what happens with the width and the shape of the peak for different broadenings, we modeled the SWNT sample spectrum by combining the calculated (6,5) and (7,5) SWNT transient spectra for various broadenings Γ.

In Figure 3.21 the combined (6,5) and (7,5) SWNT differential transmission spectra for peak widths of 0.05, 0.1, and 0.2 eV for the ground state and excited state absorbance are shown. A peak width of 0.05 eV for the independent tube absorbances is in good agreement with the peak width of the transient spectrum of Ref. 144 (blue). A peak width of 0.05 eV is also consistent with the absorption FWHM of Ref. 145, shown in Figures 3.15(a). However, in comparison to the spectrum of our SWNT sample, the combined transient spectrum has a much smaller peak width and is shifted to higher energy. This suggests that the SWNT sample shows a significant contribution due to (7,5) SWNTs. Furthermore, the transient spectrum of Ref. 144 shows a clear asymmetry due to the reduction of the peak at the higher energy end, consistent with our LDR-TDDFT-RPA calculations. This asymmetry becomes less pronounced the greater the broadening of the transitions. A peak width of 0.2 eV results in a spectrum similar to our SWNT sample measurements. This is also consistent with the absorption FWHM of our SWNT mixture shown in Figure 3.15(a).

A broader peak width for the SWNT and blended P3HT:PCBM:SWNT samples compared to those in the literature[144,145,236] might be due to having (6,5) and (7,5) SWNT mixture. Exciton transfer from the (6,5) to the (7,5) SWNT may be expected to occur, leading to electron-hole trapping on the (7,5) SWNT. Already, a 20% impurification can cause a decrease in power conversion efficiency (PCE) of an OPV by more than 30 times due to electron-hole trapping[74]. However, the peak width of the blended sample is significantly narrower than that of the SWNT system, as seen in Figure 3.15(a). The calculated energy differences between the excited (triplet) and ground states of the (6,5) SWNT and the bulk PT:PCBM:SWNT system suggest that an exciton within the bulk is more stable by about 0.08 eV. A potential source for the increased stability, and hence exciton lifetime, for the bulk system is electron and hole delocalization. This might explain the smaller width of the blended P3HT:PCBM:SWNT absorbance and resulting increase in visibility of the PA peak.
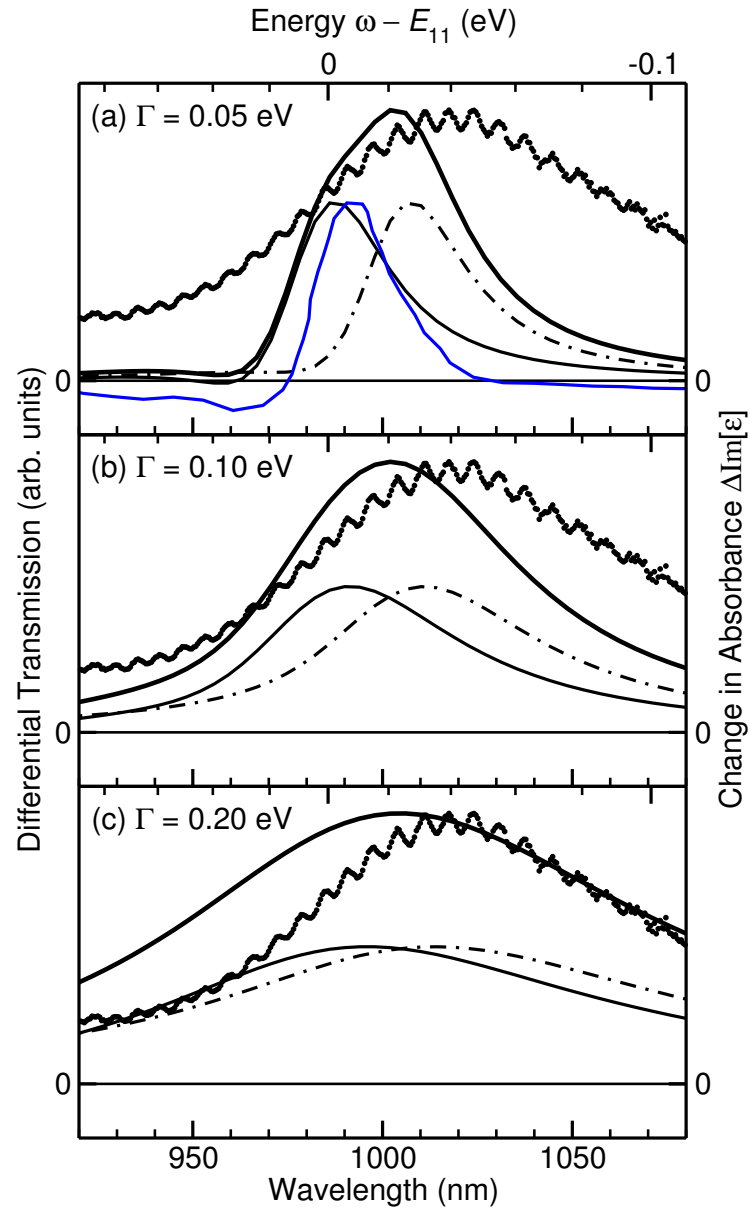
Figure 3.21: LDR-TDDFT-RPA change in absorbance between the ground and excited state for a (6,5) SWNT (solid thin lines), (7,5) SWNT (dash-dotted lines), and their normalized sum (solid thick lines) for broadenings Γ of (a) 50 meV, (b) 100 meV, and (c) 200 meV versus wavelength in nm and energy in eV relative to the E_{11} transition. Normalized differential transmission $\Delta T/T$ for our SWNT sample (black dots) and from Ref. 144 (blue) for a pump-probe delay of 0.2 ps also provided.

3.4   Modelling Transport Across Heterojunctions[*]

In this study, we carry out DFT calculations of the excited state formation energy, charge transfer, and zero-bias conductance of prototypical donor–acceptor bulk heterojunctions [69–71,74–78,88,97,98,239–241] in the singlet ground state and triplet excited state. For the donor molecule we employ the prototypical photoactive polymers: polythiophene (PT) [242] and poly(3-methylthiophene-2,5-diyl) (P3MT) [243]. For the acceptor molecule we compare fullerene (C_{60}) chains with semiconducting (6,4), (6,5), and (10,5) SWNTs, whose band gaps range between 1 and 1.4 eV [244]. These systems exhibit only a minor structural relaxation in the triplet excited state (<25 meV). This justifies our neglect of molecular vibration as a first approximation, [245] as done in previous studies of photovoltaic efficiencies. [246–248]

We model the excited state formation energy using the total energy difference between the triplet excited state and the singlet ground state from DFT. To obtain the charge transfer from donor to acceptor in the bulk heterojunction we perform a simplified Bader analysis [220] of the DFT all-electron density. Finally, we calculate the Landauer-Bütticker conductance of electron and hole charge carriers from donor to acceptor across the bulk heterojunction based on the DFT tight-binding Hamiltonians using a multiterminal implementation [162] of the non-equilibrium Green's function (NEGF) method [163–166]. In this way, we obtain the conductance from the isolated polymer, through the polymer–SWNT or polymer–C_{60} heterojunction, and out the SWNT or C_{60} chain, in the quantum coherent regime. Our use of the NEGF method for calculating the conductance across polymer–SWNT and polymer–C_{60} heterojunctions is justified by the ballistic transport, long coherence length, and high thermal conductivity of SWNTs [15,162,224,249,250], and the dominance of tunneling in transport processes across C_{60} chains. This method provides a more sophisticated description of the transport processes, and internal quantum efficiency (IQE) of the device, than previous studies employing the Newns-Anderson model. [246–248]

3.4.1   Computational Details

All DFT calculations were performed with LCAOs and the PAW implementation of the GPAW code [125,126,196], within the generalized gradient approximation (GGA) PBE [184] for the xc-functional. We employed a DZP LCAO basis set for representing the density, wavefunctions, and tight-binding Hamiltonian, which yields transmission functions in quantitative agreement ($\Delta < 50$ meV) with plane-wave codes and maximally localized Wannier functions [251]. All calculations employed a room temperature Fermi filling ($k_B T \approx 25$ meV), with total energies extrapolated to $T \to 0$ K, i.e., excluding the electronic entropy contribution to the free energy $-ST$. In this was we avoided an unrealistic smearing of the excited electron and hole in the triplet excited state calculations. We included two thirds of the number of electrons ($\frac{2}{3} N_e$) many bands within the calculations. This has been shown to be sufficient to converge the first $\pi \to \pi^*$ transitions of graphene [232] and SWNT/polymer hybrid systems [252], and the optical spectra of polymers and oligomers [121] in the RPA.

Structural optimization was performed within the ASE [230], until a maximum force below 0.05 eV/Å was obtained. We employed more than 5 Å of vacuum to the cell boundaries orthogonal to the C_{60} chain, (6,4), (6,5), (10,5) SWNTs, PT, P3MT, and P3HT, and obtained the optimized unit cells parameters along their axes $L_{\parallel} =$ 18.811, 40.915, 11.348, 7.867, 7.846, and 7.797 Å, respectively. Here, PT, P3MT, and P3HT are modeled using two thiophene, 3-methylthiophene, and 3-hexylthiophene units, respectively, in *s*-trans configuration. To sample the Brillouin zone, we included 3 **k**-points along the axis of PT, P3MT, P3HT, (6,4) SWNT, and (10,5) SWNT and 1
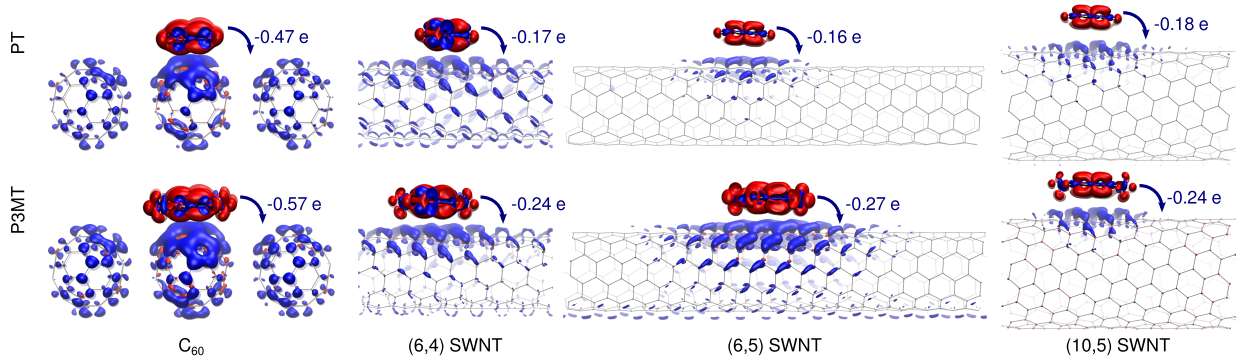
Figure 3.22: Electron (blue) and hole (red) densities at isosurface values of $\pm 1e/\mathrm{nm}^3$ from donor (PT or P3MT) to acceptor (C_{60} chain, (6,4), (6,5), or (10,5) SWNTs) from the DFT total charge density difference $\rho(\mathbf{r})$ between the excited triplet ($\uparrow\uparrow$) and singlet ($\uparrow\downarrow$) ground state.

k-point along the axis of the (6,5) SWNT.

The polymer–C_{60} junctions were modeled by aligning 10 thiophene/3-methylthiophene units orthogonal to a chain of three C_{60} molecules, and fully relaxing the resulting structure, shown in Figure 3.22. The polymer–SWNT junctions were modeled by aligning 6 thiophene/3-methylthiophene units for the smaller (6,4) and (6,5) SWNTs and 8 thiophene/3-methylthiophene units for the (10,5) SWNT orthogonal to the tube which was repeated once along its axis, and performing single-point calculations for the resulting configurations shown in Figure 3.22. This repetition of the thiophene/3-methylthiophene units makes a single **k**-point sampling along the polymer axis sufficient for describing the Brillouin zone.

By orienting the polymer and SWNT orthogonal to each other, this configuration describes the limit of a minimal polymer–SWNT overlap. In fact, by orienting diagonally across the SWNT axis a ten thiophene unit oligomer, which should provide a reasonable description of PT[121], one obtains a greater charge transfer and stronger hybridization between the polymer and SWNT[252].

For the polymer–SWNT junctions, the intermolecular distances were fixed between one carbon atom located at the centered C–C single bond of the polymer and a carbon atom of the tube, which were both aligned in the axis orthogonal to the tube and the polymer axis as shown in Figure 3.22. The alignment was achieved by shifting the polymer along the tube axis. This chosen intermolecular C–C distance is 3.35 for PT and 3.39 Å for P3MT. We slightly increased the P3MT intermolecular distance to reduce the repulsive forces from the hydrogen atoms of the methyl group. Both minimum distances employed are consistent with the interlayer distance of MWNT and graphite[235], of ~ 3.4 Å.

We performed DFT calculations for each system in both the singlet ground state ($\uparrow\downarrow$) and triplet excited state ($\uparrow\uparrow$). The triplet excited state calculations were performed by fixing the total magnetic moment μ of the system, and using separate Fermi levels for the spin majority and minority channels, $\varepsilon_F^\uparrow$ and $\varepsilon_F^\downarrow$, respectively. The Fermi levels associated with electron ε_F^e and hole ε_F^h charge carriers are then simply $\varepsilon_F^\uparrow$ and $\varepsilon_F^\downarrow$, respectively. For the singlet ground state calculations, ε_F^e is approximately the CBM $\varepsilon_{\mathrm{CBM}}$, while ε_F^h is approximately the VBM $\varepsilon_{\mathrm{VBM}}$.

The charge densities associated with the excited electron $\rho_e(\mathbf{r})$ and hole $\rho_h(\mathbf{r})$ in the triplet state are the negative and positive regions, respectively, of the all-electron charge density difference between that of the triplet excited state ($\uparrow\uparrow$) and singlet ground state ($\uparrow\downarrow$), i.e., $\Delta\rho(\mathbf{r}) = \rho_{\uparrow\uparrow}(\mathbf{r}) - \rho_{\uparrow\downarrow}(\mathbf{r})$.

To quantify the charge transfer from donor to acceptor, we perform a simplified Bader analysis[220] of the all-electron charge density in the singlet ground state $\rho_{\uparrow\downarrow}(\mathbf{r})$ and triplet excited state $\rho_{\uparrow\uparrow}(\mathbf{r})$. We begin by integrating the charge density over the plane A of the donor and acceptor axes to obtain the linear charge density

$$\lambda(z) = \iint_A \rho(r, \varphi, z) r d\varphi dr. \tag{3.2}$$

We then partition $\lambda(z)$ at its minimum $z_{\min}$ in between the polymer and C_{60} chain or SWNT. The charge transfer from donor to acceptor is then

$$Q = \int_0^{z_{\min}} \lambda(z) dz + e N_e^{\mathrm{acc}}, \tag{3.3}$$

where N_e^{acc} is the total number of electrons on the isolated acceptor molecule.

We employ a similar partitioning to assign a KS orbital $\psi(\mathbf{r})$ to the donor or acceptor molecule of the bulk heterojunction. The fraction of the nth KS orbital $\psi_n(\mathbf{r})$ on the acceptor molecule is then

$$\int_0^{z_{\min}} \iint_A |\psi_n(r, \varphi, z)|^2 r d\varphi dr dz. \tag{3.4}$$

The periodic DFT Hamiltonian and overlap matrices in the LCAO basis, $\mathcal{H}$ and $\mathcal{S}$, are employed within the NEGF formalism to calculate the Landauer-Bütticker conductance for a multiterminal configuration[162,164,166]. To do so, one must first remove overlap elements between atomic sites separated by more than half the length of the unit cell along the transmission direction, i.e., $\frac{1}{2}L_{\parallel}$, to obtain non-periodic Hamiltonian and overlap matrices H and S.

The coupling matrix to the semi-infinite leads V for the SWNTs is obtained by repeating the periodic DFT Hamiltonian matrix for the isolated SWNT

$$\mathcal{H}_{2\times 2} = \begin{pmatrix} H & (\mathcal{H} - H)^{\dagger} \\ \mathcal{H} - H & H \end{pmatrix}, \tag{3.5}$$

and removing overlap elements between atomic sites separated by more than $L_{\parallel}$, yielding the non-periodic Hamiltonian for semi-infinite lead α

$$H_{\alpha} = \begin{pmatrix} H & V \\ V^{\dagger} & H \end{pmatrix}. \tag{3.6}$$

This is reasonable for the SWNTs considered herein, for which $L_{\parallel} \gtrsim 20$ Å. In this way we avoid performing a DFT calculation with a repeated unit cell to obtain the Hamiltonian of the principle layer, H, which only couples to the next principle layer through the coupling matrix V. We then align the semi-infinite lead Hamiltonian H_{α} to the non-periodic DFT Hamiltonian for the bulk heterojunction using the first onsite energy of the same SWNT carbon atom at the cell boundary. This is unnecessary for PT, P3MT, and C_{60} as their lead Hamiltonians are extracted directly from the bulk heterojunction Hamiltonian. In these cases two thiophene units, two 3-methylthiophene units, and a C_{60} molecule comprise a principle layer, with couplings to the next nearest layer numerically zero.

The Hamiltonian matrix for the bulk heterojunction central region, H_C, is then generated by augmenting the non-periodic DFT Hamiltonian for the junction with the principle layer Hamiltonians H and coupling matrices V of the semi-infinite SWNT leads. The same procedure is employed to obtain the overlap matrix for the bulk heterojunction central region, S_C.

Following the multiterminal NEGF procedure described in Ref. 162, the zero-bias conductance at the Fermi level ε_{F} is $G = G_0 \mathrm{Tr}[\mathcal{G}_C \Gamma_{in} \mathcal{G}_C^{\dagger} \Gamma_{out}]|_{\varepsilon = \varepsilon_{\mathrm{F}}}$, where $G_0 = 2e^2/h$ is the quantum of conductance, $G_C(\varepsilon)$ is the Green's

Table 3.1: KS Band Gaps $E_{\mathrm{gap}}^{\mathrm{KS}}$, Photoluminescence E_{11} Transitions, and Triplet Excited State Formation Energy $E_f(\uparrow\uparrow)$ in Electronvolts of Acceptors (C_{60} chain, (6,4), (6,5), and (10,5) SWNTs) Isolated (—) and in Heterojunctions with a Donor (PT or P3MT)

species	$E_{\mathrm{gap}}^{\mathrm{KS}}$	E_{11}		$E_f(\uparrow\uparrow)$	
acceptor $\diagdown$ donor	—	—	—	PT	P3MT
C_{60} chain	1.46	1.9^a	1.508	0.842	0.622
(6,4) SWNT	1.08	1.420^b	1.101	0.967	0.843
(6,5) SWNT	0.92	1.272^b	0.853	0.804	0.689
(10,5) SWNT	0.74	0.992^b	0.858	0.712	0.626

^{a}Ref. 253, ^{b}Ref. 244.

function of the bulk heterojunction central region, and $\Gamma_{in/out}$ is the coupling to the semi-infinite input and output leads. The four-terminal conductance across the bulk heterojunction from donor to acceptor is then obtained when the input lead is that of a semi-infinite polymer, and the output lead is that of a semi-infinite C_{60} chain or SWNT.

The conductance of electron and hole charge carriers is then obtained by simply evaluating the transmission at their associated Fermi levels ε_F^e and ε_F^h, respectively. However, to understand the origin of differences in conductivity between the various donor–acceptor bulk heterojunctions considered herein, we shall find it useful to also consider the transmission within an energy window around the acceptor's VBM and CBM. In this way we may differentiate between differences in conductivity owing to an improved level alignment between donor and acceptor, an increased overlap of their levels, or a greater number of available transmission channels.

3.4.2 Energy Gaps and Band Gaps

To quantify the differences in electronic properties amongst the donors (PT, P3MT, and P3HT) and acceptors (C_{60} chain, (6,4), (6,5), and (10,5) SWNTs), we first consider the energy gaps for the isolated polymers and the band gaps of the isolated fullerene chain and SWNTs. Amongst the three functionalized thiophene polymers considered, both the calculated KS energy gaps and those measured via photoluminesence [240,242,243] differ by less than 50 meV, with the largest difference from PT occurring with the first methyl functionalization group (P3MT). For this reason, along with the accompanying reduction of computational effort, we shall restrict consideration from hereon to PT and P3MT as donors.

The acceptors considered have been intentionally chosen to provide a range of electronic band gaps, as shown in Table 3.1, from 1 eV for the (10,5) SWNT to 1.9 eV for the C_{60} chain. In each case, the calculated KS band gaps differ from the first E_{11} transition measured in photoluminescence (PL) experiments [244,253] by about 25%. This is consistent with previous results, and may be addressed through many-body GW corrections to the self energy [254–256]. However, for our purposes, it is more relevant to note that the difference is rather systematic amongst the carbon-based materials considered herein.

3.4.3   Triplet Formation Energy

A more reliable descriptor for differences in exciton binding between bulk heterojunctions is the triplet excited state formation energy $E_f(\uparrow\uparrow)$, provided in Table 3.1. This is obtained from the total energy difference between a system in the triplet excited state and the singlet ground state, i.e., $E_f(\uparrow\uparrow) = E(\uparrow\uparrow) - E(\uparrow\downarrow)$. Since $E_f(\uparrow\uparrow)$ depends only on DFT total energies, and not on KS eigenvalues, this quantity is in principle exact up to the approximation for the xc-functional.

Comparing the measured E_{11} transition energy and the calculated triplet formation energy $E_f(\uparrow\uparrow)$ for the isolated C_{60} chain and (6,5) SWNT, we find their difference is ~ 0.4 eV. This is consistent with the measured singlet exciton binding energy in SWNTs[48,63–66]. Although differences between the excited singlet and triplet states may occur, this demonstrates that the triplet excited state provides a reasonable approximation to the singlet excited state for fullerenes and SWNTs. For the (6,4) SWNT, we obtain a somewhat smaller energy difference (0.3 eV), while for the (10,5) SWNT it is significantly reduced to 0.1 eV. The latter is related to the reduction of the E_{11} transition energy for the (10,5) SWNT, while the $E_f(\uparrow\uparrow)$ is unchanged relative to the (6,5) SWNT. Altogether, this is indicative of a strong exciton binding in the isolated C_{60} chain, (6,4) SWNT, and (6,5) SWNT, with a much weaker exciton binding in the (10,5) SWNT. This suggests charge separation for isolated SWNTs may be easier for those with a smaller band gap.

To compare performance between different acceptors in bulk heterojunctions, it is more relevant to compare the difference between the triplet formation energy of the acceptor in the bulk heterojunction and in isolation. For a type II bulk heterojunction, a lower triplet formation energy in the bulk heterojunction suggests the hole is transferred to the donor. From Table 3.1 we see that $E_f(\uparrow\uparrow)$ is reduced for all the acceptors studied when in the bulk heterojunction. Further, the triplet formation energy is in all cases lower for the P3MT bulk heterojunction than the PT bulk heterojunction. We also clearly see that the C_{60} chain in the triplet state is significantly more stabilized upon inclusion in the PT or P3MT bulk heterojunction compared to the SWNTs. There, $E_f(\uparrow\uparrow)$ is stabilized by about 0.1 eV upon inclusion in a PT bulk heterojunction, and a further 0.1 eV for the P3MT bulk heterojunction, for all three SWNTs studied. Qualitatively, this suggests a significantly greater electron-hole separation for the C_{60} chain compared to the SWNTs, which should all be rather similar, with P3MT bulk heterojunctions having a more facile electron-hole separation than PT bulk heterojunctions.

3.4.4   Donor to Acceptor Charge Transfer

Alternatively, we may describe the degree of electron-hole separation directly by quantifying the charge transfer in the bulk heterojunction. This is obtained by partitioning the DFT all-electron density between the donor and acceptor species in the bulk heterojunction via a simplified Bader analysis. The charge transfer from donor to acceptor for each bulk heterojunction in the triplet excited state, singlet ground state, and their difference, is provided in Table 3.2.

From Table 3.2 we observe the following trends in the charge transfer: (1) it is always from donor to acceptor, (2) it is always more for P3MT than PT bulk heterojunctions by about -0.1 e, (3) for SWNTs it is always about $-\frac{1}{4}e$ for P3MT bulk heterojunctions and $-\frac{1}{6}e$ for PT bulk heterojunctions, and (4) it is significantly greater $(-\frac{1}{2}e)$ for C_{60} chains. All four findings are consistent with our previously mentioned expectations based on the triplet excited state formation energy.

To determine the origin of these trends in the bulk heterojunctions' charge transfer, it is useful to consider the

Table 3.2: CT in e from Donor (PT or P3MT) to Acceptor (C_{60} chain, (6,4), (6,5), or (10,5) SWNTs) for the Singlet Ground State ($\uparrow\downarrow$), the Triplet Excited State ($\uparrow\uparrow$), and their Difference ($\uparrow\uparrow - \uparrow\downarrow$)

donor	acceptor	$\uparrow\downarrow$	$\uparrow\uparrow$	$\uparrow\uparrow - \uparrow\downarrow$
PT	C_{60} chain	−0.01	−0.48	−0.47
P3MT	C_{60} chain	−0.04	−0.61	−0.57
PT	(6,4) SWNT	−0.05	−0.22	−0.17
P3MT	(6,4) SWNT	−0.10	−0.34	−0.24
PT	(6,5) SWNT	−0.16	−0.31	−0.16
P3MT	(6,5) SWNT	−0.23	−0.50	−0.27
PT	(10,5) SWNT	−0.10	−0.29	−0.18
P3MT	(10,5) SWNT	−0.19	−0.43	−0.24

spatial distribution of the difference in all electron density between triplet excited state and singlet ground state shown in Figure 3.22. For each bulk heterojunction studied, the hole density is mostly localized on the π bonding HOMO of PT or P3MT, with the electron density on π anti-bonding levels of the C_{60} chain or SWNT. Comparing the PT and P3MT bulk heterojunctions, we notice that the hole density clearly extends onto the methyl groups of P3MT. We expect this spatial delocalization of the hole density onto the methyl groups of P3MT makes hole transfer easier in P3MT than PT bulk heterojunctions. For the (6,4), (6,5) and (10,5) SWNT bulk heterojunctions, the electron and hole densities shown in Figure 3.22 are rather consistent, with the electron density on the upper surface of the SWNT neighbouring the PT or P3MT. On the other hand, for the C_{60} chain, the electron density is delocalized over the entire surface of all three fullerenes. This suggests the greater charge transfer onto the C_{60} chains compared to the SWNTs may have a geometrical origin.

3.4.5   Conductance from Donor to Acceptor

However, although these results clearly demonstrate a charge transfer from donor to acceptor, it remains unclear whether the excited electron and hole are truly free charge carriers, or remain bound at the donor–acceptor interface. To address this issue, we provide the zero-bias conductance at the energy of the excited electron ε_F^e and hole ε_F^h in the singlet ground state and triplet excited state in Table 3.3.

Note that these conductances are across a single polymer–fullerene or polymer–SWNT junction. This is because within the NEGF formalism, the fullerene chain, SWNT, and polymer are all modeled as semi-infinite leads. For this reason, the conductances provided in Table 3.3 may be considered to be per absorbed photon. Further, as there is only a single PT or P3MT band for this energy range through which current may flow, the quantum of conductance, $G_0 = 2e^2/h$, provides a theoretical upper bound on the conductance across the junction.

Overall, the conductances quoted in Table 3.3 vary by over six orders of magnitude, from $G_0 \times 10^{-7}$ to $0.1G_0$. Particularly impressive is the PT–(6,4) SWNT junction, with conductances of 9% and 5% of G_0 for free hole and electron carriers, respectively. While the (6,4) SWNT junctions clearly provide the highest conductivity in the triplet excited state, the P3MT–C_{60} chain junction is clearly the most active in the singlet ground state. Comparing the conductance for the junction in the singlet ground state and the triplet excited state, we find the conductance is generally significantly greater when the system is in the triplet excited state. This suggests that the level hybridization related to the charge transfer observed in Figure 3.22 facilitates tunnelling across the donor–acceptor

Table 3.3: Conductance G in $G_0 \times 10^{-3}$ from Donor (PT or P3MT) to Acceptor (C$_{60}$ chain, (6,4), (6,5), or (10,5) SWNTs) for Hole Carriers at ε_F^h and Electron Carriers at ε_F^e in the Singlet Ground State ($\uparrow\downarrow$) and the Triplet Excited State ($\uparrow\uparrow$)

		hole carriers		electron carriers	
donor	acceptor	$\uparrow\downarrow$	$\uparrow\uparrow$	$\uparrow\downarrow$	$\uparrow\uparrow$
PT	C$_{60}$ chain	0.0007	0.003	0.003	0.02
P3MT	C$_{60}$ chain	0.3	0.0007	0.09	0.6
PT	(6,4) SWNT	0.05	88	0.02	46
P3MT	(6,4) SWNT	0.0005	1	0.01	16
PT	(6,5) SWNT	0.0007	0.007	0.02	0.005
P3MT	(6,5) SWNT	0.0002	0.01	0.0003	0.004
PT	(10,5) SWNT	0.01	0.01	0.002	0.003
P3MT	(10,5) SWNT	0.0003	0.04	0.0002	0.002

gap. However, the opposite is true for the P3MT–C$_{60}$ chain junction. We also find the (6,5) and (10,5) SWNTs, with their smaller band gaps, have quite low conductivities. This is consistent with recent experimental findings, which showed P3HT:PCBM:(6,5) SWNT bulk heterojunctions perform rather poorly[88].

To provide insight into the reasons behind the great variability in the free carrier conductance provided in Table 3.3, and the origin of the high conductance across the (6,4) SWNT junctions in the triplet excited state, we plot the transmission function $\mathcal{T}(\varepsilon) = \text{Tr}[\mathcal{G}_C \Gamma_{in} \mathcal{G}_C^\dagger \Gamma_{out}]$ near the VBM and CBM for the polymer–C$_{60}$ and polymer–SWNT junctions in Figures 3.23 and 3.24, respectively.

For the polymer–C$_{60}$ junction, depicted schematically as an inset in Figure 3.23, we provide the conductance through the polymers (PT→PT and P3MT→P3MT), along the C$_{60}$ chain (C$_{60}$ →C$_{60}$), and across the junction (PT→C$_{60}$ and P3MT→C$_{60}$). The transmission along the polymers is simply G_0 for energies below the HOMO, zero within the energy gap, and G_0 above the LUMO. This amounts to a simple counting of the number of bands below the VBM and above the CBM.

In the singlet ground state, the HOMO of PT/P3MT is pinned to the LUMO of C$_{60}$ at the Fermi level, while in the triplet excited state, the LUMO of PT/P3MT becomes pinned to the LUMO of C$_{60}$ at the Fermi level of the excited electron ε_F^e. This means any differences in band gap between PT and P3MT do not play an important role for the polymer–fullerene bulk heterojunctions, as the donor HOMO and LUMO are pinned to the LUMO of the acceptor in the ground and excited state, respectively.

Conduction through the C$_{60}$ chain is rather different. It instead exhibits narrow plateaus centered on the HOMO and LUMO of the C$_{60}$ chain. As a result, conduction across the polymer–fullerene junction is limited to these narrow plateaus where the C$_{60}$ chain is conductive. It is this limitation in the conductivity of C$_{60}$ chains, which limits their effectiveness within OPV bulk heterojunctions, and motivates their replacement with SWNTs[240].

Unlike the C$_{60}$ chain, the transmission through semiconducting SWNTs exhibits broad plateaus, and is typically $2G_0$ below the VBM, zero within the band gap, and $2G_0$ above the VBM. As was this case for transmission through the polymers, this amounts to a simple counting of the number of bands below and above the VBM and CBM, respectively. As the transmission through the polymers and SWNTs is rather trivial, up to scattering due to transmission across the junction, it has been omitted in Figure 3.24. Instead, we plot the HOMO, SOMO, SUMO,
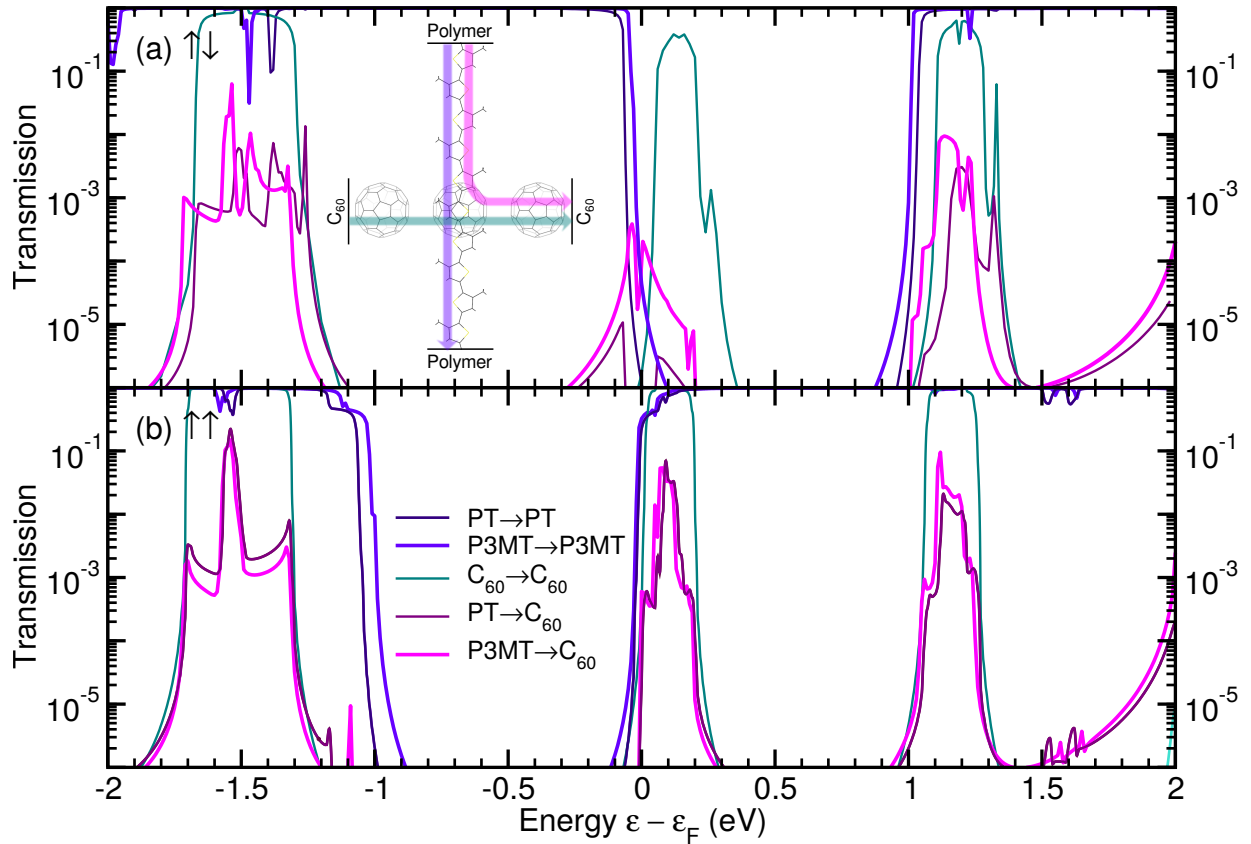
Figure 3.23: Transmission across a polymer–C_{60} junction, depicted schematically as an inset, versus energy ε in eV relative to the Fermi level ε_F in the (a) singlet ground state ($\uparrow\downarrow$) and (b) triplet excited state ($\uparrow\uparrow$), for PT–C_{60} (thin dark lines) and P3MT–C_{60} (thick light lines).

and LUMO energies below/above which the transmission from PT→PT and P3MT→P3MT is G_0.

For polymer–SWNT junctions, we find the conductance is intimately related to the alignment of the SWNT/polymer HOMO and LUMO levels (*cf.* Figure 3.24). In fact, the conductance at ε_F^e and ε_F^h depends exponentially on the alignment of the SWNT and polymer HOMOs and LUMOs[257].

For the (6,4) SWNT, with a KS band gap a bit smaller than PT and P3MT, we find both the HOMO and LUMO levels of the polymer and SWNT are align in the triplet excited state. Although the resulting charge transfer is rather similar to the other SWNTs studied (*cf.* Table 3.2), the improvement in level alignment places ε_F^h and ε_F^e at or near the polymer HOMO and LUMO, respectively. This results in a very high conductivity across the polymer–(6,4) SWNT junctions in the triplet excited state (*cf.* Table 3.3). On the other hand, the level alignment for the (10,5) SWNT is the poorest of those considered, as the CBM of the nanotube is shifted down relative to the LUMO of the polymer as the band gap decreases.

In fact, if the transmission were measured above or below the polymer LUMO or HOMO, respectively, the conductance across all three polymer–SWNT junctions studied would be $> 1\%$ of G_0. This is not the case for the C_{60} chain, which is only conductive within a narrow range of the chain's HOMO and LUMO.
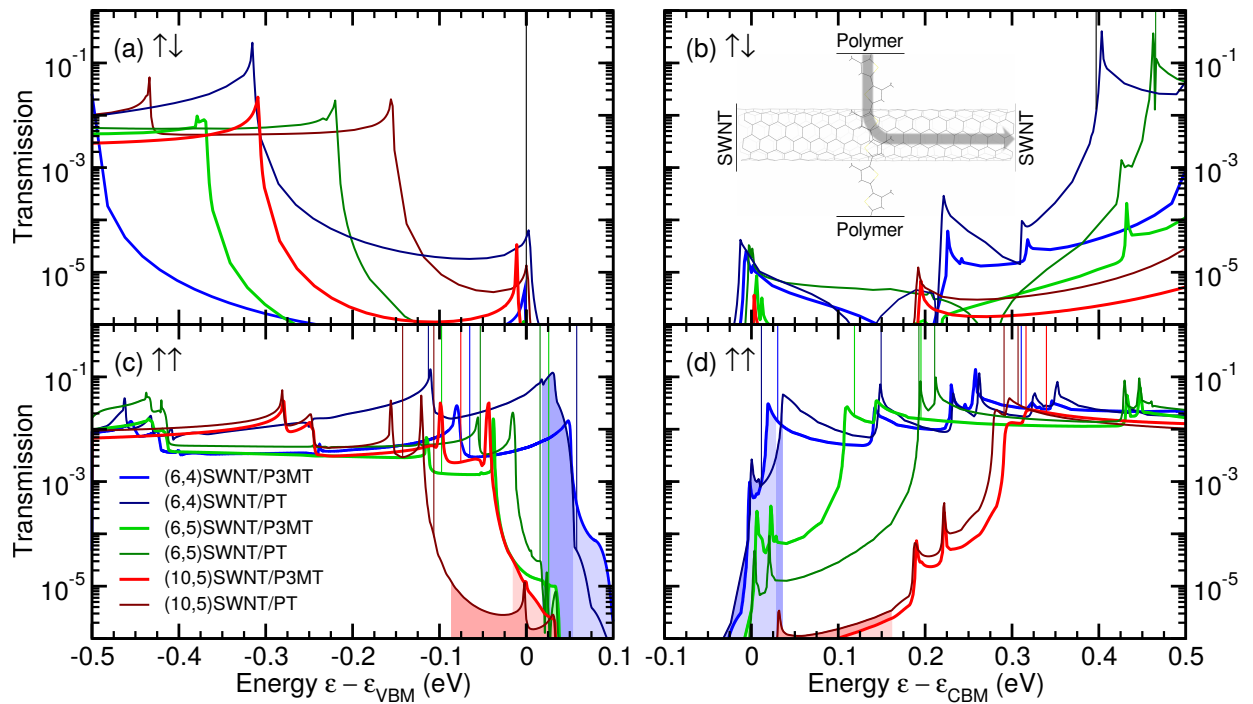
Figure 3.24: Transmission across a polymer–SWNT junction, depicted schematically as an inset, versus energy ε in eV of (a,c) the hole relative to the VBM ε_{VBM}, and (b,d) the electron relative to the CBM ε_{CBM} in the (a,b) singlet ground state ($\uparrow\downarrow$) and (c,d) triplet excited state ($\uparrow\uparrow$), with PT (thick light lines) and P3MT (thin dark lines) as donors and a (6,4) (blue), (6,5) (green), and (10,5) SWNT (red) as acceptors. DFT eigenenergies of the HOMO, SOMO, SUMO, and LUMO of P3MT/PT are marked by thin vertical lines. Filling in (c/d) denotes hole/electron charge carriers above/below the Fermi level of the VB/CB in the triplet excited state.

Essentially, the conductance across polymer–SWNT heterojunctions can be dramatically improved by a better alignment of the polymer's HOMO and LUMO levels with the SWNT's VBM and CBM, respectively. This may be accomplished using a SWNT with a larger band gap, e.g., a (6,4) SWNT. However, improving the level alignment too much may lead to a reduction of the electron and hole transfer.

Chapter 4

Conclusions & Outlook

In this work, we guided the reader through different aspects of modelling polymer–carbon nanotube heterojunctions and the electronic processes that occur upon photexcitation and during transport across the junction. In the beginning we discussed the possibility of modelling polymers from oligomers, which allows us to study the interactions at the interface of the polymer–SWNT heterojunction with less computational effort. In section 4.1 we will conclude from our results obtained from linear dielectric response (LDR) time-dependent density functional theory (TDDFT) within the random phase approximation (RPA) calculations that the copolymer of 9,9-dioctylfluorenyl-2,7-diyl and bipyridine (PFO-BPy) can be modelled by the monomer unit of the copolymer of pyridine, 9,9-dioctylfluorenyl-2,7-diyl and pyridine (Py-PFO-Py) with shortened side chains, since the optical properties within the polymer are reasonably well described by the monomer unit. Further, we will suggested possible studies on interactions at the monomer–SWNT interface.

We also were able to show that linear response (LR) TDDFT calculations on monomers can be used to identify the x, y, z contributions of the dipole oscillator strengths and thefore the transition dipole moments (TDMs) of transitions from the ground to excited state in the polymer unit spectrum. In section 4.2 we will argue that LR-TDDFT is a useful tool in combination with angle-dependent absorption spectroscopy to evaluate the supramolecular structure of polymer–single-walled carbon nanotube (SWNT) heterojunctions. From our combined results, that are the experimental PFO-BPy–SWNT angle-dependent absorption spectrum and the LR-TDDFT spectrum of the Py-PFO-Py unit, we can conclude that the PFO-BPy is aligned along the carbon nanotube's axis and not wrapped as initially thought. In addition, we will present planned experiments on other polymer–SWNT heterojunctions.

We discussed as well the transient absorption spectra of SWNTs and polymer:SWNT blends. The occurance of a photoinduced absorption (PA) peak in transient pump probe spectra of SWNT samples has motivated many hypotheses in the field. It is thought that the structure of this peak bears important information about the dynamical processes upon photoexcitation. In section 4.3, we will infer that we effectively modelled the PA peak in the transient spectra of SWNT samples using LDR-TDDFT-RPA. We will discuss the reason for the PA peak and that it could be used to evaluate different charge loadings of the SWNT samples. In addition, we will suggest further methods to model the singlet excited state more accurately.

Finally, we took a look at the performance of polymer–C_{60} and different polymer–SWNT heterojunctions in organic photovoltaics (OPVs) by calculating the Landauer-Bütticker conductance obtained using the non-equilibrium Green's function (NEGF) method. These results demonstrate the importance of considering the hybridization of

donor–acceptor levels in the excited state, and the resulting dependence of the conductivity on the level alignment, which we will explain in section 4.4. We will look at possible extensions of the NEGF description by including explicit time-dependence and the perturbation of the system. Finally, we will suggest polymers and nanotubes that may improve the efficiency of OPVs and the possible use of theoretical methods to predict materials with optimal level alignment and lower exciton binding energies.

4.1 Modelling Polymer–SWNT Heterojunctions

We have found that there is almost no red shift occurring while extending the π-system through the attachment of the Py-PFO-Py oligomer units. This suggests that conjugation of the π-system is broken due to the ortho conjugation of the bipyridine. As well, the electron and hole densities reveal that the exciton is only located on the Py-PFO-Py monomer unit in the polymer. On the other hand, the PFO-BPy monomer is electronically completely different from either the dimer or the trimer. By extending the PFO-BPy oligomers, the PFO-BPy system converges to the Py-PFO-Py system, albeit more slowly. We have also confirmed that the oligomer spectra converges to that of the infinitely long polymer chain using TDDFT within the RPA. We find that TDDFT-RPA underestimates the transition more than linear response TDDFT, and the TDDFT-RPA highest occupied molecular orbital (HOMO)-lowest unoccupied molecular orbital (LUMO) absorption peak coincides precisely with the density functional theory (DFT) HOMO-LUMO energy gap.

The small shift in the spectra between PFO-BPy and Py-PFO-Py systems indicates there is only a weak conjugation between the single monomer units. By breaking the conjugation through a rotation of the pyridine (Py)-Py bond in the dimer, the dimer only experiences a small blue shift relative to the monomer. This suggests that the shifts might also have other origins, such as the increasing molecular weight.

Additionally, we confirmed that there is no electronic influence of the octyl side chains in 9,9-dioctylfluorenyl-2,7-diyl (PFO), beyond the first ethyl group, as expected. This is consistent with previous studies of the polymer chain length's effect on the absorption properties of such polymers[233].

Overall, we find the Py-PFO-Py unit with shortened ethyl side chains describes the PFO-BPy polymer sufficiently well to be used when modelling electronic and optical absorption properties of a hybrid polymer-SWNT system. These results have important implications for the reliability of such simplified models for describing polymer-SWNT heterojunctions[258].

In another study we compared the adsorption enthalpies of Py-PFO-Py and derivatives on SWNTs by subtracting the ground-state energies of the isolated monomer unit and the SWNT from the ground-state of the Py-PFO-Py–SWNT heterojunction. We have found that the physisorption is quite strong, with around 1 electronvolt (eV) of energy. Unfortunately, comparing different monomer units and their adosrption behaviour emerged difficult because of several points (1) the van der Waals xc functional (vdW-DF) functional is very demanding for such huge systems, (2) small chemical changes, like the exchange of some atoms, have almost no influence on the energies considering that we look at a system with around 1000 atoms, (3) including the effect of the solvent is rather difficult, (4) a huge impact on the calculation of the adsorption enthalpy have the rotations of the 6-membered rings in the polymer unit. Polymers, whose ground-state structure is stronger twisted, show smaller adsorption enthalpies. This is due to fact that the polymer physisorbs more stable on the SWNT when being planar. Hence, different conformers need to be considered in such a study. The strength of the polymer twist might as well be the reason for the selective sorting of certain tube sizes. This is an important point, which needs to be studied further. As well, the electronic influence of

the physisorption on the SWNT can be evaluated by looking at the density of states of the SWNT with and without physisorbed polymer units. We plan to study the mechanism of polymer sorting further to get a better understanding of what influences the selectivity. Our results shall support the development of polymers that selectively sort tubes of the wished size/chirality.

4.2 Supramolecular Structure Evaluation of Polymer–SWNT Heterojunctions

From the polarized angle-dependent absorption spectrum of PFO-BPy sorted (6,5) SWNT samples that were embedded in a crystalline polystyrol matrix, we could deduce that the polymer absorption peak and the first excited state in SWNTs (E_{11}) and second excited state in SWNTs (E_{22}) transitions of the (6,5) SWNTs have the same angle dependence. This result suggest that in this sample the polymer PFO-BPy and the SWNTs have the same polarization.

Using LR-TDDFT calculations, we were able to extract a dipole strength direction resolved absorption spectrum of the Py-PFO-Py unit. The Py-PFO-Py unit is representative for the full PFO-BPy polymer as discussed in section 4.1. In the spectrum we see that the transition is perturbed by an electric field polarized along the *y* direction, that is, along the polymer's backbone. Comparing this result with the polarized angle-dependent spectrum, we are able to verify that in the experimental setup the polymer has to be aligned vertically, that is, in the *y* direction, when the sample is at 0°. Only in this position will the polymer absorb parallel polarized light as it does in the experiment.

A strongly wrapped polymer would show a helical-like structure and would therefore absorb light polarized along 45°, when the nanotubes are aligned vertically at 0°. In addition, the absorption would be significantly reduced, since 50% of the wrapped polymer would be aligned at 135°. Even though the reference sample of the PFO-BPy shows polarization in the same direction due to the stretching of the matrix, we can exclude that a strongly wrapped polymer would stretch out in the same way in the PFO-BPy sorted (6,5) SWNT sample. Moreover, it is unlikely that the polymer stretches out to account for a 1.7 times stronger absorption. In summary, all our combined results suggest that the compolymer PFO-BPy has to be aligned stretched out along the tube axis.

We have shown that polarized angle-dependent absorption spectroscopy in combination with LR-TDDFT is an efficent and dependable tool for identifying the supramolecular structure of polymer–SWNT heterojunctions. This result is of importance for the evaluation of the supramolecular structure of polymer–SWNT heterojunctions and further supports the understanding of the polymer selective dispersion of nanotubes.

Further projects are under discussion regarding the evaluation of the supramolecular structure of other polymer–SWNT heterojunctions. Specifically, we are interested in identifying how a polymer of 9,10-(N-octyl-2,5-pyrrolidin-dione)anthracene units* (shown in Figure 4.1 with ethyl side chain and hidroxy linkers) adsorbs on SWNTs. In order to achieve the optimal physisorption, the "clamp"-like structure of the antracene side (red) should adsorb orthogonal to the tube axis. We can see in Figure 4.1 that peaks in the experimental spectrum are in good agreement with the LR-TDDFT spectrum. In addition, all peaks show contributions to the average dipole strengths in different directions. This might be useful for deteriming the orientation of the "clamp" on the SWNT using polarized angle-dependent absorption spectroscopy.

---

*The experimental work shown in Figure 4.1 was performed by Ina Bodoky. The absorption spectrum was kindly provided in a private communication.
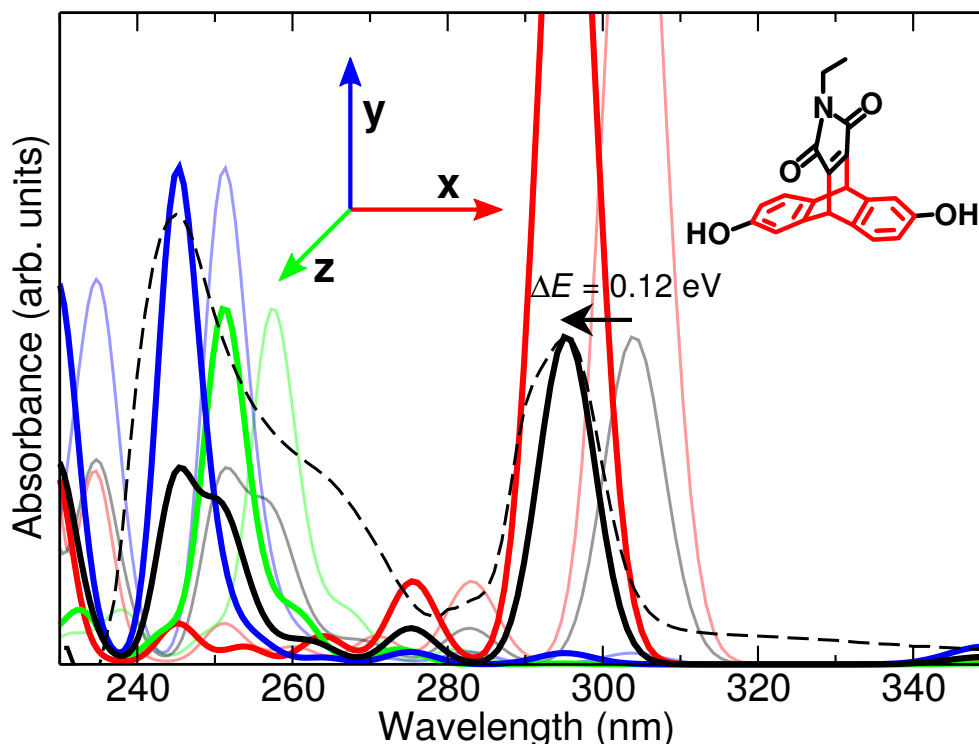
Figure 4.1: Comparison of the average (black) LR-TDDFT absorption spectrum (solid lines) of the 9,10-(N-ethyl-2,5-pyrrolidindione)-3,7-dihodroxy-anthracene, and dipole oscillator strength contributions in the *x* (red), *y* (blue), and *z* (green) directions, with the measured spectra of unit with octyl instead of ethyl side chains (black dashed line) before (light thin lines) and after (dark thick lines) applying a common energy shift of $\Delta E = 0.12$ eV. The molecular structure of the 9,10-(N-ethyl-2,5-pyrrolidindione)-3,7-dihodroxy-anthracene unit aligned in the *x*-direction is shown as an inset.

4.3 Modelling Transient Absorption Spectroscopy

Using LDR-TDDFT-RPA calculations of the ground and excited states of (6,5) and (7,5) SWNTs, we are able to qualitatively explain the measured differential transmission spectra of the probed lowest energy excited state, the E_{11} transition. Our results confirm that the observed PA peak is due to a blue shift Δ of the E_{11} transition after pumping. The PA peak is therefore an artifact of excitations within the spin channel, which experience a widening of the band gap after electron and hole stabilization within the other spin channel.

The intensity and the visibility of the PA peak depends on the charge carrier density, but mainly on the peak width. If the peak width is greater than the blue shift of the main absorption peak, the transient spectrum will be dominated by the photobleach (PB) peak[140]. Further, our SWNT sample contains a mixture of (6,5) and (7,5) SWNTs. This SWNT sample exhibits rather broad absorption peaks, approximately 4 times broader than previously measured (6,5) SWNT samples[144,145]. We suggest that this is related to having a mixture of SWNTs with similar energy gaps. The different types of SWNTs are causing an overlap of the peaks, but more importantly, the mixture enables an exciton transfer from the (6,5) to (7,5) SWNTs. This both shortens the exciton lifetime on the (6,5) SWNTs

and inhibits a widening of the band gap. As a result, the differential transmission spectrum of the (6,5) SWNT has almost no PA peak.

For the blended poly(3-hexylthiophene-2,5-diyl) (P3HT):phenyl-C_{61}-butyric acid methyl ester (PCBM):SWNT sample, the exciton is locally stabilized on the (6,5) SWNT due to the hole transfer to the P3HT. As a result, the PA peak intensity and position in the differential transmission spectra may be used as a qualitative measure of exciton density and charge transfer within SWNT systems.

These results are important for the understanding of the origin of the PA peak in pump-probe spectroscopy and will help to interpret the exciton dynamics within SWNT systems.

In future studies on transient spectra of extended system we may attempt to create better models and descriptions of the singlet excited states. We have already attempted to model the singlet excited state with the delta self-consistent field (ΔSCF) method, which adds the density of a specified orbital to the total density in each step of the self-consistency cycle. The extra charge is usually taken from the Fermi level to keep the system neutral. By creating a hole density in the SWNT's HOMO and adding a negative charge to the occupied states, we have obtained the unoccupied electronic Kohn-Sham (KS) densities, whereas putting an electron in the SWNT's LUMO and adding a positive charge to the occupied levels resulted in the occupied hole KS densities. However, we were unable to converge the band structure due to the many close lying, nearly degenerate KS levels present in the (6,5) SWNT. One might attempt to model the singlet excited state using equation-of-motion coupled cluster (EOM-CC), single excitation configuration interaction (CIS), or TDDFT. If we are able to find a way to model the excited states of extended systems, we would be able to simulate more reliable transient spectra, as well at that of higher energy excited states.

4.4 Modelling Conductance Across Heterojunctions

We have employed four descriptors: (1) the triplet state formation energy $E_f(\uparrow\uparrow)$, (2) the donor to acceptor charge transfer, (3) the conductance of free electron carriers $G(\varepsilon_F^e)$, and (4) the conductance at free hole carriers $G(\varepsilon_F^h)$, to assess the relative performance of OPV bulk heterojunctions with polythiophene (PT) and poly(3-methylthiophene-2,5-diyl) (P3MT) as acceptors, and C_{60} chains, (6,4), (6,5), and (10,5) SWNTs as acceptors. We find P3MT, with its larger band gap, and greater ability to absorb a hole, generally exhibits a greater charge transfer and conductance than PT. The C_{60} chain accepts significantly more charge ($\sim\frac{1}{2}e$) than the SWNTs ($\sim\frac{1}{4}e$), which are rather consistent for all the SWNTs considered. These results are also consistent with the calculated formation energies for the triplet excited state.

However, the conductance across the junctions via free hole and electron carriers differs by six orders of magnitude amongst the bulk heterojunctions considered here. In the singlet ground state the P3MT–C_{60} chain junction has the greatest conductivity of those considered (0.03% and 0.06% of G_0), while the PT–(6,4) SWNT junction shows a dramatic increase in conductivity in the triplet excited state (9% and 5%). This suggests by improving the level alignment of the polymer and SWNT through the use of larger band gap SWNTs, one may obtain a dramatic improvement in OPV efficiency.

Altogether, these results demonstrate the importance of considering the hybridization of donor–acceptor levels in the excited state, and the resulting dependence on level alignment of the conductivity. This dramatic dependence on the level alignment observed herein provides significant motivation for future studies including the dependence on the vibrational modes of the molecules[245], and more advanced quasiparticle calculations including anisotropic
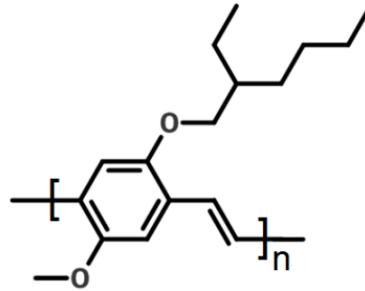
Figure 4.2: Molecular structure of poly[2-methoxy-5-(2-ethylhexyloxy)-1,4-phenylenevinylene] (MEH-PPV)

screening effects [259–263] in the polymer–SWNT level alignment. Furthermore, a reformulation of the NEGF method to describe photoinduced quantum transport is required to describe the optical absorption dependent photovoltaic efficiency of OPV devices. The techniques employed herein provide a road map for the computational design of OPV bulk heterojunctions *in silico*.

It is planned to extend the NEGF formalism to describe photoinduced quantum transport across a bulk heterojunction. This may be accomplished by introducing the screened vector potential of solar irradiation into the Hamiltonian as a coupling between initial and final absorption states.

Further, we suggest perfoming studies to find the optimal level alignment of SWNTs with poly[2-methoxy-5-(2-ethylhexyloxy)-1,4-phenylenevinylene] (MEH-PPV), as shown in Figure 4.2. This polymer is used for light emmiting diodes (LEDs) although its potential use in SWNT-based OPVs has received little attention [264,265] The interesting thing about poly(p-phenylene vinylene)s (PPVs) is that they can be functionalized differently, which results in different band gaps. The introduction of extended functional groups might as well lower the exciton binding energy due to more efficient electron/hole separation. In summary, MEH-PPVs or a polymer of a PPV derivative could result in a promising polymer for an optimal level alignment with SWNTs. This could be investigated via calculations of the Landauer-Bütticker conductance using the NEGF method.

4.5 Final Remarks

Thanks to our studies we were able to gain a deeper understanding of the electronic processes that occur upon photoexcitation within polymer–SWNT heterojunctions. We have successfully demonstrated that we can model experimental pump probe data of the lowest energy excited state in SWNT systems and in so doing facilitate their interpretation. Our results have shown that the photoinduced absorption in transient spectra can reveal the localization or delocalization of charges and therefore can be used to qualitatively compare charge transfer states and exciton binding in materials. In addition, we were able to provide an explanation for the low internal quantum efficiencies of SWNT-based OPVs. We found that improving their donor–acceptor level alignment increases the internal quantum efficiency by several orders of magnitude. In addition, we have shown that it is essential to include the energy levels of the excited state in order to properly describe the donor–acceptor level alignment. Our achievments pave the way for the use of theoretical tools to predict potential materials for the development of more efficient OPVs.

I thank the reader for his/her interest in this work on polymer–carbon nanotube heterojunctions and their use in organic photovoltaic applications. I hope it stimulates new ideas for future scientific work.

Appendix A

Power Conversion Efficiency

The power P in Watts of an organic photovoltaic (OPV) device is given by the equation $P = IV$, from which as well the maximum power P_{max} quadrant is obtained as shown in Figure A.1.[266] Although the amount of power is essential, the actual quality of a solar cell is defined by the fill factor (FF), which is the ratio of maximum power
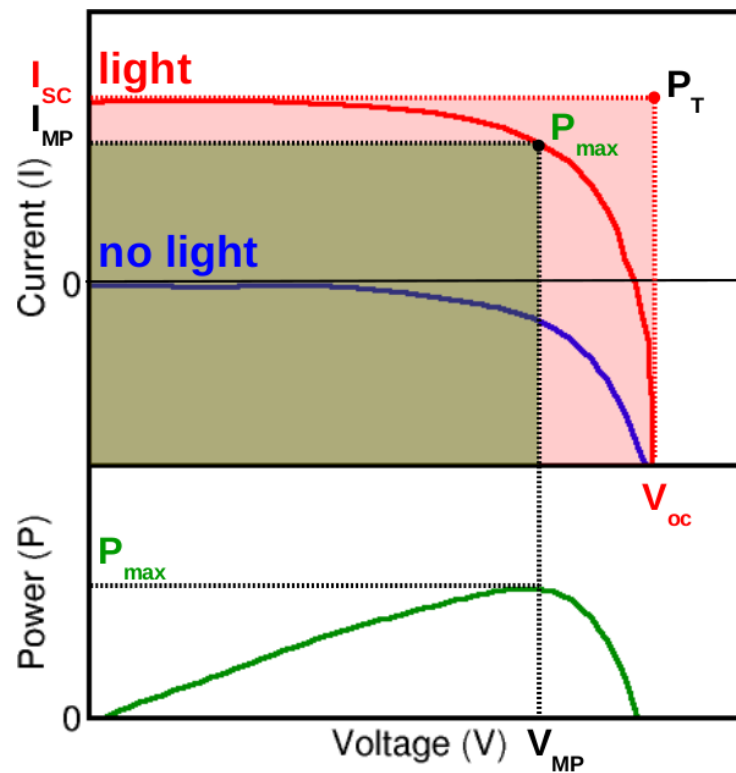
Figure A.1: Ideal $I - V$ sweep with maximum power P_{max} quadrant and theoretical power P_T quadrant.

P_{max} to the theoretical power P_T,

$$FF = \frac{P_{max}}{P_T} = \frac{I_{MP} \cdot V_{MP}}{I_{SC} \cdot V_{OC}}. \tag{A.1}$$

The larger the FF, the more ideal and square-like is the I-V sweep. This is normally hampered by the internal shunt and series resistances, which decrease the current respectively make the voltage drop. This has an impact on P_{max} and therefore on the power conversion efficiency (PCE) of the cell, which is given by

$$\text{PCE} = \frac{P_{out}}{P_{in}} \implies \text{PCE} = \frac{I_{SC} \cdot V_{OC} \cdot FF}{P_{in}}, \tag{A.2}$$

where P_{in} is the product of the irradiation of the incident light (W/m^2 or in suns $1000W/m^2$) and the surface area of the solar cell (m^2), and P_{out} is the power output of the device. This external efficiency includes optical losses from reflection and transmission.

In section 3.4, the internal quantum efficiency (IQE) is studied, which refers to the percentage of absorbed photons that are converted to electric current. Note that unlike the photovoltaic efficiency,[267] the IQE is independent of the device's optical absorption spectra, that is, the number of absorbed photons, as it is calculated per absorbed photon.[159]

Appendix B

LCAO TDDFT-RPA

The optical absorption spectra are obtained via linear response (LR) time-dependent density functional theory (TDDFT) within the random phase approximation (RPA)[119–121,207,232], from the imaginary part of the macroscopic dielectric function, $\text{Im}[\varepsilon(\mathbf{q}, \omega)]$, as $\|\mathbf{q}\| \to 0^+$.

In Figure B.1 we compare the TDDFT-RPA spectra obtained within the locally centered atomic orbital (LCAO) basis (violet), and after projecting onto a real space grid (blue). The latter was calculated using the TDDFT-RPA implementation within the GPAW code[125,126,196] described in refs 119, 120 and 232 including 79 $\mathbf{G}$ vectors.
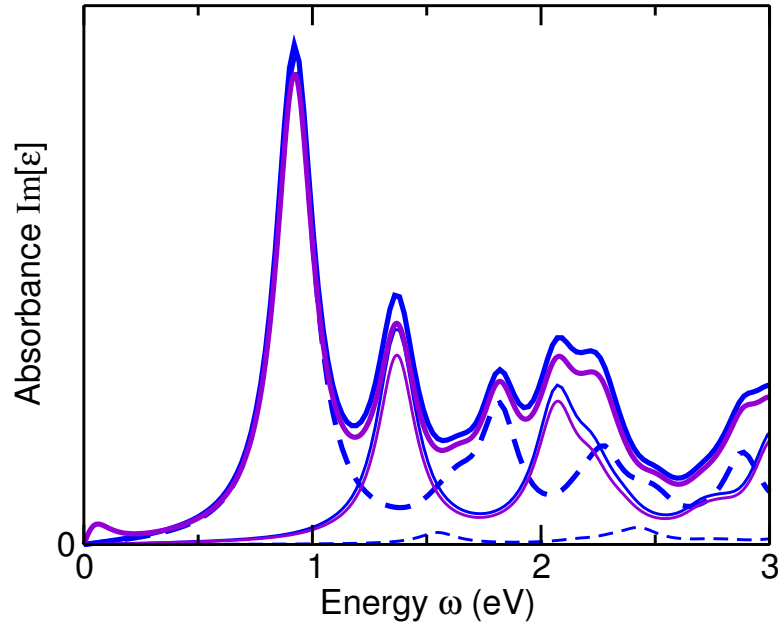
Figure B.1: TDDFT-RPA absorbance $\text{Im}[\varepsilon]$ of a (6,5) SWNT in the ground state versus energy in eV obtained from our LCAO implementation (violet) and a real space projection of the wavefunctions (blue) including (dashed) and neglecting (solid) LFEs. Total absorbance (thick lines) and absorbance for light polarized perpendicular to the SWNT axis (thin lines) are shown.

When LFEs are neglected, both codes agree up to a constant of proportionality. We attribute this difference to the projection of the LCAO basis functions onto the real space grid. When including LFEs, the absorbance perpendicular to the SWNT axis is greatly suppressed, while that along the axis is unchanged. However, this suppression of the perpendicular absorbance may be due to modelling debundled SWNTs[238]. In any case, we find the neglect of LFEs is justified for these systems, especially because our primary interest is the first excited state in SWNTs (E_{11}) transition along the SWNT axis.

Bibliography

[1] Chapin, D. M.; Fuller, C.; Pearson, G. A new silicon p-n junction photocell for converting solar radiation into electrical power. *J. Appl. Phys.* **1954**, *25*, 676–677.

[2] Secretariat, R. Renewables 2016 global status report. *REN21, Paris, Tech. Rep* **2016**,

[3] Goldemberg, J. *World Energy Assessment: Energy and the challenge of sustainability*; United Nations Pubns, 2000.

[4] Wirth, H.; Schneider, K. Aktuelle Fakten zur Photovoltaik in Deutschland. *Fraunhofer ISE* **2012**,

[5] Bolto, B. A.; McNeill, R.; Weiss, D. Electronic conduction in polymers. III. Electronic properties of polypyrrole. *Aust. J. Chem.* **1963**, *16*, 1090–1103.

[6] Shirakawa, H.; Louis, E. J.; MacDiarmid, A. G.; Chiang, C. K.; Heeger, A. J. Synthesis of electrically conducting organic polymers: halogen derivatives of polyacetylene, (CH). *J. Chem. Soc., Chem. Commun.* **1977**, 578–580.

[7] Diaz, A.; Logan, J. Electroactive polyaniline films. *J. Electroanal. Chem. Interfac.* **1980**, *111*, 111–114.

[8] Zhang, X.; MacDiarmid, A. G.; Manohar, S. K. Chemical synthesis of PEDOT nanofibers. *Chem. Commun.* **2005**, 5328–5330.

[9] Boehm, H. P.; Clauss, A.; Fischer, G. O.; Hofmann, U. Das Adsorptionsverhalten sehr dünner Kohlenstoff-Folien. *Z. Anorg. Allg. Chem.* **1962**, *316*, 119–127.

[10] Novoselov, K. S.; Geim, A. K.; Morozov, S. V.; Jiang, D.; Zhang, Y.; Dubonos, S. V.; Grigorieva, I. V.; Firsov, A. A. Electric Field Effect in Atomically Thin Carbon Films. *Science* **2004**, *306*, 666–669.

[11] Osawa, E. Superaromaticity. *Kagaku* **1970**, *25*, 101.

[12] Iijima, S. Helical microtubules of graphitic carbon. *Nature* **1991**, *354*, 56–58.

[13] Радучкевитч, ЛВ,; Лукяновитч, ВМ, О структуре углерода образующегося при термическом разложении окиси углерода на железном контакте. Журнал Физичес **1952**, *26*, 88–95.

[14] Oberlin, A.; Endo, M.; Koyama, T. Filamentous growth of carbon through benzene decomposition. *J. Cryst. Growth* **1976**, *32*, 335–349.

[15] Harris, P. J. F. *Carbon Nanotubes and Related Structures: New Materials for the Twenty-first Century*; Cambridge University Press: Cambridge, 1999.

[16] Heeger, A. J.; Mac Diarmid, A.; Shirakawa, H. The nobel prize in chemistry 2000. *The Nobel Foundation* **2000**,

[17] Zhao, J.; Wang, A.; Altermatt, P.; Green, M. A. Twenty-four percent efficient silicon solar cells with double layer antireflection coatings and reduced resistance loss. *Appl. Phys. Lett.* **1995**, *66*, 3636–3638.

[18] Green, M. A. The path to 25cell evolution. *Prog. Photovoltaics Res. Appl.* **2009**, *17*, 183–189.

[19] Shockley, W.; Queisser, H. J. Detailed Balance Limit of Efficiency of p-n Junction Solar Cells. *J. Appl. Phys.* **1961**, *32*, 510–519.

[20] Scharber, M.; Sariciftci, N. Efficiency of bulk-heterojunction organic solar cells. *Prog. Polym. Sci.* **2013**, *38*, 1929 – 1940.

[21] Green, M. A.; Emery, K.; Hishikawa, Y.; Warta, W.; Dunlop, E. D. Solar cell efficiency tables (version 46). *Prog. Photovoltaics Res. Appl.* **2015**, *23*, 805–812.

[22] Gregg, B. A. Excitonic Solar Cells. *J. Phys. Chem. B* **2003**, *107*, 4688–4698.

[23] Scholes, G. D.; Rumbles, G. Excitons in nanoscale systems. *Nat. Mater.* **2006**, *5*, 683–696.

[24] Dvorak, M.; Wei, S.-H.; Wu, Z. Origin of the variation of exciton binding energy in semiconductors. *Phys. Rev. Lett.* **2013**, *110*, 016402.

[25] Dimitrov, S. D.; Schroeder, B. C.; Nielsen, C. B.; Bronstein, H.; Fei, Z.; McCulloch, I.; Heeney, M.; Durrant, J. R. Singlet exciton lifetimes in conjugated polymer films for organic solar cells. *Polymers* **2016**, *8*, 14.

[26] Sariciftci, N. S.; Smilowitz, L.; Heeger, A. J.; Wudl, F. Photoinduced Electron Transfer from a Conducting Polymer to Buckminsterfullerene. *Science* **1992**, *258*, 1474–1476.

[27] Halls, J. J. M.; Pichler, K.; Friend, R. H.; Moratti, S. C.; Holmes, A. B. Exciton diffusion and dissociation in a poly(p-phenylenevinylene)/C60 heterojunction photovoltaic cell. *Appl. Phys. Lett.* **1996**, *68*, 3120–3122.

[28] Brabec, C. J.; Zerza, G.; Cerullo, G.; De Silvestri, S.; Luzzati, S.; Hummelen, J. C.; Sariciftci, S. Tracing photoinduced electron transfer process in conjugated polymer/fullerene bulk heterojunctions in real time. *Chem. Phys. Lett.* **2001**, *340*, 232–236.

[29] Deibel, C.; Dyakonov, V. Polymer–fullerene bulk heterojunction solar cells. *Rep. Prog. Phys.* **2010**, *73*, 096401.

[30] Yu, G.; Gao, J.; Hummelen, J. C.; Wudl, F.; Heeger, A. J. Polymer Photovoltaic Cells: Enhanced Efficiencies via a Network of Internal Donor-Acceptor Heterojunctions. *Science* **1995**, *270*, 1789–1791.

[31] Mikhnenko, O. V.; Azimi, H.; Scharber, M.; Morana, M.; Blom, P. W. M.; Loi, M. A. Exciton diffusion length in narrow bandgap polymers. *Energy Environ. Sci.* **2012**, *5*, 6960–6965.

[32] Langevin, P. Sur la loi de recombination des ions. *Ann. Chim. Phys* **1903**, *28*, 433–530.

[33] Dennler, G.; Mozer, A.; Juška, G.; Pivrikas, A.; Österbacka, R.; Fuchsbauer, A.; Sariciftci, N. Charge carrier mobility and lifetime versus composition of conjugated polymer/fullerene bulk-heterojunction solar cells. *Org. Electron.* **2006**, *7*, 229–234.

[34] Cowan, S. R.; Roy, A.; Heeger, A. J. Recombination in polymer-fullerene bulk heterojunction solar cells. *Phys. Rev. B* **2010**, *82*, 245207.

[35] Lakhwani, G.; Rao, A.; Friend, R. H. Bimolecular recombination in organic photovoltaics. *Ann. Rev. Phys. Chem.* **2014**, *65*, 557–581.

[36] Onsager, L. Deviations from Ohm's law in weak electrolytes. *J. Chem. Phys.* **1934**, *2*, 599–615.

[37] Vandewal, K.; Tvingstedt, K.; Gadisa, A.; Inganäs, O.; Manca, J. V. On the origin of the open-circuit voltage of polymer–fullerene solar cells. *Nat. Mater.* **2009**, *8*, 904–909.

[38] Burke, T. M.; Sweetnam, S.; Vandewal, K.; McGehee, M. D. Beyond Langevin Recombination: How Equilibrium Between Free Carriers and Charge Transfer States Determines the Open-Circuit Voltage of Organic Solar Cells. *Adv. Energy Mater.* **2015**, *5*.

[39] Kirchartz, T.; Taretto, K.; Rau, U. Efficiency limits of organic bulk heterojunction solar cells. *J. Phys. Chem. C* **2009**, *113*, 17958–17966.

[40] Sun, S.-S.; Sariciftci, N. S. *Organic photovoltaics: mechanisms, materials, and devices*; CRC press, 2005.

[41] Pandey, R.; Gunawan, A. A.; Mkhoyan, K. A.; Holmes, R. J. Efficient organic photovoltaic cells based on nanocrystalline mixtures of boron subphthalocyanine chloride and C60. *Adv. Funct. Mater.* **2012**, *22*, 617–624.

[42] Kim, G.-H.; Song, H.-K.; Kim, J. Y. The effect of introducing a buffer layer to polymer solar cells on cell efficiency. *Sol. Energ. Mat. Sol. Cells* **2011**, *95*, 1119–1122.

[43] Hu, Z.; Zhang, J.; Hao, Z.; Zhao, Y. Influence of doped PEDOT: PSS on the performance of polymer solar cells. *Sol. Energ. Mat. Sol. Cells* **2011**, *95*, 2763–2767.

[44] Xu, W.; Yan, C.; Kan, Z.; Wang, Y.; Lai, W.-Y.; Huang, W. High Efficiency Inverted Organic Solar Cells with a Neutral Fulleropyrrolidine Electron Collecting Interlayer. *ACS Appl. Mater. Interfaces* **2016**,

[45] Krebs, F. C. Air stable polymer photovoltaics based on a process free from vacuum steps and fullerenes. *Sol. Energ. Mat. Sol. Cells* **2008**, *92*, 715–726.

[46] Mandoc, M.; Koster, L.; Blom, P. Optimum charge carrier mobility in organic solar cells. *Appl. Phys. Lett.* **2007**, *90*, 133504.

[47] Baughman, R. H.; Zakhidov, A. A.; de Heer, W. A. Carbon nanotubes–the route toward applications. *Science* **2002**, *297*, 787–792.

[48] Spataru, C. D.; Ismail-Beigi, S.; Benedict, L. X.; Louie, S. G. Excitonic Effects and Optical Spectra of Single-Walled Carbon Nanotubes. *Phys. Rev. Lett.* **2004**, *92*, 077402.

[49] Kataura, H.; Kumazawa, Y.; Maniwa, Y.; Umezu, I.; Suzuki, S.; Ohtsuka, Y.; Achiba, Y. Optical properties of single-wall carbon nanotubes. *Syn. Metals* **1999**, *103*, 2555–2558.

[50] Yamamoto, T.; Watanabe, K.; Hernández, E. R. In *Carbon Nanotubes: Advanced Topics in the Synthesis, Structure, Properties and Applications*; Jorio, A., Dresselhaus, G., Dresselhaus, M. S., Eds.; Springer Berlin Heidelberg: Berlin, Heidelberg, 2008; pp 165–195.

[51] Liew, K. M.; Wong, C. H.; He, X. Q.; Tan, M. J. Thermal stability of single and multi-walled carbon nanotubes. *Phys. Rev. B* **2005**, *71*, 075424.

[52] White, C. T.; Todorov, T. N. Carbon nanotubes as long ballistic conductors. *Nature* **1998**, *393*, 240–242.

[53] Dürkop, T.; Getty, S. A.; Cobas, E.; Fuhrer, M. S. Extraordinary Mobility in Semiconducting Carbon Nanotubes. *Nano Lett.* **2004**, *4*, 35–39.

[54] Lin, Y.-M.; Appenzeller, J.; Knoch, J.; Avouris, P. High-performance carbon nanotube field-effect transistor with tunable polarities. *IEEE Trans. Nanotechnol.* **2005**, *4*, 481–489.

[55] Martel, R.; Schmidt, T.; Shea, H. R.; Hertel, T.; Avouris, P. Single- and multi-wall carbon nanotube field-effect transistors. *Appl. Phys. Lett.* **1998**, *73*, 2447–2449.

[56] Bockrath, M.; Hone, J.; Zettl, A.; McEuen, P. L.; Rinzler, A. G.; Smalley, R. E. Chemical doping of individual semiconducting carbon-nanotube ropes. *Phys. Rev. B* **2000**, *61*, R10606–R10608.

[57] Yao, Z.; Kane, C. L.; Dekker, C. High-Field Electrical Transport in Single-Wall Carbon Nanotubes. *Phys. Rev. Lett.* **2000**, *84*, 2941–2944.

[58] Soavi, G.; Scotognella, F.; Brida, D.; Hefner, T.; SpÃd'th, F.; Antognazza, M. R.; Hertel, T.; Lanzani, G.; Cerullo, G. Ultrafast Charge Photogeneration in Semiconducting Carbon Nanotubes. *J. Phys. Chem. C* **2013**, *117*, 10849–10855.

[59] Jensen, S. A.; Ulbricht, R.; Narita, A.; Feng, X.; Müllen, K.; Hertel, T.; Turchinovich, D.; Bonn, M. Ultrafast Photoconductivity of Graphene Nanoribbons and Carbon Nanotubes. *Nano Lett.* **2013**, *13*, 5925–5930.

[60] Kumamoto, Y.; Yoshida, M.; Ishii, A.; Yokoyama, A.; Shimada, T.; Kato, Y. K. Spontaneous Exciton Dissociation in Carbon Nanotubes. *Phys. Rev. Lett.* **2014**, *112*, 117401.

[61] Crochet, J. J.; Hoseinkhani, S.; Lüer, L.; Hertel, T.; Doorn, S. K.; Lanzani, G. Free-Carrier Generation in Aggregates of Single-Wall Carbon Nanotubes by Photoexcitation in the Ultraviolet Regime. *Phys. Rev. Lett.* **2011**, *107*, 257402.

[62] Soavi, G.; Scotognella, F.; Viola, D.; Hefner, T.; Hertel, T.; Cerullo, G.; Lanzani, G. High energetic excitons in carbon nanotubes directly probe charge-carriers. *Sci. Rep.* **2015**, *5*, 9681.

[63] Ando, T. Excitons in Carbon Nanotubes. *J. Phys. Soc. Jap.* **1997**, *66*, 1066–1073.

[64] Perebeinos, V.; Tersoff, J.; Avouris, P. Scaling of Excitons in Carbon Nanotubes. *Phys. Rev. Lett.* **2004**, *92*, 257402.

[65] Wang, F.; Dukovic, G.; Brus, L. E.; Heinz, T. F. The Optical Resonances in Carbon Nanotubes Arise from Excitons. *Science* **2005**, *308*, 838–841.

[66] Maultzsch, J.; Pomraenke, R.; Reich, S.; Chang, E.; Prezzi, D.; Ruini, A.; Molinari, E.; Strano, M. S.; Thomsen, C.; Lienau, C. Exciton Binding Energies in Carbon Nanotubes from Two-Photon Photoluminescence. *Phys. Rev. B* **2005**, *72*, 241402.

[67] Spataru, C. D.; Léonard, F. Tunable Band Gaps and Excitons in Doped Semiconducting Carbon Nanotubes Made Possible by Acoustic Plasmons. *Phys. Rev. Lett.* **2010**, *104*, 177402.

[68] Arnold, M. S.; Zimmerman, J. D.; Renshaw, C. K.; Xu, X.; Lunt, R. R.; Austin, C. M.; Forrest, S. R. Broad Spectral Response Using Carbon Nanotube/Organic Semiconductor/C60 Photodetectors. *Nano Lett.* **2009**, *9*, 3354–3358.

[69] Bindl, D. J.; Ferguson, A. J.; Wu, M.-Y.; Kopidakis, N.; Blackburn, J. L.; Arnold, M. S. Free Carrier Generation and Recombination in Polymer-Wrapped Semiconducting Carbon Nanotube Films and Heterojunctions. *J. Phys. Chem. Lett.* **2013**, *4*, 3550–3559.

[70] Bindl, D. J.; Arnold, M. S. Efficient Exciton Relaxation and Charge Generation in Nearly Monochiral (7,5) Carbon Nanotube/C60 Thin-Film Photovoltaics. *J. Phys. Chem. C* **2013**, *117*, 2390–2395.

[71] Bindl, D. J.; Wu, M.-Y.; Prehn, F. C.; Arnold, M. S. Efficiently Harvesting Excitons from Electronic Type-Controlled Semiconducting Carbon Nanotube Films. *Nano Lett.* **2011**, *11*, 455–460.

[72] Bindl, D. J.; Safron, N. S.; Arnold, M. S. Dissociating Excitons Photogenerated in Semiconducting Carbon Nanotubes at Polymeric Photovoltaic Heterojunction Interfaces. *ACS Nano* **2010**, *4*, 5657–5664.

[73] Bindl, D. J.; Brewer, A. S.; Arnold, M. S. Semiconducting carbon nanotube/fullerene blended heterojunctions for photovoltaic near-infrared photon harvesting. *Nano Res.* **2011**, *4*, 1174–1179.

[74] Jain, R. M.; Howden, R.; Tvrdy, K.; Shimizu, S.; Hilmer, A. J.; McNicholas, T. P.; Gleason, K. K.; Strano, M. S. Polymer-Free Near-Infrared Photovoltaics with Single Chirality (6,5) Semiconducting Carbon Nanotube Active Layers. *Adv. Mater.* **2012**, *24*, 4436–4439.

[75] Kymakis, E.; Amaratunga, G. A. J. Single-Wall Carbon Nanotube/Conjugated Polymer Photovoltaic Devices. *Appl. Phys. Lett.* **2002**, *80*, 112–114.

[76] Kymakis, E.; Alexandrou, I.; Amaratunga, G. A. J. High Open-Circuit Voltage Photovoltaic Devices from Carbon-Nanotube-Polymer Composites. *J. Appl. Phys.* **2003**, *93*, 1764–1768.

[77] Stich, D.; Späth, F.; Kraus, H.; Sperlich, A.; Dyakonov, V.; Hertel, T. Triplet-Triplet Exciton Dynamics in Single-Walled Carbon Nanotubes. *Nat. Photon.* **2014**, *8*, 1749–4885.

[78] Ferguson, A. J.; Blackburn, J. L.; Kopidakis, N. Fullerenes and Carbon Nanotubes as Acceptor Materials in Organic Photovoltaics. *Mater. Lett.* **2013**, *90*, 115–125.

[79] Yan, J.; Ni, T.; Zou, F.; Zhang, L.; Yang, D.; Yang, S.; Zou, B. Towards optimization of functionalized single-walled carbon nanotubes adhering with poly (3-hexylthiophene) for highly efficient polymer solar cells. *Diamond Relat. Mater.* **2014**, *41*, 79–83.

[80] Ren, S.; Bernardi, M.; Lunt, R. R.; Bulovic, V.; Grossman, J. C.; GradeÄ𝐷ak, S. Toward Efficient Carbon Nanotube/P3HT Solar Cells: Active Layer Morphology, Electrical, and Optical Properties. *Nano Lett.* **2011**, *11*, 5316–5321.

[81] Kymakis, E.; Kornilios, N.; Koudoumas, E. Carbon nanotube doping of P3HT: PCBM photovoltaic devices. *J. Phys. D: Appl. Phys.* **2008**, *41*, 165110.

[82] Li, C.; Mitra, S. Processing of fullerene-single wall carbon nanotube complex for bulk heterojunction photovoltaic cells. *Appl. Phys. Lett.* **2007**, *91*, 3112.

[83] Berson, S.; de Bettignies, R.; Bailly, S.; Guillerez, S.; Jousselme, B. Elaboration of P3HT/CNT/PCBM composites for organic photovoltaic cells. *Adv. Funct. Mater.* **2007**, *17*, 3363–3370.

[84] Dang, M. T.; Hirsch, L.; Wantz, G. P3HT:PCBM, Best Seller in Polymer Photovoltaic Research. *Adv. Mater.* **2011**, *23*, 3597–3602.

[85] Figueroa del Valle, D. G.; Scotognella, F.; Lanzani, G. private communication.

[86] Glanzmann, L. N.; Mowbray, D. J. Theoretical Insight into the Internal Quantum Efficiencies of Polymer/C_{60} and Polymer/SWNT Photovoltaic Devices. *J. Phys. Chem. C* **2016**, *120*, 6336–6343.

[87] Ratier, B.; Nunzi, J.-M.; Aldissi, M.; Kraft, T. M.; Buncel, E. Organic solar cell materials and active layer designs—improvements with carbon nanotubes: a review. *Polym. Int.* **2012**, *61*, 342–354.

[88] Gomulya, W.; Gao, J.; Loi, M. A. Conjugated Polymer-Wrapped Carbon Nanotubes: Physical Properties and Device Applications. *Euro. Phys. J. B* **2013**, *86*.

[89] Journet, C.; Maser, W.; Bernier, P.; Loiseau, A.; De La Chapelle, M. L.; Lefrant, d. l. S.; Deniard, P.; Lee, R.; Fischer, J. Large-scale production of single-walled carbon nanotubes by the electric-arc technique. *Nature* **1997**, *388*, 756–758.

[90] Guo, T.; Nikolaev, P.; Thess, A.; Colbert, D.; Smalley, R. Catalytic growth of single-walled manotubes by laser vaporization. *Chem. Phys. Lett.* **1995**, *243*, 49–54.

[91] Endo, M.; Takeuchi, K.; Kobori, K.; Takahashi, K.; Kroto, H. W.; Sarkar, A. Pyrolytic carbon nanotubes from vapor-grown carbon fibers. *Carbon* **1995**, *33*, 873–881.

[92] Dai, H.; Rinzler, A. G.; Nikolaev, P.; Thess, A.; Colbert, D. T.; Smalley, R. E. Single-wall nanotubes produced by metal-catalyzed disproportionation of carbon monoxide. *Chem. Phys. Lett.* **1996**, *260*, 471–475.

[93] Kitiyanan, B.; Alvarez, W. E.; Harwell, J. H.; Resasco, D. E. Controlled production of single-wall carbon nanotubes by catalytic decomposition of CO on bimetallic Co-Mo catalysts. *Chem. Phys. Lett.* **2000**, *317*, 497.

[94] Gong, M.; Shastry, T. A.; Xie, Y.; Bernardi, M.; Jasion, D.; Luck, K. A.; Marks, T. J.; Grossman, J. C.; Ren, S.; Hersam, M. C. Polychiral semiconducting carbon nanotube–fullerene solar cells. *Nano Lett.* **2014**, *14*, 5308–5314.

[95] Mehlenbacher, R. D.; McDonough, T. J.; Grechko, M.; Wu, M.-Y.; Arnold, M. S.; Zanni, M. T. Energy transfer pathways in semiconducting carbon nanotubes revealed using two-dimensional white-light spectroscopy. *Nat. Commun.* **2015**, *6*.

[96] Qian, H.; Georgi, C.; Anderson, N.; Green, A. A.; Hersam, M. C.; Novotny, L.; Hartschuh, A. Exciton transfer and propagation in carbon nanotubes studied by near-field optical microscopy. *Phys. Stat. Solidi B* **2008**, *245*, 2243–2246.

[97] Holt, J. M.; Ferguson, A. J.; Kopidakis, N.; Larsen, B. A.; Bult, J.; Rumbles, G.; Blackburn, J. L. Prolonging Charge Separation in P3HT–SWNT Composites Using Highly Enriched Semiconducting Nanotubes. *Nano Lett.* **2010**, *10*, 4627–4633.

[98] Mallajosyula, A.; Iyer, S. S. K.; Mazhari, B. Conduction properties of carbon nanotubes in P3HT:SWNT bulk heterojunction solar cells. Photovoltaic Specialists Conference, 2008. PVSC '08. 33rd IEEE. 2008; pp 1–6.

[99] Liu, C.-H.; Zhang, H.-L. Chemical approaches towards single-species single-walled carbon nanotubes. *Nanoscale* **2010**, *2*, 1901–1918.

[100] Martel, R. Sorting carbon nanotubes for electronics. *ACS Nano* **2008**, *2*, 2195–2199.

[101] O'Connell, M. J.; Bachilo, S. M.; Huffman, C. B.; Moore, V. C.; Strano, M. S.; Haroz, E. H.; Rialon, K. L.; Boul, P. J.; Noon, W. H.; Kittrell, C.; Ma, J. P.; Hauge, R. H.; Weisman, R. B.; Smalley, R. E. Band gap fluorescence from individual single-walled carbon nanotubes. *Science* **2002**, *297*, 593.

[102] Arnold, M. S.; Green, A. A.; Hulvat, J. F.; Stupp, S. I.; Hersam, M. C. Sorting carbon nanotubes by electronic structure using density differentiation. *Nat. Nanotechnol.* **2006**, *1*, 60–65.

[103] Zheng, M.; Jagota, A.; Semke, E. D.; Diner, B. A.; Mclean, R. S.; Lustig, S. R.; Richardson, R. E.; Tassi, N. G. DNA-assisted dispersion and separation of carbon nanotubes. *Nat. Mater.* **2003**, *2*, 338.

[104] Zheng, M.; Jagota, A.; Strano, M. S.; Santos, A. P.; Barone, P.; Chou, S. G.; Diner, B. A.; Dresselhaus, M. S.; McLean, R. S.; Onoa, G. B.; Samsonidze, G. G.; Semke, E. D.; Usrey, M.; Walls, D. J. Structure-based carbon nanotube sorting by sequence-dependent DNA assembly. *Science* **2003**, *302*, 1545.

[105] Krupke, R.; Hennrich, F.; Löhneysen, H. v.; Kappes, M. M. Separation of Metallic from Semiconducting Single-Walled Carbon Nanotubes. *Science* **2003**, *301*, 344–347.

[106] Liu, H.; Nishide, D.; Tanaka, T.; Kataura, H. Large-scale single-chirality separation of single-wall carbon nanotubes by simple gel chromatography. *Nat. Commun.* **2011**, *2*, 309.

[107] Nakashima, N. Solubilization of single-walled carbon nanotubes with condensed aromatic compounds. *Sci. Tech. of Adv. Mater.* **2006**, *7*, 609.

[108] Nakashima, N.; Fujigaya, T. Methodology for Homogeneous Dispersion of Single-walled Carbon Nanotubes by Physical Modification. *Polym. J.* **2008**, *40*, 577–589.

[109] Nakashima, N.; Fujigaya, T. Fundamentals and Applications of Soluble Carbon Nanotubes. *Chem. Lett.* **2007**, *36*, 692–697.

[110] Chen, F.; Wang, B.; Chen, Y.; Li, L.-J. Toward the Extraction of Single Species of Single-Walled Carbon Nanotubes Using Fluorene-Based Polymers. *Nano Lett.* **2007**, *7*, 3013–3017.

[111] Lee, H. W.; Yonn, Y. Selective dispersion of high purity semiconducting single-walled carbon nanotubes with regioregular poly(3-alkylthiophene)s. *Nat. Commun.* **2011**, *2*, 541.

[112] Ozawa, H.; Ide, N.; Fujigaya, T.; Niidome, Y.; Nakashima, N. One-pot Separation of Highly Enriched (6,5)-Single-walled Carbon Nanotubes Using a Fluorene-based Copolymer. *Chem. Lett.* **2011**, *40*, 239–241.

[113] Nish, A.; Hwang, J.-Y.; Doig, J.; Nicholas, R. J. Highly selective dispersion of single-walled carbon nanotubes using aromatic polymers. *Nat. Nanotech.* **2007**, *2*, 640–646.

[114] Gao, J.; Loi, M. A.; de Carvalho, E. J. F.; dos Santos, M. C. Selective wrapping and supramolecular structures of polyfluorene–carbon nanotube hybrids. *ACS Nano* **2011**, *5*, 3993–3999.

[115] Saha, L. C.; Mian, S. A.; Jang, J.-K. Molecular Dynamics Simulation Study on the Carbon NanotubeInteracting with a Polymer. *Bull. Korean Chem. Soc.* **2012**, *33*, 893–896.

[116] Liu, W.; Yang, C.-L.; Zhu, Y.-T.; Wang, M.-s. Interactions between single-walled carbon nanotubes and polyethylene/polypropylene/polystyrene/poly (phenylacetylene)/poly (p-phenylenevinylene) considering repeat unit arrangements and conformations: a molecular dynamics simulation study. *J. Phys. Chem. C* **2008**, *112*, 1803–1811.

[117] Naito, M.; Nobusawa, K.; Onouchi, H.; Nakamura, M.; Yasui, K.-i.; Ikeda, A.; Fujiki, M. Stiffness-and conformation-dependent polymer wrapping onto single-walled carbon nanotubes. *J. Am. Chem. Soc.* **2008**, *130*, 16697–16703.

[118] Marchiori, C. F. N.; Koehler, M. Density functional theory study of the dipole across the P3HT:PCBM complex: the role of polarization and charge transfer. *J. Phys. D: Appl. Phys.* **2014**, *47*, 215104.

[119] Yan, J.; Thygesen, K. S.; Jacobsen, K. W. Nonlocal Screening of Plasmons in Graphene by Semiconducting and Metallic Substrates: First-Principles Calculations. *Phys. Rev. Lett.* **2011**, *106*, 146803.

[120] Yan, J.; Mortensen, J. J.; Jacobsen, K. W.; Thygesen, K. S. Linear density response function in the projector augmented wave method: Applications to solids, surfaces, and interfaces. *Phys. Rev. B* **2011**, *83*, 245122.

[121] Glanzmann, L. N.; Mowbray, D. J.; Rubio, A. PFO-BPy Solubilizers for SWNTs: Modelling Polymers from Oligomers. *Phys. Stat. Solidi B* **2014**, *251*, 2407–2412.

[122] Fiolhais, C., Nogueira, F., Marques, M., Eds. *A Primer in Density Functional Theory*; Lecture notes in physics; Springer-Verlag: Berlin, 2003.

[123] Engel, E.; Dreizler, R. M. *Density Functional Theory: An Advanced Course*; Springer-Verlag: Berlin, 2011.

[124] Dion, M.; Rydberg, H.; Schröder, E.; Langreth, D. C.; Lundqvist, B. I. Van der Waals Density Functional for General Geometries. *Phys. Rev. Lett.* **2004**, *92*, 246401.

[125] Mortensen, J. J.; Hansen, L. B.; Jacobsen, K. W. Real-Space Grid Implementation of the Projector Augmented Wave Method. *Phys. Rev. B* **2005**, *71*, 035109.

[126] Enkovaara, J. *et al.* Electronic Structure Calculations with GPAW: A Real-Space Implementation of the Projector Augmented-Wave Method. *J. Phys.: Condens. Matter* **2010**, *22*, 253202.

[127] Vladar, A. E. Strategies for scanning electron microscopy sample preparation and characterization of multi-wall carbon nanotube polymer composites. *NIST Special Publication* **2015**, *1200*, 17.

[128] Loos, J.; Alexeev, A.; Grossiord, N.; Koning, C. E.; Regev, O. Visualization of single-wall carbon nanotube (SWNT) networks in conductive polystyrene nanocomposites by charge contrast imaging. *Ultramicroscopy* **2005**, *104*, 160–167.

[129] Shea, M. J.; Mehlenbacher, R. D.; Zanni, M. T.; Arnold, M. S. Experimental Measurement of the Binding Configuration and Coverage of Chirality-Sorting Polyfluorenes on Carbon Nanotubes. *J. Phys. Chem. Lett.* **2014**, *5*, 3742–3749.

[130] Dresselhaus, M. S.; Dresselhaus, G.; Saito, R.; Jorio, A. Exciton photophysics of carbon nanotubes. *Annu. Rev. Phys. Chem.* **2007**, *58*, 719–747.

[131] Ajiki, H. Exciton states and optical properties of carbon nanotubes. *J. Phys.: Condens. Matter* **2012**, *24*, 483001.

[132] Kaiser, W.; Auston, D. H. *Ultrashort laser pulses: generation and applications*; Springer, 1993.

[133] Berera, R.; van Grondelle, R.; Kennis, J. T. Ultrafast transient absorption spectroscopy: principles and application to photosynthetic systems. *Photosyn. Res.* **2009**, *101*, 105–118.

[134] Lüer, S., Larry ans Hoseinkhani; Polli, D.; Crochet, J.; Hertel, T.; Lanzani, G. Size and mobility of excitons in (6, 5) carbon nanotubes. *Nat. Phys.* **2009**, *5*, 54–58.

[135] Greene, B. I.; Orenstein, J.; Schmitt-Rink, S. All-Optical Nonlinearities in Organics. *Science* **1990**, *247*, 679–687.

[136] Manzoni, C.; Gambetta, A.; Menna, E.; Meneghetti, M.; Lanzani, G.; Cerullo, G. Intersubband Exciton Relaxation Dynamics in Single-Walled Carbon Nanotubes. *Phys. Rev. Lett.* **2005**, *94*, 207401.

[137] Gambetta, A.; Manzoni, C.; Menna, E.; Meneghetti, M.; Cerullo, G.; Lanzani, G.; Tretiak, S.; Piryatinski, A.; Saxena, A.; Martin, R. L.; Bishop, A. R. Real-time observation of nonlinear coherent phonon dynamics in single-walled carbon nanotubes. *Nat. Phys.* **2006**, *2*, 515–520.

[138] Lüer, L.; Gadermaier, C.; Crochet, J.; Hertel, T.; Brida, D.; Lanzani, G. Coherent Phonon Dynamics in Semiconducting Carbon Nanotubes: A Quantitative Study of Electron-Phonon Coupling. *Phys. Rev. Lett.* **2009**, *102*, 127401.

[139] Styers-Barnett, D. J.; Ellison, S. P.; Mehl, B. P.; Westlake, B. C.; House, R. L.; Park, C.; Wise, K. E.; ; Papanikolas, J. M. Exciton Dynamics and Biexciton Formation in Single-Walled Carbon Nanotubes Studied with Femtosecond Transient Absorption Spectroscopy. *J. Phys. Chem. C* **2008**, *112*, 4507–4516.

[140] Pedersen, T. G.; Pedersen, K.; Cornean, H. D.; Duclos, P. Stability and Signatures of Biexcitons in Carbon Nanotubes. *Nano Lett.* **2005**, *5*, 291–294.

[141] Rønnow, T. F.; Pedersen, T. G.; Cornean, H. D. Correlation and dimensional effects of trions in carbon nanotubes. *Phys. Rev. B* **2010**, *81*, 205446.

[142] Hartleb, H.; Späth, F.; Hertel, T. Evidence for Strong Electronic Correlations in the Spectra of Gate-Doped Single-Wall Carbon Nanotubes. *ACS Nano* **2015**, *9*, 10461–10470.

[143] Soavi, G.; Scotognella, F.; Brida, D.; Hefner, T.; SpÃd'th, F.; Antognazza, M. R.; Hertel, T.; Lanzani, G.; Cerullo, G. Ultrafast Charge Photogeneration in Semiconducting Carbon Nanotubes. *J. Phys. Chem. C* **2013**, *117*, 10849–10855.

[144] Zhu, Z.; Crochet, J.; Arnold, M. S.; Hersam, M. C.; Ulbricht, H.; Resasco, D.; Hertel, T. Pump-Probe Spectroscopy of Exciton Dynamics in (6,5) Carbon Nanotubes. *J. Phys. Chem. C* **2007**, *111*, 3831–3835.

[145] Zi-Peng, Z. Photo-induced absorption in the pump probe spectroscopy of single-walled carbon nanotubes. *Chin. Phys. B* **2013**, *22*, 077803.

[146] Marques, M. A. L.; Maitra, N.; Nogueira, F.; Gross, E. K. U.; Rubio, A. *Fundamentals of Time-dependent Density Functional Theory*; Springer-Verlag: Berlin-Heidelberg, 2011.

[147] Marcus, R. A. Electron transfer reactions in chemistry: theory and experiment (Nobel lecture). *Angew. Chem. Int. Ed.* **1993**, *32*, 1111–1121.

[148] Yi, Y.; Coropceanu, V.; Brédas, J.-L. A comparative theoretical study of exciton-dissociation and charge-recombination processes in oligothiophene/fullerene and oligothiophene/perylenediimide complexes for organic solar cells. *J. Mater. Chem.* **2011**, *21*, 1479–1486.

[149] Liu, T.; Troisi, A. Absolute rate of charge separation and recombination in a molecular model of the P3HT/PCBM interface. *J. Phys. Chem. C* **2011**, *115*, 2406–2415.

[150] Kanai, Y.; Grossman, J. C. Insights on interfacial charge transfer across P3HT/fullerene photovoltaic heterojunction from ab initio calculations. *Nano Lett.* **2007**, *7*, 1967–1972.

[151] Huang, Y.-s.; Westenhoff, S.; Avilov, I.; Sreearunothai, P.; Hodgkiss, J. M.; Deleener, C.; Friend, R. H.; Beljonne, D. Electronic structures of interfacial states formed at polymeric semiconductor heterojunctions. *Nat. Mater.* **2008**, *7*, 483–489.

[152] Yi, Y.; Coropceanu, V.; Brédas, J.-L. Exciton-dissociation and charge-recombination processes in pentacene/C60 solar cells: theoretical insight into the impact of interface geometry. *J. Am. Chem. Soc.* **2009**, *131*, 15777–15783.

[153] Marchiori, C.; Koehler, M. Dipole assisted exciton dissociation at conjugated polymer/fullerene photovoltaic interfaces: A molecular study using density functional theory calculations. *Syn. Metals* **2010**, *160*, 643–650.

[154] Grancini, G.; Polli, D.; Fazzi, D.; Cabanillas-Gonzalez, J.; Cerullo, G.; Lanzani, G. Transient absorption imaging of P3HT: PCBM photovoltaic blend: Evidence for interfacial charge transfer state. *J. Phys. Chem. Lett.* **2011**, *2*, 1099–1105.

[155] Li, Y.; Qi, D.; Song, P.; Ma, F. Fullerene-based photoactive layers for heterojunction solar cells: structure, absorption spectra and charge transfer process. *Materials* **2014**, *8*, 42–56.

[156] Falke, S. M.; Rozzi, C. A.; Brida, D.; Maiuri, M.; Amato, M.; Sommer, E.; De Sio, A.; Rubio, A.; Cerullo, G.; Molinari, E. Coherent ultrafast charge transfer in an organic photovoltaic blend. *Science* **2014**, *344*, 1001–1005.

[157] Adler, S. L. Quantum Theory of the Dielectric Constant in Real Solids. *Phys. Rev.* **1962**, *126*, 413–420.

[158] Hybertsen, M. S.; Louie, S. G. Ab initio static dielectric matrices from the density-functional approach. I. Formulation and application to semiconductors and insulators. *Phys. Rev. B* **1987**, *35*, 5585.

[159] U. S. Department of Energy. Photovoltaic Cell Quantum Efficiency Basics. http://energy.gov/eere/energybasics/articles/photovoltaic-cell-quantum-efficiency-basics (accessed Aug 20, 2013).

[160] Kanai, Y.; Grossman, J. C. Insights on Interfacial Charge Transfer Across P3HT/Fullerene Photovoltaic Heterojunction from Ab Initio Calculations. *Nano Lett.* **2007**, *7*, 1967–1972.

[161] Kanai, Y.; Grossman, J. C. Role of Semiconducting and Metallic Tubes in P3HT/Carbon-Nanotube Photovoltaic Heterojunctions: Density Functional Theory Calculations. *Nano Lett.* **2008**, *8*, 908–912.

[162] Mowbray, D. J.; Morgan, C.; Thygesen, K. S. Influence of O_2 and N_2 on the Conductivity of Carbon Nanotube Networks. *Phys. Rev. B* **2009**, *79*, 195431.

[163] Meir, Y.; Wingreen, N. S. Landauer Formula for the Current Through an Interacting Electron Region. *Phys. Rev. Lett* **1992**, *68*, 2512–2515.

[164] Datta, S. *Electronic Transport in Mesoscopic Systems*, 1st ed.; Cambridge University Press: Cambridge, 1997.

[165] Thygesen, K.; Jacobsen, K. Molecular Transport Calculations with Wannier Functions. *Chem. Phys.* **2005**, *319*, 111–125.

[166] Thygesen, K. S. Electron Transport Through an Interacting Region: The Case of a Nonorthogonal Basis Set. *Phys. Rev. B* **2006**, *73*, 035309.

[167] Kohn, W. Nobel lecture: Electronic structure of matter - wave functions and density functionals. *Rev. Mod. Phys.* **1999**, *71*, 1253–1266.

[168] Schrödinger, E. An Undulatory Theory of the Mechanics of Atoms and Molecules. *Phys. Rev.* **1926**, *28*, 1049–1070.

[169] Born, M.; Oppenheimer, R. Zur Quantentheorie der Molekeln. *Ann. Phys.* **1927**, *20*, 467.

[170] Ritz, W. Über eine neue Methode zur Lösung gewisser Variationsprobleme der mathematischen Physik. *J. Reine. Angew. Math.* **1909**, *135*, 1–61.

[171] Hartree, D. R. The Wave Mechanics of an Atom with a Non-Coulomb Central Field. Part I. Theory and Methods. *Math. Proc. Cambridge* **1928**, *24*, 89–110.

[172] Fock, V. Näherungsmethode zur Lösung des quantenmechanischen Mehrkörperproblems. *Z. Phys.* **1930**, *61*, 126–148.

[173] Roothaan, C. C. J. New developments in molecular orbital theory. *Rev. Mod. Phys.* **1951**, *23*, 69.

[174] Hall, G. G. The molecular orbital theory of chemical valency. VIII. A method of calculating ionization potentials. Proceedings of the Royal Society of London A: Mathematical, Physical and Engineering Sciences. 1951; pp 541–552.

[175] Thomas, L. H. The calculation of atomic fields. *Proc. Cambridge Phil. Soc.* **1927**, *5*, 542.

[176] Fermi, E. Statistical method to determine some properties of atoms. *Atti. Accad. Lincei* **1927**, *6*, 602–607.

[177] Hohenberg, P.; Kohn, W. Inhomogeneous Electron Gas. *Phys. Rev.* **1964**, *136*, B864–B871.

[178] Kohn, W.; Sham, L. J. Self-Consistent Equations Including Exchange and Correlation Effects. *Phys. Rev.* **1965**, *140*, A1133–A1138.

[179] Perdew, J. P.; Kurth, S. In *A Tutorial on Density Functional Theory*; Fiolhais, C., Nogueira, F., Marques, M., Eds.; Springer-Verlag: Berlin Heidelberg, 2003; Chapter 1, pp 1–55.

[180] Harris, J.; Jones, R. O. The surface energy of a bounded electron gas. *J. Phys. F* **1974**, *4*, 1170–1186.

[181] Landgreth, D. C.; Perdew, J. P. The exchange-correlation energy of a metallic surface. *Sol. State Commun.* **1975**, *17*, 1425–1429.

[182] Gunnarsson, O.; Lundqvist, B. I. Exchange and correlation in atoms, molecules, and solids by the spin-density-functional formalism. *Phys. Rev. B* **1976**, *13*, 4274–4298.

[183] Parr, R. G.; Yang, W. *Density-Functional Theory of Atoms and Molecules*; Oxford University Press: New York, 1989.

[184] Perdew, J. P.; Burke, K.; Ernzerhof, M. Generalized Gradient Approximation Made Simple. *Phys. Rev. Lett.* **1996**, *77*, 3865–3868.

[185] Lieb, E. H.; Oxford, S. Improved lower bound on the indirect Coulomb energy. *Int. J. Quantum Chem.* **1981**, *19*, 427–439.

[186] Zhao, Y.; Truhlar, D. G. Construction of a generalized gradient approximation by restoring the density-gradient expansion and enforcing a tight LiebâĂŞOxford bound. *J. Chem. Phys.* **2008**, *128*, 184109.

[187] MA, S.-k.; BRUECKNER, K. A. Correlation Energy of an Electron Gas with a Slowly Varying High Density. *Phys. Rev.* **1968**, *165*, 18–31.

[188] Román-Pérez, G.; Soler, J. M. Efficient Implementation of a van der Waals Density Functional: Application to Double-Wall Carbon Nanotubes. *Phys. Rev. Lett.* **2009**, *103*, 096102.

[189] Bloch, F. Über die Quantenmechanik der Elektronen in Kristallgittern. *Z. Phys.* **1929**, *52*, 555–600.

[190] Kittel, C. *Introduction to Solid State Physics*, 7th ed.; 1996.

[191] Monkhorst, H. J.; Pack, J. D. Special points for Brillouin-zone integrations. *Phys. Rev. B* **1976**, *13*, 5188.

[192] Chelikowsky, J. R.; Troullier, N.; Saad, Y. Finite-difference-pseudopotential method: Electronic structure calculations without a basis. *Phys. Rev. Lett.* **1994**, *72*, 1240.

[193] Briggs, E. L.; Sullivan, D. J.; Bernholc, J. Large-scale electronic-structure calculations with multigrid acceleration. *Phys. Rev. B* **1995**, *52*, R5471.

[194] Marques, M. A. L.; Castro, A.; Bertsch, G. F.; Rubio, A. *Comput. Phys. Commun.* **2001**, *151*, 60–78.

[195] Heiskanen, M.; Torsti, T.; Puska, M. J.; Nieminen, R. M. Multigrid method for electronic structure calculations. *Phys. Rev. B* **2001**, *63*, 245106.

[196] Larsen, A. H.; Vanin, M.; Mortensen, J. J.; Thygesen, K. S.; Jacobsen, K. W. Localized Atomic Basis Set in the Projector Augmented Wave Method. *Phys. Rev. B* **2009**, *80*, 195112.

[197] Sankey, O. F.; Niklewski, D. J. Ab initio multicenter tight-binding model for molecular-dynamics simulations and other applications in covalent systems. *Phys. Rev. B* **1989**, *40*, 3979.

[198] Anglada, E.; M. Soler, J.; Junquera, J.; Artacho, E. Systematic generation of finite-range atomic basis sets for linear-scaling calculations. *Phys. Rev. B* **2002**, *66*, 205101.

[199] Soler, J. M.; Artacho, E.; Gale, J. D.; García, A.; Junquera, J.; Ordejón, P.; Sánchez-Portal, D. The SIESTA method for ab initio order- N materials simulation. *J. Phys.: Condens. Matter* **2002**, *14*, 2745.

[200] Blöchl, P. E. Projector augmented-wave method. *Phys. Rev. B* **1994**, *50*, 17953–17979.

[201] Blöchl, P. E.; Först, C. J.; Schimpl, J. Projector augmented wave method: ab initio molecular dynamics with full wave functions. *Bull. Mater. Sci.* **2003**, *26*, 33–41.

[202] Runge, E.; Gross, E. K. U. Density-Functional Theory for Time-Dependent Systems. *Phys. Rev. Lett.* **1984**, *52*, 997–1000.

[203] Mahan, G. D. *Many-Particle Physics*, 2nd ed.; Plenum Press: New York, 1990.

[204] Ren, X.; Rinke, P.; Joas, C.; Scheffler, M. Random-phase approximation and its applications in computational chemistry and materials science. *Journal of Materials Science* **2012**, *47*, 7447–7471.

[205] Hafner, J.; Heine, V. Theory of the atomic interactions in (s,p)-bonded metals. *J. Phys. F* **1986**, *16*, 1429.

[206] Starkloff, T.; Joannopoulos, J. D. Local pseudopotential theory for transition metals. *Phys. Rev. B* **1977**, *16*, 5212–5215.

[207] Onida, G.; Reining, L.; Rubio, A. Electronic Excitations: Density-Functional versus Many-Body Green's-Function Approaches. *Rev. Mod. Phys.* **2002**, *74*, 601–659.

[208] Imry, Y.; Landauer, R. *More Things in Heaven and Earth*; Springer, 1999; pp 515–525.

[209] Landauer, R. Spatial Variation of Currents and Fields Due to Localized Scatterers in Metallic Conduction. *IBM J. Res. Dev.* **1957**, *1*, 223–231.

[210] Landauer, R. Conductance determined by transmission: probes and quantised constriction resistance. *J. Phys.: Condens. Matter* **1989**, *1*, 8099.

[211] Büttiker, M.; Imry, Y.; Landauer, R.; Pinhas, S. Generalized many-channel conductance formula with application to small rings. *Phys. Rev. B* **1985**, *31*, 6207–6215.

[212] Weisstein, E. W. *Green's Function*; Wolfram Research, Inc., 2004.

[213] Arfken, G. B.; Weber, H. J.; Harris, F. E. *Mathematical Methods for Physicists: A Comprehensive Guide*; Academic Press, 2011.

[214] Martin, P. C.; Schwinger, J. Theory of Many-Particle Systems. I. *Phys. Rev.* **1959**, *115*, 1342–1373.

[215] Baym, G.; Kadanoff, L. P. Conservation Laws and Correlation Functions. *Phys. Rev.* **1961**, *124*, 287–299.

[216] Keldysh, L. V. Diagram technique for nonequilibrium processes. *Zh. Eksp. Teor. Fiz.* **1964**, *47*, 1515–1527.

[217] Ryndyk, D.; Gutiérrez, R.; Song, B.; Cuniberti, G. *Energy Transfer Dynamics in Biomaterial Systems*; Springer, 2009; pp 213–335.

[218] Ryndyk, D. A.; Gutiérrez, R.; Song, B.; Cuniberti, G. In *Energy Transfer Dynamics in Biomaterial Systems*; Burghardt, I., May, V., Micha, A. D., Bittner, R. E., Eds.; Springer Berlin Heidelberg: Berlin, Heidelberg, 2009; Chapter Green Function Techniques in the Treatment of Quantum Transport at the Molecular Scale, pp 213–335.

[219] Datta, S. Nanoscale device modeling: the Green's function method. *Superlattices Microstruct.* **2000**, *28*, 253–278.

[220] Bader, R. F. W. *Atoms in Molecules: A Quantum Theory*; Oxford University, 1990; Vol. 3; pp 1–120.

[221] Tang, W.; Sanville, E.; Henkelman, G. A grid-based Bader analysis algorithm without lattice bias. *J. Phys.: Condens. Matter* **2009**, *21*, 084204.

[222] Henkelman, G.; Arnaldsson, A.; Jónsson, H. A fast and robust algorithm for Bader decomposition of charge density. *Comp. Mater. Sci.* **2006**, *36*, 354–360.

[223] Saito, R.; Dresselhaus, G.; Dresselhaus, M. S. *Physical properties of carbon nanotubes*; World Scientific, 1998; Vol. 35.

[224] Dresselhaus, M. S., Dresselhaus, G., Avouris, P., Eds. *Carbon Nanotubes: Synthesis, Structure, Properties, and Applications*; Springer: Berlin, 2001.

[225] Schönenberger, C. Bandstructure of Graphene and Carbon Nanotubes: An Exercise in Condensed Matter Physics. **2000**, https://nanoelectronics.unibas.ch/education/Nanotubes/LCAO-NT.pdf (accessed Aug 20, 2016).

[226] Castro Neto, A. H.; Guinea, F.; Peres, N. M. R.; Novoselov, K. S.; Geim, A. K. The electronic properties of graphene. *Rev. Mod. Phys.* **2009**, *81*, 109–162.

[227] Mintmire, J.; White, C. Electronic and structural properties of carbon nanotubes. *Carbon* **1995**, *33*, 893 – 902.

[228] Hobson, J. P.; Nierenberg, W. A. The Statistics of a Two-Dimensional, Hexagonal Net. *Phys. Rev.* **1953**, *89*, 662–662.

[229] Olk, C. H.; Heremans, J. P. Scanning tunneling spectroscopy of carbon nanotubes. *J. Mater. Res.* **1994**, *9*, 259–262.

[230] Bahn, S. R.; Jacobsen, K. W. An Object-Oriented Scripting Interface to a Legacy Electronic Structure Code. *Comput. Sci. Eng.* **2002**, *4*, 56.

[231] Walter, M.; Häkkinen, H.; Lehtovaara, L.; Puska, M.; Enkovaara, J.; Rostgaard, C.; Mortensen, J. J. Time-dependent density-functional theory in the projector augmented-wave method. *J. Chem. Phys.* **2008**, *128*, 244101.

[232] Mowbray, D. J. Theoretical Electron Energy Loss Spectroscopy of Isolated Graphene. *Phys. Stat. Solidi B* **2014**, *251*, 2509–2514.

[233] Namal, I.; Ozelcaglayan, A. C.; Udum, Y. A.; Toppare, L. Synthesis and electrochemical characterization of fluorene and benzimidazole containing novel conjugated polymers: Effect of alkyl chain length on electrochemical properties. *Euro. Poly. J.* **2013**, *49*, 3181–3187.

[234] Späth, F. Präparation und Charakterisierung einwandiger Kohlenstoffnanorohr-Polyfluoren-Komplexe. Ph.D. thesis, Julius-Maximilians-Universität Würzburg, 2015.

[235] Cumings, J.; Zettl, A. In *Applied Physics of Carbon Nanotubes; Fundamentals of Theory, Optics, and Transport Devices*; Rotkin, S. V., Subramoney, S., Eds.; Springer-Verlag: Berlin, 2005; pp 273–306.

[236] Tao, S.; Miyata, Y.; Yanagi, K.; Kataura, H.; Okamoto, H. Subpicosecond coherent nonlinear optical response of isolated single-walled carbon nanotubes. *Phys. Rev. B* **2009**, *80*, 201405.

[237] Tu, X.; Manohar, S.; Jagota, A.; Zheng, M. DNA sequence motifs for structure-specific recognition and separation of carbon nanotubes. *Nature* **2009**, *460*, 250–253.

[238] Kramberger, C.; Roth, F.; Schuster, R.; Kraus, R.; Knupfer, M.; Einarsson, E.; Maruyama, S.; Mowbray, D. J.; Rubio, A.; Pichler, T. Channeling of charge carrier plasmons in carbon nanotubes. *Phys. Rev. B* **2012**, *85*, 085424.

[239] Lan, F.; Li, G. Direct Observation of Hole Transfer from Semiconducting Polymer to Carbon Nanotubes. *Nano Lett.* **2013**, *13*, 2086–2091.

[240] Goutam, P. J.; Singh, D. K.; Iyer, P. K. Photoluminescence Quenching of Poly(3-hexylthiophene) by Carbon Nanotubes. *J. Phys. Chem. C* **2012**, *116*, 8196–8201.

[241] Lanzi, M.; Paganin, L.; Caretti, D. New Photoactive Oligo- and Poly-Alkylthiophenes. *Polymer* **2008**, *49*, 4942–4948.

[242] Vardeny, Z.; Ehrenfreund, E.; Shinar, J.; Wudl, F. Photoexcitation Spectroscopy of Polythiophene. *Phys. Rev. B* **1987**, *35*, 2498–2500.

[243] Ren-Kuan, Y.; Zhen-Chun, H.; You-Dou, Z.; Wen-Guo, T.; Zi-Yuan, L.; Xue-Chu, S. Photoluminescence of Poly(3-methyl thiophene)–P3MT. *Acta Phys. Sin.* **1988**, *37*, 857.

[244] Bachilo, S. M.; Strano, M. S.; Kittrell, C.; Hauge, R. H.; Smalley, R. E.; Weisman, R. B. Structure-Assigned Optical Spectra of Single-Walled Carbon Nanotubes. *Science* **2002**, *298*, 2361.

[245] Galperin, M.; Nitzan, A. Raman Scattering and Electronic Heating in Molecular Conduction Junctions. *J. Phys. Chem. Lett.* **2011**, *2*, 2110–2113.

[246] Le Bahers, T.; Labat, F.; Pauporté, T.; Lainé, P. P.; Ciofini, I. Theoretical Procedure for Optimizing Dye-Sensitized Solar Cells: From Electronic Structure to Photovoltaic Efficiency. *J. Am. Chem. Soc.* **2011**, *133*, 8005–8013.

[247] Labat, F.; Le Bahers, T.; Ciofini, I.; Adamo, C. First-Principles Modeling of Dye-Sensitized Solar Cells: Challenges and Perspectives. *Acc. Chem. Res.* **2012**, *45*, 1268–1277.

[248] Le Bahers, T.; Pauporté, T.; Lainé, P.; Labat, F.; Adamo, C.; Ciofini, I. Modeling Dye-Sensitized Solar Cells: From Theory to Experiment. *J. Phys. Chem. Lett.* **2013**, *4*, 1044–1050.

[249] García-Lastra, J. M.; Thygesen, K. S.; Strange, M.; Ángel Rubio, Conductance of Sidewall-Functionalized Carbon Nanotubes: Universal Dependence on Adsorption Sites. *Phys. Rev. Lett.* **2008**, *101*, 236806.

[250] García-Lastra, J. M.; Mowbray, D. J.; Thygesen, K. S.; Rubio, Á.; Jacobsen, K. W. Modeling nanoscale gas sensors under realistic conditions: Computational screening of metal-doped carbon nanotubes. *Phys. Rev. B* **2010**, *81*, 245429.

[251] Strange, M.; Kristensen, I. S.; Thygesen, K. S.; Jacobsen, K. W. Benchmark Density Functional Theory Calculations for Nanoscale Conductance. *J. Chem. Phys.* **2008**, *128*, 114714.

[252] Glanzmann, L. N.; Mowbray, D. J.; Figueroa del Valle, D. G.; Scotognella, F.; Lanzani, G.; Rubio, A. Photoinduced Absorption within Single-Walled Carbon Nanotube Systems. *J. Phys. Chem. C* **2015**, *120*, 1926–1935.

[253] Kelly, M. K.; Etchegoin, P.; Fuchs, D.; Krätschmer, W.; Fostiropoulos, K. Optical Transitions of C_{60} Films in the Visible and Ultraviolet from Spectroscopic Ellipsometry. *Phys. Rev. B* **1992**, *46*, 4963–4968.

[254] Grüneis, A.; Attaccalite, C.; Wirtz, L.; Shiozawa, H.; Saito, R.; Pichler, T.; Rubio, A. Tight–Binding Description of the Quasiparticle Dispersion of Graphite and Few–Layer Graphene. *Phys. Rev. B* **2008**, *78*, 205425.

[255] Umari, P.; Petrenko, O.; Taioli, S.; De Souza, M. M. Communication: Electronic Band Gaps of Semiconducting Zig-Zag Carbon Nanotubes from Many-Body Perturbation Theory Calculations. *J. Chem. Phys.* **2012**, *136*, 181101.

[256] Despoja, V.; Mowbray, D. J. Using Surface Plasmonics to Turn on Fullerene's Dark Excitons. *Phys. Rev. B* **2014**, *89*, 195433.

[257] Mowbray, D. J.; Jones, G.; Thygesen, K. S. Influence of Functional Groups on Charge Transport in Molecular Junctions. *J. Chem. Phys.* **2008**, *128*, 111103.

[258] Späth, F.; Glanzmann, L. N.; Mowbray, D. J.; Rubio, A.; Hertel, T. (unpublished).

[259] Migani, A.; Mowbray, D. J.; Iacomino, A.; Zhao, J.; Petek, H.; Rubio, A. Level Alignment of a Prototypical Photocatalytic System: Methanol on $TiO_2(110)$. *J. Am. Chem. Soc.* **2013**, *135*, 11429–11432.

[260] Migani, A.; Mowbray, D. J.; Zhao, J.; Petek, H.; Rubio, A. Quasiparticle Level Alignment for Photocatalytic Interfaces. *J. Chem. Theory Comput.* **2014**, *10*, 2103–2114.

[261] Migani, A.; Mowbray, D. J.; Zhao, J.; Petek, H. Quasiparticle Interfacial Level Alignment of Highly Hybridized Frontier Levels: H_2O on $TiO_2(110)$. *J. Chem. Theory Comput.* **2015**, *11*, 239–251.

[262] Sun, H.; Mowbray, D. J.; Migani, A.; Zhao, J.; Petek, H.; Rubio, A. Comparing Quasiparticle H_2O Level Alignment on Anatase and Rutile TiO_2. *ACS Catal.* **2015**, *5*, 4242–4254.

[263] Mowbray, D. J.; Migani, A. Using G_0W_0 Level Alignment to Identify Catechol's Structure on $TiO_2(110)$. *J. Phys. Chem. C* **2015**, *119*, 19634–19641.

[264] Ltaief, A.; Bouazizi, A.; Davenas, J. Charge Transport in Carbon Nanotubes-Polymer Composite Photovoltaic Cells. *Materials* **2009**, *2*, 710–718.

[265] Ago, H.; Petritsch, K.; Shaffer, M. S.; Windle, A. H.; Friend, R. H. Composites of carbon nanotubes and conjugated polymers for photovoltaic devices. *Adv. Mater.* **1999**, *11*, 1281–1285.

[266] Plasticphotovoltaic.org - a hub for OPV research. (accessed Sep 19, 2016).

[267] U. S. Department of Energy. Photovoltaic Cell Conversion Efficiency Basics. http://energy.gov/eere/energybasics/articles/photovoltaic-cell-conversion-efficiency-basics (accessed Aug 20, 2013).

Abbreviations

Δ**SCF** delta self-consistent field 89

E_{11} first excited state in SWNTs 6–8, 59, 65, 67–73, 75, 79, 80, 87, 88, 94

E_{22} second excited state in SWNTs 59, 87

AE all-electron 9, 22, 25–27

AFM atomic force microscopy 6

ALDA adiabatic local density approximation 30

ASE atomic simulation environment 51, 59, 64, 76

BBO β-barium borate 62, 63

BHJ bulk heterojunction 2, 4

BOA Born-Oppenheimer approximation 14

CB conduction band 1, 70, 72, 84

CBM conduction band minimum 68, 70, 77, 79, 82–84

CIS single excitation configuration interaction 89

CoMoCAT® cobalt-molybdenum catalyst 5, 62

CT charge transfer 2, 7, 81

CVD chemical vapor deposition 5, 62

DFT density functional theory i, 8, 9, 20, 22, 51, 59, 63, 64, 70, 72, 76–78, 80, 84, 86

DOS density of states 35, 46, 49

DZP double-zeta polarized 26, 59, 64, 76

ECL electron collecting layer 3, 4

EOM-CC equation-of-motion coupled cluster 89

eV electronvolt 1–3, 8, 51–54, 56, 57, 59, 64, 69–71, 73–76, 79, 80, 83, 84, 86, 93

FBZ first Brillouin zone 46

FF fill factor 91, 92

FFT fast Fourier transform 24

gcd greatest common divisor 44

GGA generalized gradient approximation 13, 20, 30, 76

HCL hole collecting layer 3
HF Hartree-Fock 16
HiPco high-pressure carbon monoxide disproportionation 5
HOMO highest occupied molecular orbital 2, 54, 81–84, 86, 89

IQE internal quantum efficiency i, 8, 10, 32, 76, 92
IR infrared spectral region 62–65
ITO indium tin oxide 2–4

KS Kohn-Sham 6, 9, 13, 18, 22–25, 28–30, 36, 41, 52, 70, 78–80, 83, 89

LCAO locally centered atomic orbital 7, 9, 22, 25, 26, 59, 64, 76, 78, 93, 94
LDA local density approximation 13, 19, 20, 30, 59
LDR linear dielectric response i, 6, 9, 10, 30, 52, 54, 62–64, 70–75, 85, 88
LED light emmiting diode 90
LFE local field effects 31, 52, 62, 64, 70, 93, 94
LR linear response i, 6, 9, 10, 54, 58–62, 85, 87, 88, 93
LUMO lowest unoccupied molecular orbital 2, 54, 82–84, 86, 89

MEH-PPV poly[2-methoxy-5-(2-ethylhexyloxy)-1,4-phenylenevinylene] 90
MWNT multi-walled carbon nanotube 64, 77

NEGF non-equilibrium Green's function i, vi, 8, 9, 32, 35, 36, 38–40, 76, 78, 81, 85, 86, 90
NIR near infrared spectral region 1, 6, 58, 62, 65

ODCB ortho-dichlorobenzene 62
OMA optical multichannel analyzer 63
OPV organic photovoltaic i, 1–5, 8–11, 32, 36, 41, 51, 74, 82, 85, 86, 89–91

P3HT poly(3-hexylthiophene-2,5-diyl) 1–4, 7, 62, 64–68, 72–74, 76, 79, 82, 89
P3MT poly(3-methylthiophene-2,5-diyl) 76–84, 89
PA photoinduced absorption i, 7, 8, 10, 11, 62, 65, 66, 68, 69, 71, 73, 74, 85, 88, 89
PAW projector augmented wave 9, 22, 25–27, 51, 59, 64, 76
PB photobleach 62, 65, 66, 68–70, 72, 73, 88
PBE Perdew-Burke-Ernzerhof xc functional 13, 20, 30, 51, 59, 64, 76
PCBM phenyl-C_{61}-butyric acid methyl ester 2, 4, 62, 64–68, 70–74, 82, 89
PCE power conversion efficiency 1, 3, 4, 74, 92
PEDOT:PSS poly(3,4-ethylenedioxythiophene)poly(styrenesulfonate) 3
PFO 9,9-dioctylfluorenyl-2,7-diyl 5, 6, 10, 55, 57, 86
PFO-BPy copolymer of 9,9-dioctylfluorenyl-2,7-diyl and bipyridine i, 5, 6, 10, 11, 51–60, 85–87
PL photoluminescence 79
PLQY photoluminescence quantum yields 5
PPV poly(p-phenylene vinylene) 90
PS pseudo 9, 22, 26, 27

PT polythiophene 62, 64, 65, 70–72, 74, 76–84, 89

Py pyridine 6, 10, 56, 86

Py-PFO-Py copolymer of pyridine, 9,9-dioctylfluorenyl-2,7-diyl and pyridine 6, 10, 11, 51–57, 60, 61, 85–87

QED quantum electrodynamical 7

RPA random phase approximation i, 6, 9, 10, 28, 30, 52, 54, 62–64, 70–76, 85, 86, 88, 93

s-SWNT semiconducting single-walled carbon nanotube i, 3, 4

SDS sodium dodecyl sulphate 5

SEM scanning electron microscopy 6

SHG second harmonic generation 63

SOMO singly occupied molecular orbital 82, 84

ssDNA single-stranded deoxyribonucleic acid 5

SUMO singly unoccupied molecular orbital 82, 84

SWNT single-walled carbon nanotube x, 3–11, 43–45, 47–49, 51, 52, 58–60, 62–90, 93, 94

SZ single-zeta 26

TDDFT time-dependent density functional theory i, 6, 7, 9, 10, 28, 30, 51–54, 58–64, 70–75, 85–89, 93

TDM transition dipole moment 6, 11, 58–60, 85

UV ultraviolet spectral region 1, 6, 58, 65

VB valence band 1, 70, 72, 84

VBM valence band maximum 70, 72, 77, 79, 82, 84

vdW-DF van der Waals xc functional 13, 20, 21, 86

VIS visible spectral region 2, 6, 7, 58, 65

xc exchange and correlation 9, 13, 19, 20, 24, 27, 30, 51, 59, 64, 76, 80